SUBSURFACE CHARACTERIZATION USING HEAD-WAVE ARTIFACTS IN SEISMIC INTERFEROMETRY

by

Thomas Dylan Mikesell

A dissertation
submitted in partial fulfillment
of the requirements for the degree of
Doctor of Philosophy in Geophysics
Boise State University

May 2012

BOISE STATE UNIVERSITY GRADUATE COLLEGE

DEFENSE COMMITTEE AND FINAL READING APPROVALS

of the dissertation submitted by

Thomas Dylan Mikesell

Dissertation Title: Subsurface Characterization Using Head-Wave Artifacts in Seismic Interferometry

Date of Final Oral Examination: 2 December 2011

The following individuals read and discussed the dissertation submitted by student Thomas Dylan Mikesell, and they evaluated his presentation and response to questions during the final oral examination. They found that the student passed the final oral examination.

Kasper van Wijk, Ph.D.	Chair, Supervisory Committee
John H. Bradford, Ph.D.	Member, Supervisory Committee
Hans-Peter Marshall, Ph.D.	Member, Supervisory Committee
Jodi L. Mead, Ph.D.	Member, Supervisory Committee
Andrew Curtis, Ph.D.	External Examiner

The final reading approval of the dissertation was granted by Kasper van Wijk, Ph.D., Chair of the Supervisory Committee. The dissertation was approved for the Graduate College by John R. Pelton, Ph.D., Dean of the Graduate College.

ACKNOWLEDGMENTS

I have to express my gratitude to Dr. Kasper van Wijk for making my experience at Boise State University, and throughout our professional relationship, absolutely wonderful. I cannot describe how much I have enjoyed myself over the past four and half years. I attribute a lot of that enjoyment to Dr. van Wijk's enthusiasm for research, and life in general. I would not trade this experience for the world. I would like to thank the members of the Physical Acoustics Lab, particularly Andy Lamb, Thomas Blum and Dr. Mila Adam for always giving input, reading abstracts and papers, and taking time from their busy schedules to make sure I had plenty of good meals, a fishing buddy, and other distractions.

Support for the work in this dissertation comes from multiple sources, but largely a Department of Defense National Defense Science and Engineering Graduate Fellowship and a National Science Foundation GK12 Fellowship. I especially want to thank Dr. Karen Viskupic, Dr. David Wilkins, and Dr. Jim Belthoff for the GK12 opportunity. I learned a great deal about the importance of community outreach, and I am forever grateful for the knowledge I gained about myself and my role as an educator during my year as a GK12 fellow.

I thank my committee members, Dr. John Bradford, Dr. Hans-Peter Marshall, and Dr. Jodi Mead, for their interest in this dissertation as well as their time and

suggestions. I especially thank Dr. Matt Haney for many valuable tips, jokes, and help with computer coding. I thank Dr. Alex Calvert for very stimulating talks about the virtual refraction theory during the beginning of this dissertation.

Developing a complete understanding of seismic interferometry was aided by a three month visit to Delft University of Technology, The Netherlands. I would particularly like to thank Dr. Kees Wapenaar, Dr. Deyan Draganov, and Elmer Ruigrok, who put a lot of time and effort into making that trip possible, as well as helping bring me up to speed on all aspects of seismic interferometry.

Last but not least, I would like to thank friends and family, especially my parents Tom and Dana, my brother Jack, my sister Hannah, and her family–Stephen, Henry, and Wyatt. I feel extremely fortunate to have had the opportunity to return to Idaho for graduate school. Without their support, this experience would not have been so fun and enjoyable.

ABSTRACT

Seismologists continually work to improve images of the Earth's interior. One new approach is seismic interferometry, which involves cross-correlating the seismic wavefield recorded at two receivers to generate data as if one of the receivers was a source. Over the past decade, seismic interferometry has become an established technique to estimate the surface-wave part of the impulse response between two receivers; however, practical limitations in the source-energy distribution have made body-wave recovery difficult and causes spurious energy in the estimated impulse response. Rather than suppress such spurious energy, it can be useful to analyze coherent spurious events to help constrain subsurface parameters.

With this in mind, we examine a particular spurious event we call the virtual refraction. This event comes from cross-correlating head-wave (or critically refracted) energy at one receiver with reflection and refraction energy at the other receiver. For this particular spurious event, we find that, similar to surface waves, the important part of the source-energy distribution is readily available. The sources need to be at or past the critical offset from both receivers. In a horizontal, two-layer subsurface model, the slope of the virtual refraction defines the velocity of the fast layer (V_2). Furthermore, the stationary-phase point in the correlation gather defines the critical offset, a property that depends on the thickness (H) and velocity (V_1) of the slow layer.

A two-layer numerical example is presented to illustrate the origin of the virtual refraction. After estimating the refractor velocity, a semblance analysis can be used to estimate H and V_1. In field data from the Boise Hydrogeophysical Research Site, the virtual refraction alone is used to the estimate H, V_1, and V_2. This is an improvement over methods that rely on several wave types to fully characterize seismic properties above and below an interface. An exploration-scale active source seismic data set illustrates how we can use the method to build near-surface seismic models that can then be used for statics estimation in standard reflection processing. Finally, we investigate multi-component seismic interferometry for the virtual refraction, a technique that has recently been developed to more accurately estimate the surface-wave impulse response with higher signal-to-noise than traditional single component estimates. We find that using multi-component correlations to estimate shear wave virtual refractions also improves signal-to-noise, but with a dependence on the incidence angle of the incoming wavefield.

TABLE OF CONTENTS

LIST OF FIGURES

LIST OF TABLES

CHAPTER 1:

INTRODUCTION

The field of seismology has changed tremendously over the past 50 years. Computational power has expanded, as well as our ability to store large amounts of data. We have improved processing techniques and developed more accurate mathematical representations of the seismic wavefield. There have also been a number of advancements in hardware, such that we are able to record more broadband signals at a lower cost. In the end though, these improvements have all been made with one goal to improve the resolution and accuracy of seismic images.

In all seismic studies, the spatial sampling of sources and receivers is a limitation that has major consequences on the quality of the seismic image. In the Earth, which is infinitely dimensional in space and therefore impossible to completely sample seismically, we use strategically placed sources and receivers to illuminate, as best we can, the subsurface parts that are of interest. With receivers being inexpensive compared to active sources, it has been the focus of one branch of seismology over the last decade to develop methods based on extracting the impulse response between a receiver and a so-called virtual source (Bakulin and Calvert, 2006). This technique has been formalized and termed seismic interferometry in active-source seismology (Wapenaar and Fokkema, 2006; Curtis *et al.*, 2006). Seismic interferometry is a method to estimate the impulse response between any two receivers, as if one were a source. Two examples related to downhole receivers, where sources are extremely difficult to place, are given by Bakulin and Calvert (2006) and Mehta *et al.* (2007). Countless other studies have demonstrated that seismic interferometry is a technique that can improve the spatial sampling of seismic surveys for many geometries. In principle, at the exploration scale, this allows one to increase stacking fold cheaply while avoiding sources in sensitive areas where dynamite and vibroseis are not appropriate. It also allows us to redatum the wavefield, eliminating difficult statics problems caused by the complex near-surface.

The major requirement of seismic interferometry is that the wavefield be recorded simultaneously at both receivers. If this is the case, the method can even be applied to passive-source seismic data. Previously, passive seismologists were limited to using the impulse response between a receiver and an earthquake. Unfortunately, earthquakes occur mostly near plate boundaries, limiting subsurface illumination in some parts of the Earth. Ambient noise tomography, which has added a new dimension to surface-wave inversion for the Earth's lithosphere, is closely related to seismic interferometry. Using Earth's natural seismic noise (e.g., ocean microseism), we can now estimate phase- and group-velocity dispersion curves between distributed station pairs and invert for 3D velocity structure (e.g., Sabra *et al.*, 2005; Shapiro *et al.*, 2005; Lin *et al.*, 2008; Ekstrom *et al.*, 2009). This approach greatly improves our ability to illuminate the subsurface, as well as allows us to turn earthquakes into receivers buried deep within the Earth (Curtis *et al.*, 2009).

Accurately estimating the impulse response relies on the notion that seismic energy comes from all directions. In passive-source seismology, this is called the equipartition of waves and often comes from multiple scattering. Equipartition means that all directions of propagation are equally likely (i.e., the wavefield has no preferred wave number). In active-source seismology, we need to place sources everywhere, or at least everywhere in the subsurface surrounding the two receivers (Wapenaar and Fokkema, 2006). In either case, it has been known for many years that the *sources everywhere* requirement can be relaxed as long as the stationary-phase points in the seismic interferometry integral are sampled.

In typical land seismic acquisition, sampling the stationary-phase points for body waves is difficult and artifacts in the estimated impulse response arise. Exploring the cause of one such artifact, a virtual refraction, we determined that this artifact contains useful information about the subsurface. The reasons for studying such artifacts are many. Generating the impulse response between two receivers can be very useful, but artifacts due to the source-energy distribution can be misinterpreted and lead to inaccurate subsurface models. Characterizing and understanding the origin of artifacts makes it possible to suppress them during the seismic imaging process. Furthermore, it is beneficial to use these artifacts to constrain seismic properties in the subsurface. This dissertation is devoted to understanding one artifact in the interferometric wavefield; however, our analysis can be applied to different wave modes to gain similar understanding of other artifacts. The chapters are divided in the following way to provide a step-by-step understanding of the virtual refraction artifact.

1.1 Investigating Head Waves in Seismic Interferometry

This chapter covers the application of seismic interferometry to a two-layer acoustic model. The majority of this chapter was published as Mikesell *et al.* (2009). It begins with a short introduction to seismic interferometry and critically refracted (i.e., head wave) energy. Using an active-source numerical example, we illustrate how head waves behave during the application of seismic interferometry. Specifically, we highlight an artifact in the interferometric wavefield due to violating the theoretical restrictions placed on seismic interferometry. This artifact is the virtual refraction.

1.2 Characterizing an Aquifer with the Virtual Refraction

The field data example in this chapter comes from Nichols *et al.* (2010) and illustrates the virtual refraction using a 2D hammer seismic data set from the Boise Hydrogeophysical Research Site. At this location, the water table is so shallow that surface waves mask the reflection and make standard reflection imaging difficult. There is a strong head wave generated by the sharp contrast between unsaturated and saturated sediments that generates a virtual refraction in the seismic interferometry result. By creating a virtual shot record, we suppress uncorrelated noise and produce a virtual refraction that intercepts zero offset at zero time. These two features make the virtual refraction easy to pick, providing an estimate of refractor (saturated sediment) velocity. To obtain the physical parameters of the layer above the refractor, we analyze the cross-correlation of wavefields recorded at two receivers for all sources. A stationary-phase point associated with the correlation between the reflected wave and refracted wave from the interface identifies the critical offset. By combining information from the virtual shot record, the correlation gather, and the real shot record, we determine the seismic velocities of the unsaturated sand, as well as the relative depth to the water table. This work demonstrates the requirements placed on spatial sampling in order to recover information about the subsurface using the virtual refraction.

1.3 Semblance Analysis on the Correlation Gather

This chapter comes from Mikesell and van Wijk (2011), whereby we use the correlation between reflected and refracted energy to estimate the seismic properties of the slow layer. We present a semblance analysis on the correlation gather of a numerical data set to estimate the slow layer thickness and velocity. The semblance method is further illustrated using the Boise Hydrogeophysical Research Site data. We find good agreement with previously published results for estimates of depth and velocity. Using the semblance approach, we find that we no longer need the variable source and receiver spacing required by Nichols *et al.* (2010).

1.4 Statics Estimation with the Virtual Refraction

In this chapter, we apply the virtual refraction analysis to 2D synthetic land seismic exploration data with statics caused by near-surface weathering layer thickness variations. Using the *delay-time method*, we estimate source and receiver statics using first-break arrival times. We go on to develop a *modified delay-time method*, wherein we use the first-break arrival times of the virtual refraction to isolate and estimate receiver statics. We show that this approach simplifies the inverse problem by removing the source static term from the delay-time equation. Finally, we show that using the virtual refraction extends lateral resolution and is better suited for estimating statics when the data are noisy.

1.5 Using the Green Tensor to Isolate Wave Modes

This chapter demonstrates the use of multi-component cross-correlations. We show that the cross terms of the Green tensor can be used to estimate the impulse response. A 1D laboratory example illustrates this idea on surface waves. The Batholiths temporary seismic deployment example from van Wijk *et al.* (2011) is then shown in Section 6.3 to demonstrate the cross terms in 2D. With this data, we provide estimates of the Rayleigh wave with a higher signal-to-noise ratio and a consequently better phase-velocity dispersion curve. We then investigate if a similar improvement in signal-to-noise exists for body waves. We use the Green tensor cross terms to estimate the wavefield using numerical elastic wave data. In particular, we highlight what happens to the virtual S-wave refraction with regard to phase and amplitude. We find the signal-to-noise improves in the cross-term estimate, but the phase relationship is not the same as the case for Rayleigh waves.

CHAPTER 2:

INVESTIGATING HEAD WAVES IN SEISMIC INTERFEROMETRY

Summary

We investigate Green's function recovery in a two-layer model in which we violate assumptions in the seismic interferometry theory. We show that violating these assumptions leads to an artifact we call the virtual refraction. We investigate the origins of this artifact and show how the artifact can be used to estimate the P-wave velocity in the fast layer and aid estimates of the slow layer thickness and velocity. Finally, we show results from a numerical experiment with a source/receiver geometry that resembles a 2D-land seismic experiment and determine that all sources past the critical offset from any two receivers contribute energy to the virtual refraction.

2.1 A Two-Layer Model and the Interferometric Result

Consider the two-layer acoustic model shown in Figure 2.1. The top layer has velocity $V_1 = 1250$ m/s, the bottom layer has velocity $V_2 = 1750$ m/s, and the density is 1000 g/cm^3 in both layers. We place an explosive seismic source (with a dominant wavelength of ~ 30 m) at the first receiver location ($r1$) and model the wavefield for 0.8 s after the explosion on 101 receivers evenly spaced on a 400 m line, 52 m above the interface. We use the spectral element modeling method, widely used in global seismology (Komatitsch and Vilotte, 1998; Komatitsch and Tromp, 2002). The left panel of Figure 2.2 shows three coherent events in the modeled wave field: 1) the direct wave, 2) the reflected wave from the interface, and 3) the refracted wave at offsets greater than 300 m. Now, using seismic interferometry, we attempt to recover the wavefield between two receiver positions based on Equation 19 from Wapenaar and Fokkema (2006), which represents the exact acoustic Green's function:

$$\begin{aligned}\hat{G}(\mathbf{x}_A, \mathbf{x}_B) + \hat{G}^*(\mathbf{x}_A, \mathbf{x}_B) &= \oint_S \frac{-1}{j\omega\rho(\mathbf{x})}(\hat{G}^*(\mathbf{x}_A, \mathbf{x})\partial_i(\hat{G}(\mathbf{x}_B, \mathbf{x})) \\ &- \partial_i(\hat{G}^*(\mathbf{x}_A, \mathbf{x}))\hat{G}(\mathbf{x}_B, \mathbf{x}))n_i dS, \qquad (2.1)\end{aligned}$$

where $\hat{G}(\mathbf{x}_A, \mathbf{x}_B)$ denotes the causal frequency domain Green's function at $\mathbf{x}_A$ from a source at $\mathbf{x}_B$ and $\hat{G}^*(\mathbf{x}_A, \mathbf{x}_B)$ denotes the complex conjugate Green's function, which corresponds to the anticausal time-domain Green's function. Angular frequency is ω, ρ is density and j is $\sqrt{-1}$. $\hat{G}^*(\mathbf{x}_A, \mathbf{x})$ and $\hat{G}(\mathbf{x}_B, \mathbf{x})$ represent the Green's functions at locations $\mathbf{x}_A$ and $\mathbf{x}_B$ due to a monopole source at $\mathbf{x}$, and $\partial_i\hat{G}^*(\mathbf{x}_A, \mathbf{x})$ and $\partial_i\hat{G}(\mathbf{x}_B, \mathbf{x})$ represent the Green's functions at locations $\mathbf{x}_A$ and $\mathbf{x}_B$ due to a dipole source at

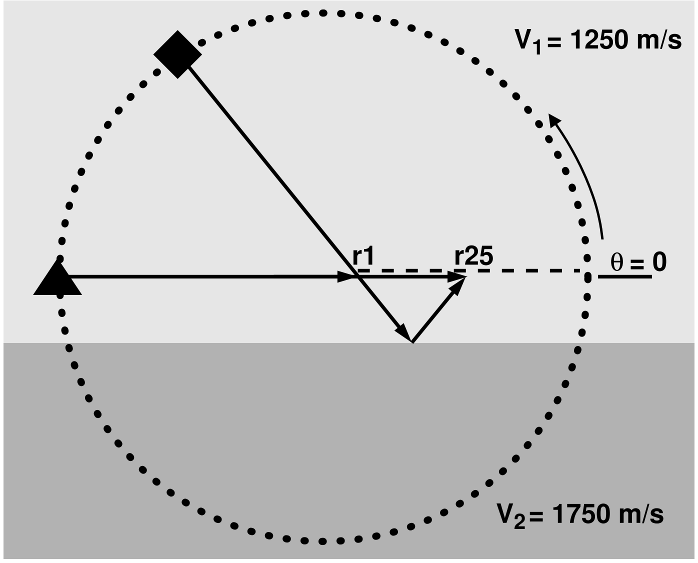

Figure 2.1: Layout of the acoustic numerical model with 2880 sources on a circle with radius 475 m and 101 receivers every 4 m on the dashed line, 52 m above the interface. Receiver $r1$ is located 75 m to the right of the circle center. The diamond and square infer stationary phase points, described in the section - The stationary phase in the far-field.

$\mathbf{x}$. S is the closed integration surface around the receivers $\mathbf{x}_{A,B}$. To approximate this analytic result, we use a finite number of sources on a surface surrounding our receivers (Figure 2.1). We choose the integration surface S to be a circle with radius 475 m. We place the receiver array 75 m to the right of the circle center. We distribute 2880 dipole and monopole seismic sources evenly over the circle, approximately one dipole and monopole source every meter along the circle. We simulate a monopole source using an explosive source. A dipole source consists of the addition of an explosion (located 2.5 m outside the circle) and an implosion (located 2.5 m inside the circle), divided over the distance (5 m) between them. We center the dipole at the monopole source location and orient it normal to the circle.

We cross-correlate the wavefields according to Equation 2.1 for each source po-

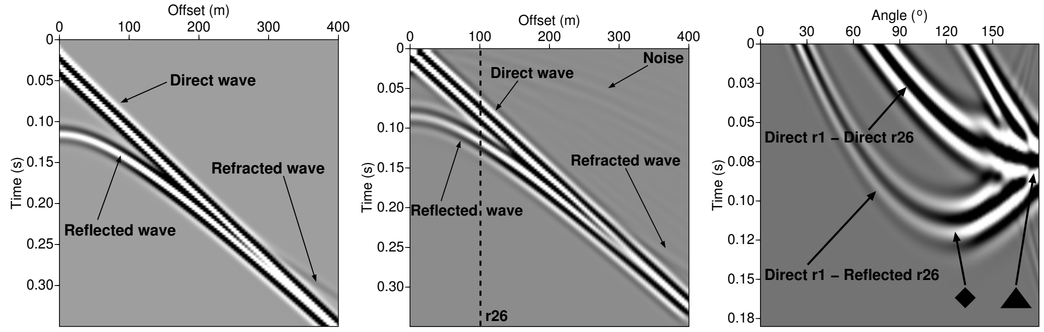

Figure 2.2: Left: shot record from an explosive source placed at receiver $r1$ (i.e., zero-offset) showing the direct, reflected, and refracted waves. Middle: virtual shot record based on a discretized Equation 2.1. The wavelet in the seismic interferometry result is the auto-correlation of the real shot wavelet. Right: correlation gather between $r1$ and $r26$ (dash line-middle plot) for all monopole sources on the top half of the circle. The stationary-phase regions are indicated with arrows and symbols correspond to those in Figure 2.1: the triangle is related to the direct wave, the diamond is related to the reflected wave.

sition. We set $\mathbf{x}_B = r1$ so that it is always this receiver cross-correlated with the 101 receivers; $r1$ is commonly called the virtual source (Bakulin and Calvert, 2004). After summing the cross-correlations for all sources, we obtain the virtual shot record shown in the middle panel of Figure 2.2. Because we are limited to a finite number of sources on S, we observe some noise before the first breaks. There is a phase difference in the source wavelet between the real and the virtual shot records because the source wavelet is squared in the cross-correlation procedure of seismic interferometry (Snieder, 2004; Wapenaar and Fokkema, 2006).

2.2 Stationary Phase Analysis in the Far-Field

Wapenaar and Fokkema (2006) simplify Equation 2.1 by making the following assumptions:

- All sources lie in the far-field (i.e., the distance from the source to the receivers and scatterers is large compared to the wavelength).
- Rays take off approximately normal from the integration surface S.
- The medium outside the integration surface S is homogeneous, such that no energy going outward from the surface is scattered back into the system.
- The medium around the source is locally smooth (the high-frequency approximation).

Following these assumptions, the spatial derivative can be approximated by a time derivative:

$$\partial_i \hat{G}(\mathbf{x}_A, \mathbf{x}) n_i \approx -j \frac{\omega}{c(\mathbf{x})} \hat{G}(\mathbf{x}_A, \mathbf{x}). \tag{2.2}$$

With this approximation, Equation 2.1 simplifies to Equation 31 in Wapenaar and Fokkema (2006):

$$\hat{G}(\mathbf{x}_A, \mathbf{x}_B) + \hat{G}^*(\mathbf{x}_A, \mathbf{x}_B) \approx \oint_S \frac{2\hat{G}^*(\mathbf{x}_A, \mathbf{x}) \hat{G}(\mathbf{x}_B, \mathbf{x})}{\rho(\mathbf{x}) c(\mathbf{x})} dS, \tag{2.3}$$

where c is the acoustic velocity. From this expression, we use the stationary phase argument (e.g., Snieder, 2004) to investigate the origin of events in the virtual shot record. In the right panel of Figure 2.2, we present the causal part of the correlations between $r1$ and $r25$ (i.e., offset $|\mathbf{x}_A - \mathbf{x}_B| = 100$ m) for all monopole sources in the upper hemisphere of integration surface S to illustrate the validity of the far-field approximation for the direct and reflected waves. We ignore correlations from sources in the lower half because no stationary points exist. We observe several coherent events in this so-called correlation gather that give rise to the events in the virtual shot record (Mehta *et al.*, 2008). The correlation of the direct wave at $r1$ with the direct wave at $r25$ has a stationary phase point at 180° and is associated with the direct wave traveling from $r1$ to $r25$ in ~ 0.08 s. The arrows marked with a black triangle in Figure 2.1 and in the right panel of Figure 2.2 indicate that this is the source location where source and receiver are in-line. Another coherent event in the virtual shot record stems from the correlation between the direct wave at receiver $r1$ and the reflected wave at $r25$. This event has a stationary phase point at $\sim 120°$ associated with the reflected wave traveling from $r1$ to $r25$ in ~ 0.12 s. The arrows marked with a black diamond in Figure 2.1 and in the right panel of Figure 2.2 indicate that this is the source location where the wave reflects to $r25$ after passing through $r1$. These stationary phase points result in the two arrivals in the middle panel of Figure 2.2 at 100 m offset. The weaker correlations seen at sources past 150° are associated with refractions and are discussed next.

2.3 Violation of the Far-Field Approximation

The top panel of Figure 2.3 is a magnification of the previously mentioned weaker correlations, except now we show the correlations between receivers $r1$ and $r101$ to emphasize the longer offsets. We identify correlations between the refracted wave at $r101$ and either the direct, reflected, or refracted wave at $r1$. For this particular model, sources between $\sim 170°$ and the layer interface provide the visible stationary correlation at ~ 0.23 s. This correlation is between the refracted wave at $r1$ and the refracted wave at $r101$ (see the bottom panel of Figure 2.3). These refractions have travel times in common down to and up from the refractor. Hence, the time of the correlation is only a function of the difference in travel paths along the refractor, denoted by dr in the bottom panel of Figure 2.3. As we show next, this correlation does not cancel when using only explosive (i.e., monopole) sources required by the approximate interferometric integral.

The virtual shot record using the approximate far-field integral (i.e., using only monopole sources on the circle) is shown in the left panel of Figure 2.4. Again we recover the correct direct, reflected, and refracted waves. However, we also observe a spurious linear event traveling at $V_2 = 1750$ m/s going through the origin. We call this spurious arrival the virtual refraction. This event is a direct result of violating the far-field approximation represented by Equation 2.2, as it is the only approximation we made to the exact interferometric integral. The assumptions in Equation 2.2 are violated for those sources where the interface between V_1 and V_2 is located in the near-field.

2.4 A Line of Sources

Since sources located at post-critical locations on the circle are responsible for the virtual refraction, we can instead place explosive sources on a line at post-critical offsets to generate this event. The bottom panel of Figure 2.3 illustrates how post-critical sources on the circle can be transposed onto such a line. We place a line of 110 explosive sources 52 m above the interface, to the left of the receiver line. This model more closely resembles a common 2D data acquisition geometry in seismic surveys, except that one more commonly performs this experiment at the surface. Here we bury sources and receivers to eliminate correlations associated with surface-related multiples. The middle panel of Figure 2.4 shows the virtual shot record

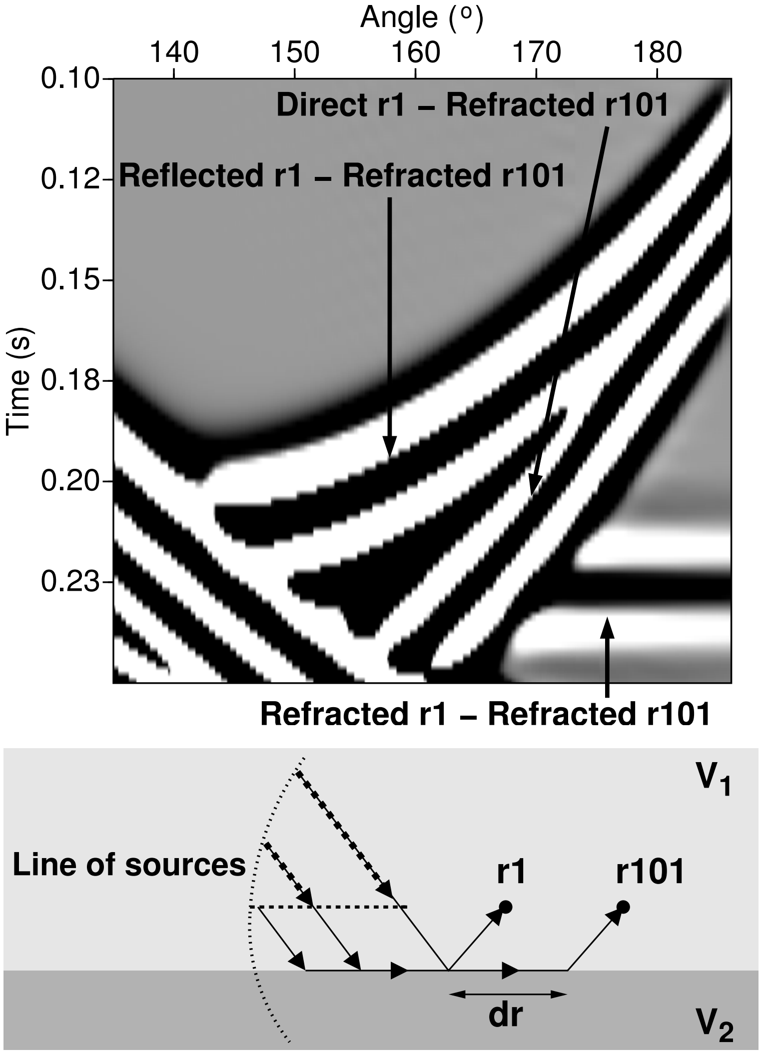

Figure 2.3: Top: correlation gather between $r1$ and $r101$. Bottom: paths for refracted waves traveling from source to $r1$ and $r101$. Note that these post-critical sources on the circle can be transposed to a line of sources.

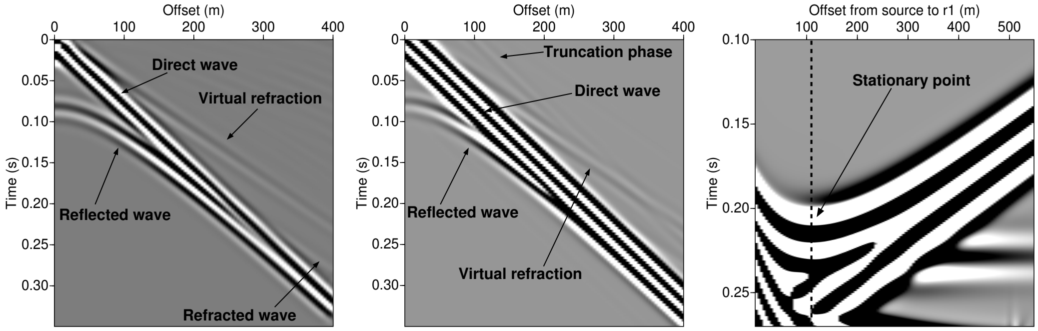

Figure 2.4: Left: virtual shot record using only explosive sources on the circle. In addition to the direct, reflected, and refracted waves, we observe a linear spurious event: the virtual refraction. Middle: virtual shot record for a line of explosive sources, showing direct and reflected waves, along with the virtual refraction. Right: correlation gather for $r1$ and $r101$ with a constant phase for the correlation between refracted waves at the larger offsets. Note also the stationary-phase point at the critical offset (dashed line) when the source is 106 m from $r1$.

obtained following Equation 2.3 using the line of explosive sources. We identify the direct, reflected, and refracted waves, as well as the virtual refraction. Other linear events not crossing the origin are truncation phases, as our source coverage is abruptly ended on each side of the source line (Snieder *et al.*, 2008). The small amplitude variations in the virtual refraction at ~ 0.15 s and ~ 0.25 s arise from wave interference with these truncation phases. It is worth noting that because all contributions from post-critical sources sum constructively, the virtual refraction is robust in the presence of uncorrelated noise.

2.4.1 The Critical Offset

While the virtual refraction is not part of the true Green function, its move-out defines the wave speed V_2 in the bottom layer, and because dr goes to zero as we approach the virtual shot location, the intercept time of the virtual refraction is by definition $t = 0$ s. Therefore, unlike in conventional refraction analysis (Palmer, 1986; Lowrie, 2007), important subsurface information about the top-layer velocity V_1 and interface depth H cannot be determined from the virtual refraction alone. Despite this, Tatanova *et al.* (2009, 2011) have shown that time-lapse measurements of the virtual refraction are useful for reservoir monitoring.

We overcome the lack of a refraction intercept time by investigating events in the correlation gather between $r1$ and $r101$ for the line of explosive sources (right panel of Figure 2.4). For long offset sources, we see the constant feature at $t \approx 0.23$ s. The correlation between the direct and the refracted wave is represented by a straight line while the curving feature represents the correlation between the reflected and refracted waves, having an extremum at $x \approx 106$ m (dashed line). This stationary-phase point, associated with the correlation between reflected and refracted waves, occurs at the critical offset.

Using the sine of the critical angle $\sin(\theta_c) \equiv V_1/V_2$, Pythagorean theorem, and the parameters in Figure 2.5, we write

$$\sin(\theta_c) \equiv \frac{V_1}{V_2} = \frac{X_c/2}{\sqrt{(X_c/2)^2 + H^2}} \Leftrightarrow X_c = \frac{2V_1 H}{\sqrt{V_2^2 - V_1^2}}. \tag{2.4}$$

To show that this is the same offset between the source and $r1$ where the maximum delay between refracted and reflected waves occurs, we set the spatial derivative of the difference in arrival times to zero and solve for offset x:

$$\begin{aligned}
&\frac{d}{dx}\left(t_{refr}-t_{refl}\right)=0 \quad \Leftrightarrow \\
&\frac{d}{dx}\left(\left(\frac{2H\cos\theta_c}{V_1}+\frac{x}{V_2}\right)-\sqrt{\left(\frac{x}{V_1}\right)^2+\left(\frac{2H}{V_1}\right)^2}\right)=0 \quad \Leftrightarrow \\
&\frac{1}{V_2}-\frac{x}{V_1\sqrt{x^2+(2H)^2}}=0 \quad \Leftrightarrow \quad x=\frac{2V_1H}{\sqrt{V_2^2-V_1^2}},
\end{aligned} \tag{2.5}$$

which equals the definition of the critical offset in Equation 2.4. The critical time t_c can be picked on real data as the arrival time of the reflected event on $r1$ for the source at $X_c \approx 106$ m. Then, with observables x_c, t_c, and V_2, we can uniquely solve for H by rearranging Equation 2.4:

$$H = X_c\sqrt{V_2^2-V_1^2}/(2V_1). \tag{2.6}$$

Using $t_c = 2\sqrt{H^2+(X_c/2)^2}/V_1$ and Equation 2.6, we can also solve for the top-layer wave speed V_1:

$$V_1 = \sqrt{(V_2X_c)/t_c}. \tag{2.7}$$

In the presence of a dipping refractor, one would perform seismic interferometry with source lines on both sides of the receiver line. The average of the two speeds observed in the virtual refractions determines V_2, similarly to conventional refraction techniques (Palmer, 1986).

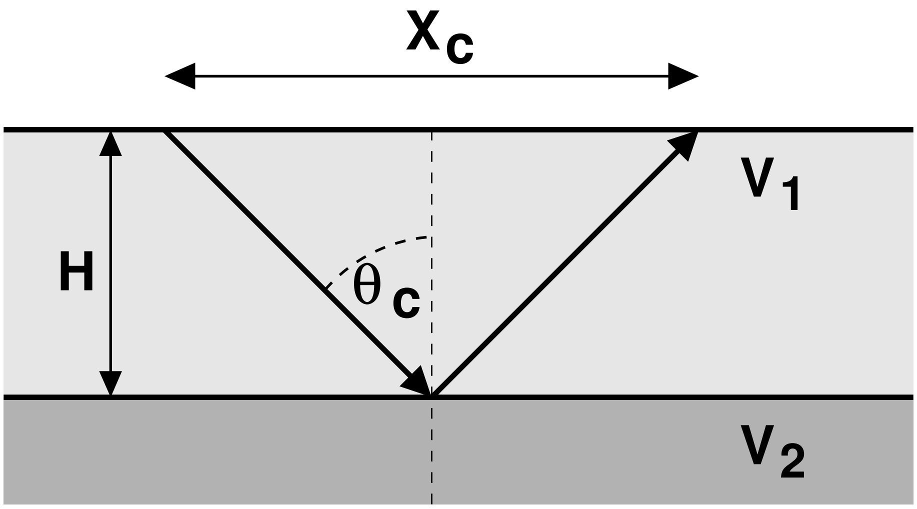

Figure 2.5: The ray path of reflection at the critical offset.

2.5 Conclusions

Spurious waves in practical applications of seismic interferometry are ever present because strict requirements for the exact recovery of the Green function between receivers cannot be met in practice. Here we present an artifact we call the virtual refraction in a two-layered model. We estimate the velocity of the bottom layer from its slope and the critical offset from the stationary phase point in the correlation gather between receivers. With the critical time picked on the real shot record, the real and virtual refractions provide enough information to estimate wave speeds and interface depth. Finally, the virtual refraction intercepts at the origin and is the direct result of stacking multiple sources. These characteristics potentially provide robustness in the presence of noise and make identification in the virtual shot record straightforward.

CHAPTER 3:

CHARACTERIZING AN AQUIFER WITH THE VIRTUAL REFRACTION

Summary

Instead of attempting to suppress the virtual refraction during application of seismic interferometry, we show how this spurious energy contains information about the subsurface. We present an application of the analysis developed in Chapter 2 to field data. We use data collected at the Boise Hydrogeophysical Research Site (BHRS) to determine relative water table depth and seismic-wave velocities. By forming a virtual shot record we suppress uncorrelated noise and produce a virtual refraction that intercepts zero offset at zero time. These features make the virtual refraction velocity straightforward to estimate. The stationary-phase point associated with the correlation between the reflected and refracted waves from the interface identifies the critical offset and allows us to estimate the top layer thickness and velocity. This field data example can also be found in Nichols *et al.* (2010).

3.1 Introduction

We present the first application of the analysis developed in Chapter 2 to field data. We use data collected at the Boise Hydrogeophysical Research Site (BHRS) to determine relative water table depth and seismic-wave velocities. The BHRS is a research site located 15 km southeast of Boise, Idaho (USA), developed to study the permeability and other properties of heterogeneous aquifers using hydrogeological and geophysical methods (Barrash *et al.*, 1999; Clement *et al.*, 1999). In 1997 and 1998, eighteen wells were drilled to aid in the collection of hydrologic, geophysical, and well log data. The stratigraphy of the upper 20 m at the BHRS consists of coarse fluvial deposits (silts and sands). The coarse fluvial deposits include layering and variations, such as lenses, within some of the sediment packages (Barrash and Clemo, 2002; Barrash and Reboulet, 2004). A local quarry exposure shows a succession of fluvial deposits (Figure 3.1) that is similar to the top 20 m of sediment at the BHRS. Hydraulic conductivity can vary significantly within the shallow aquifer at the BHRS, having an effect on the seismic velocities. However, the seismic velocity contrast is greatest between unsaturated and saturated sediments (i.e., above and below the water table). The geology is unknown in detail below the shallow fluvial aquifer. However, a clay layer appears continuous at 20 m depth at the BHRS based on drilling (Barrash and Clemo, 2002). Drilling data indicate the clay is at least 3 m thick. A vertical seismic profile (VSP) survey at the BHRS shows P-wave velocities above and below the water table to about 20 m depth are approximately 400 m/s and 2700 m/s, respectively (Moret *et al.*, 2004). Based on this information and other hydrologic and geophysical surveys conducted at the BHRS (Barrash *et al.*, 1999; Clement *et al.*, 1999; Barrash and Clemo, 2002; Barrash and Reboulet, 2004), we

Figure 3.1: Quarry representative of BHRS geology showing: Sand Lenses, Poorly sorted massive units, moderately sorted horizontally bedded units, and trough cross-bedded units. The vertical exposure is ∼6 m.

develop the seismic velocity model shown in Figure 3.2.

3.2 2006 Field Seismic Data

3.2.1 Data Acquisition

The 2006 data were originally collected for a reflection tomography study and to introduce students to seismic data collection. The 2006 survey was a 187 m 2D profile passing through the northeastern section of the wells (Figure 3.3). The source was a hitch-mounted, accelerated 100 lb. weight, dropped onto a steel plate. We

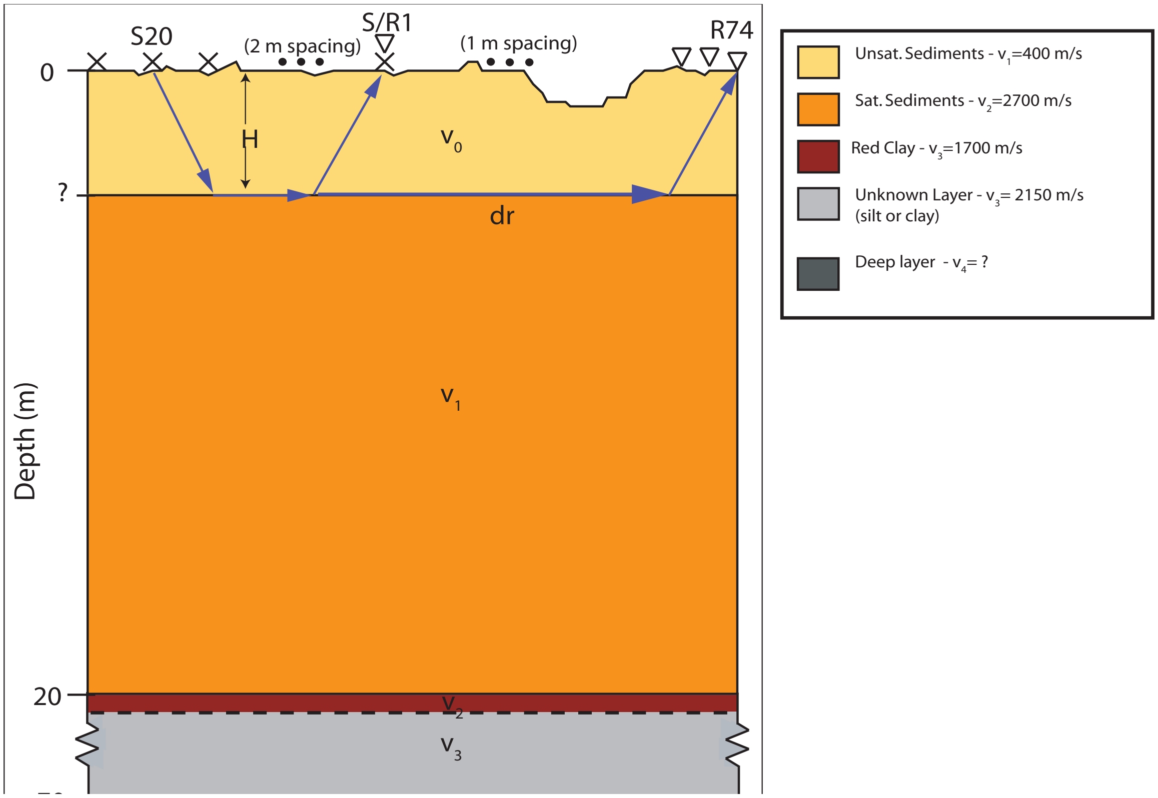

Figure 3.2: The P-wave velocity model representing the geology of the BHRS where the 2006 survey was conducted. The elevation profile showing the 1 m dip was collected using a differential GPS.

recorded for 1 s after each shot, sampling at 0.5 ms on 120 10 Hz vertical-component geophones. Five shots at each location were averaged to increase the signal-to-noise ratio. Receivers were placed every meter and sources every two meters. The survey geometry is shown in Figure 3.3. Because seismic refraction interferometry requires data collected at long source-receiver offsets, in the following analysis we consider sources off the Northwest end of the line that give us the greatest offset from receivers..

Since the refractions contain higher frequencies than the surface waves, we tried different filters to suppress the groundroll. We found that a trapezoidal bandpass filter defined with corners at 75-150-300-600 Hz works well to suppress groundroll. We also applied a centered root-mean-square Automatic Gain Control (AGC) (e.g., p. 85 in Yilmaz, 2001) with a window of 50 ms to boost the refraction amplitude relative to the slower groundroll. A processed shot gather from a source colocated at the first receiver is shown in Figure 3.4a. The surface-wave and air-wave amplitudes are reduced by the filter, but residual energy is visible (blue dashed line). The P-wave refraction from the water table is seen between 0.02 s and 0.05 s (red dashed line). Note that the direct and reflected waves are not obvious, thus making conventional refraction analysis difficult. Between 40 m and 60 m offset, there is a $\sim$2 ms pull-up in the refraction. Using V_1=400 m/s, the pull up corresponds to a 1 m dip, which is confirmed by the surface topography profile, obtained with a differential Global Positioning System (GPS) (Figure 3.2). The data also show ambient noise arriving before the refraction, particularly at the far offsets.

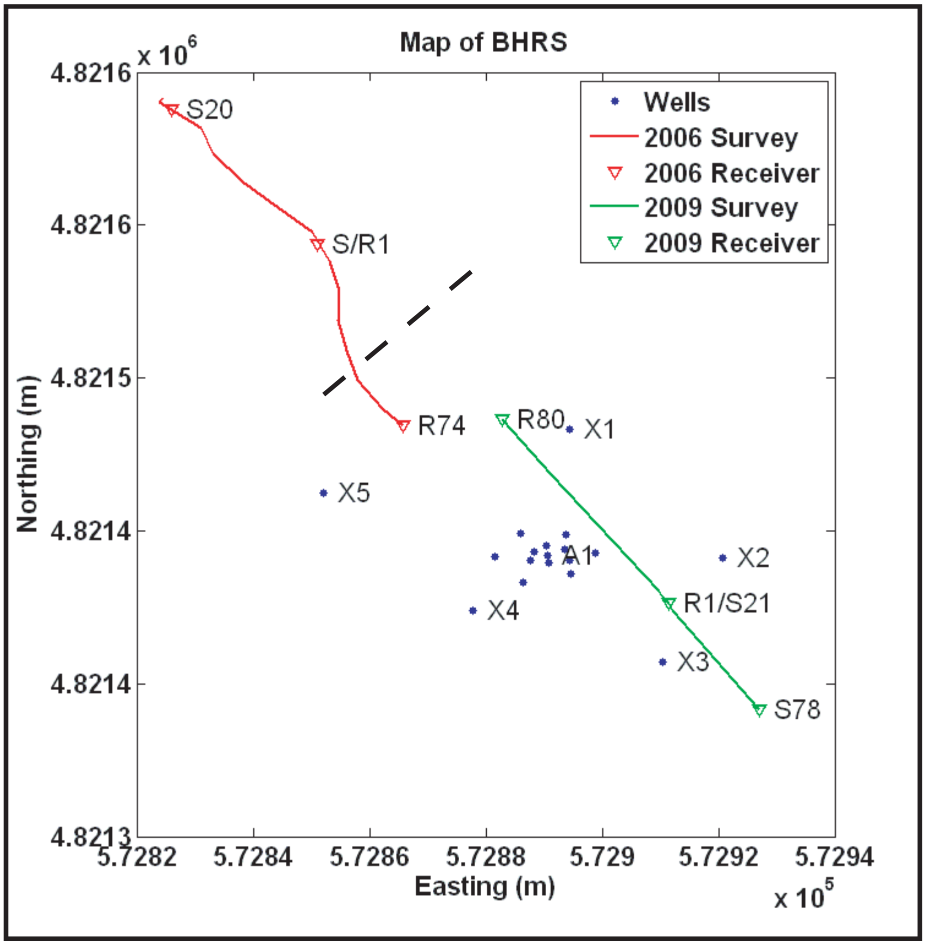

Figure 3.3: Plan view of the BHRS. Survey geometry for the 2006 (red line) and 2009 (green line) 2D seismic lines at BHRS. Dashed line indicates the 1 m topographic dip in the 2006 line. We used variable spacing in the section where sources and receivers intersect in the 2009 line (described in detail in Section 3.3.1). The blue dots are the wells at the BHRS.

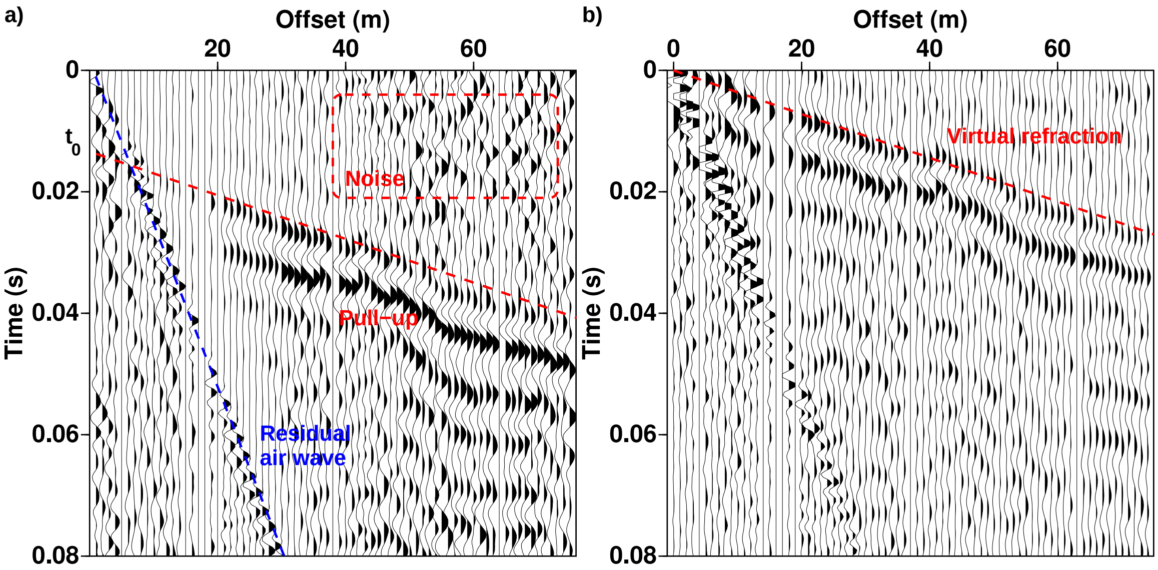

Figure 3.4: a) Shot record for the source at S2. The data are filtered and gained. b) Virtual shot record produced from seismic interferometry. The virtual refraction intercepts t=0 s at zero offset and has a velocity of 2700 m/s.

3.2.2 The Virtual Shot Record

Following Equation 2.3, we cross-correlate wavefields recorded at receiver R1 with wavefields recorded at receivers R1 to R74, for shots at positions S1 to S20. Summing the cross-correlations for all 20 sources produces a virtual shot at receiver R1 (Figure 3.4b). While this is an elastic medium, we only record the vertical component of the wavefield, and consider only the pure P-wave refraction. Therefore, it is kinematically equivalent to the acoustic numerical example shown in Chapter 2.

The high amplitude and coherent event in Figure 3.4b is the virtual refraction (red dashed line). The virtual refraction has an average velocity V_2 =2700 m/s, which agrees well with the previous P-wave velocity estimate in saturated sand (Moret *et al.*, 2004). This is the identical moveout as the refraction in the real shot record. The pull up due to the surface topography can be seen in both the real shot record and the virtual shot record. The virtual refraction always intercepts zero offset at zero time. Therefore, it is relatively straightforward to pick the virtual refraction on the virtual shot record. Additionally, the uncorrelated noise before the refraction has been suppressed due to the summation over sources in seismic interferometry.

3.2.3 Stationary-Phase Point

Figure 3.5 shows the correlation gather for receivers R1 and R74 for S1 to S20. We observe the correlation of the refracted wave at R1 and the refracted wave at R74 at $t \sim 0.035$ s for large offsets. While we see the constant correlation between both refracted waves for large-offset sources, we do not see the stationary-phase point from the correlation of the refracted wave at R74 with the reflected wave at R1, as we do in the numerical data (right panel of Figure 2.4). Since we do not observe the stationary-phase point in the correlation gather, we do not know X_c. This in turn prevents the determination of V_1 and H using Equations 2.7 and 2.6, respectively. Instead, we calculate the critical offset using our model values:

$$\begin{gathered}\theta_c = \arcsin\left(\frac{V_2}{V_1}\right) = \arcsin\left(\frac{400}{2700}\right) = 8.5 \Leftarrow \\ X_c = 2H\tan\left(\theta_c\right) = 8\tan\left(8.5^o\right) = 1.2\ m.\end{gathered} \tag{3.1}$$

With the 2 m shot spacing being larger than the critical offset, the stationary-phase point is contained within the first offset. The spatial resolution of this survey is too low to see the stationary-phase point, preventing us from determining X_c, V_1, and H using the virtual shot record. To observe the stationary-phase point, we conducted a second seismic survey with finer receiver and shot spacing.

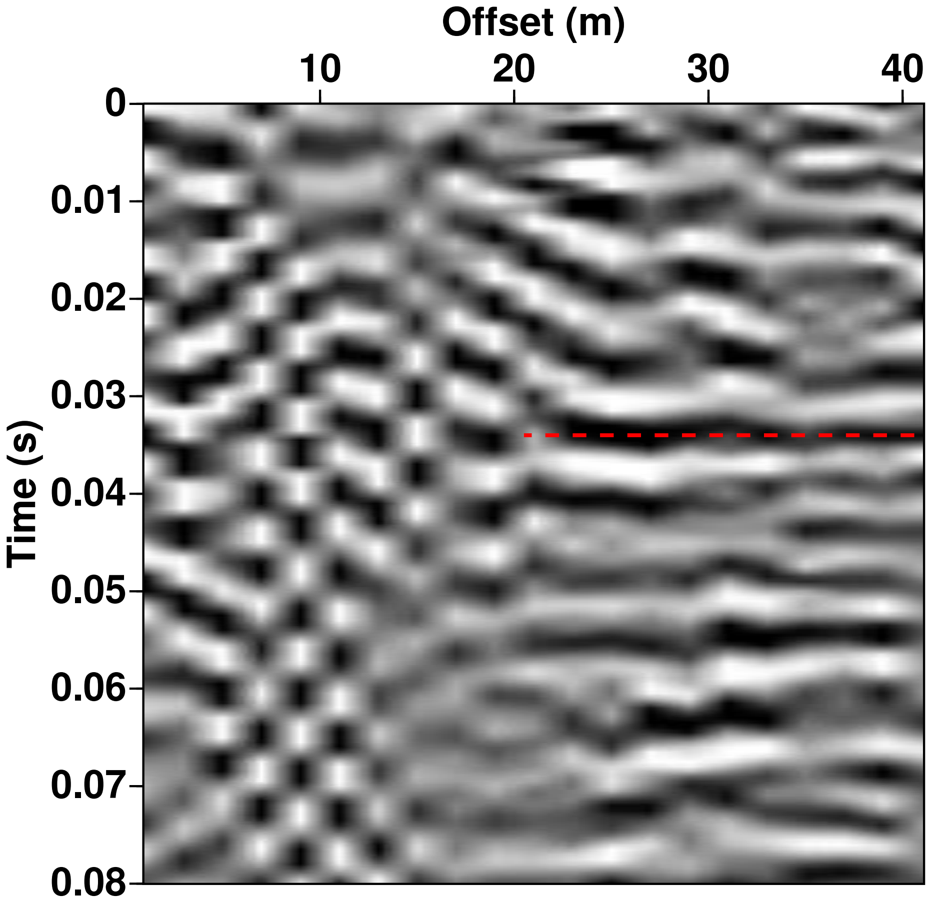

Figure 3.5: Correlation gather between R1 and R74 from 2006 BHRS data. The horizontal band at $t \sim 0.035$ s (red dashed line) is caused by the correlation of refracted waves at both receivers. The correlation of reflected and refracted waves is not obvious with this source sampling so we cannot pick the stationary-phase point to get the critical offset.

3.3 2009 Field Seismic Data

3.3.1 Data Acquisition

In May 2009, we designed and conducted a second 2D seismic survey at the Boise Hydrogeophysical Research Site (BHRS). The survey line was 86 m long, located on horizontal ground near the 2006 survey (Figure 3.3). We recorded on 91 variably spaced 100 Hz vertical-component geophones. The variable spacing gave better resolution near the critical offset while allowing us to record greater offsets. There were 74 receivers with 1 m spacing. On the end nearest the sources, we placed 17 receivers with 0.25 m spacing. Our source was a 4 lb. sledge hammer. Starting at the first receiver, we stacked 4 shots every 0.1 m for the first 2 m, while moving away from the receiver array. We then increased the shot spacing to 1 m, for another 38 m. We recorded for 0.5 s with a sampling interval of 0.25 ms.

We applied the same data processing as in the 2006 data example to suppress the groundroll and air wave while highlighting the water table refraction event. Figure 3.6a is the shot record from the source at S21 with the bandpass filter and AGC applied. We plotted only the regularly spaced receivers (i.e., 1 m) in Figure 3.6a. As with the 2006 data, we observed a refraction from the water table (red line), along with residual groundroll and air-wave energy. Variation in the refraction arrival time is caused by the intermittent lenses and inclusions in the dry sediment (Figure 3.1). What appeared to be multiples are likely reflections from below the clay layer. The background noise level is also larger because the 4 lb. sledge hammer is a much weaker source than the weight drop.

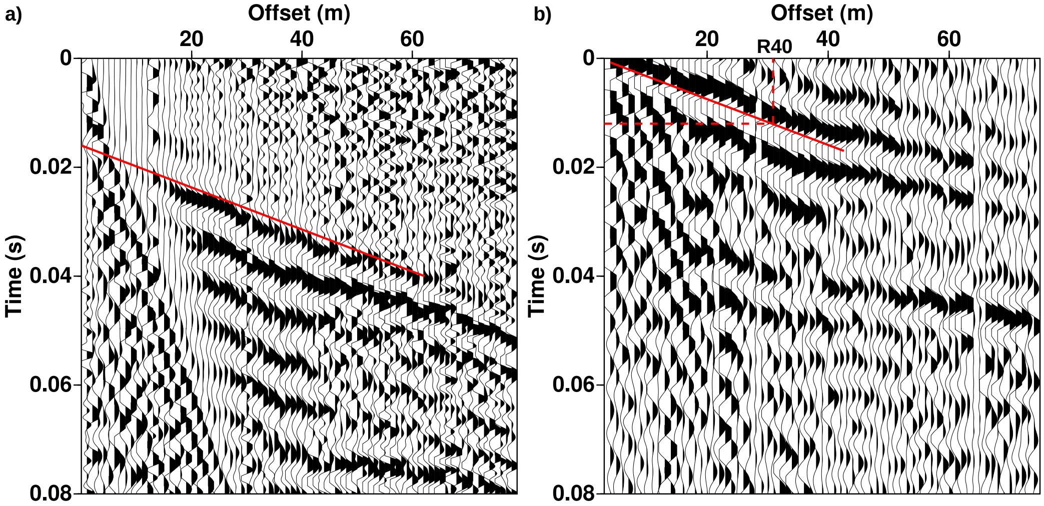

Figure 3.6: a) Example shot record from source at S21. The data are filtered and gained to suppress the groundroll and air wave. b) Virtual shot record produced by seismic interferometry. Note the virtual refraction intercepts t =0 s and has a velocity of 2700 m/s. R40 is the receiver correlated with R1 to produce the correlation gather in Figure 3.7. The virtual refraction arrives at R40 at $t \sim 0.01$ s.

3.3.2 The Virtual Shot Record

Using the same procedure as for the 2006 data, we cross-correlate the wavefield recorded at R1 with the wavefields at the other 90 receivers. We then sum the cross-correlations from sources S21 to S78 to produce a virtual shot record (Figure 3.6b). Since there is irregular source spacing, care must be taken to multiply the terms in the summation by their corresponding source spacing (dS in the integral Equation 2.3). Again we see the virtual refraction with velocity V_2 =2700 m/s. The refraction decreases in amplitude at long offsets due to a lack of source energy in the 4 lb. hammer; this is visible in both the real and virtual shot records.

3.3.3 Stationary-Phase Point

We change to a trapezoidal bandpass filter with corner frequencies 30-75-150-300 Hz. This reduces the ringyness and emphasizes the cross-correlation of the refracted wave with the reflected wave from the water table in the correlation gather. By cross-correlating wavefields from R1 and R40 for all sources, we create a correlation gather (Figure 3.7). The correlation gather has a variable scale along the horizontal axis to highlight the stationary-phase point. We observe the stationary-phase point from the correlation of the water table reflection at R1 and the water table refraction at R40 at X_c =1.3 m. We also observe the flat feature at far offsets, at t ∼0.01 s resulting from the correlation of the refracted wave at R1 and the refracted wave at R40. The lack of coherency between 5 m and 22 m offsets is caused by correlations involving residual groundroll not completely remove by the bandpass filter.

We know V_2 =2700 m/s from the virtual shot record. We can use the real shot record to pick the critical time T_c =0.0185 s at X_c. Using Equations 2.7 and 2.6, we find that V_1 =440 m/s and H =3.9 m. For comparison, a conventional refraction analysis requires the intercept time and the upper and lower layer velocities to estimate H. Looking back to the real shot record with a source at the first receiver, we estimate the refraction intercept time is T_i =0.018 s. Because we do not observe the direct wave, we use V_1 =440 m/s (Moret *et al.*, 2004). The velocity of the faster layer V_2 =2700 m/s can be estimated from the slope of the real refraction. Calculating the depth to interface using (Equation 3-41a in Yilmaz, 2001):

$$H = \frac{V_1 V_2 T_i}{2\sqrt{V_2^2 - V_1^2}}, \tag{3.2}$$

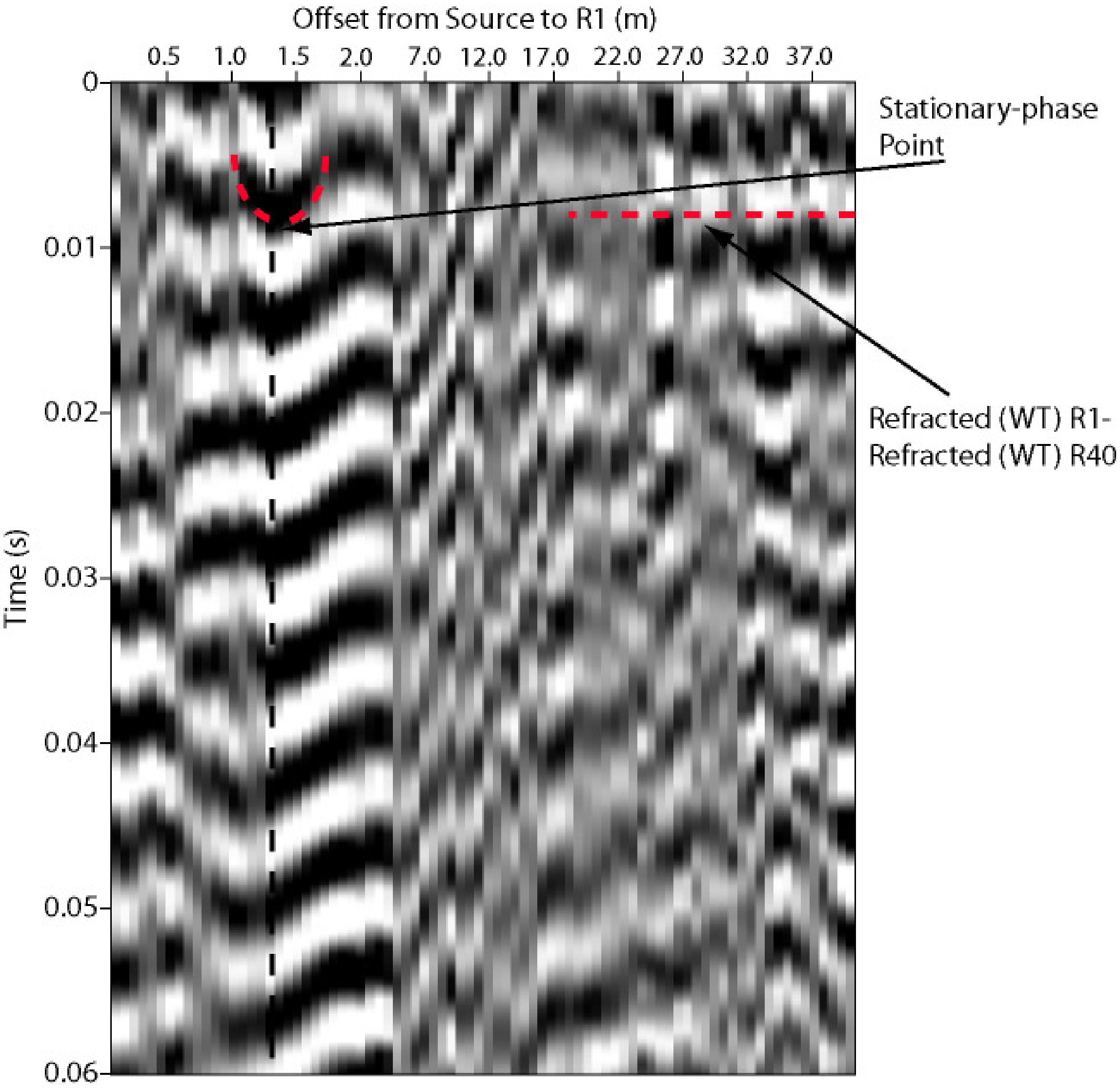

Figure 3.7: Correlation gather of R1 and R40. The correlations of the refracted wave at R40 with the refracted and the reflected waves at R1 are highlighted in red. The critical offset (X_c) is denoted with the black dashed line. Note the change in offset scale at 2 m.

yields H =4.0 m. Traditional and interferometric refraction analysis are in agreement. We note that the virtual refraction method does not explicitly need an estimate of V_1, but both traditional and interferometric methods require user interpretation to pick the values going into estimates of V_1 and H. In the example shown here, V_1 matches well with Moret *et al.* (2004), but H is slightly larger than estimates using an electric tape measurement (Johnson, 2011) near the time of data collection. This is analyzed in the next chapter.

3.4 Discussion

Survey geometry plays a key role in the effectiveness of the virtual refraction method in determining subsurface parameters. For example, we could obtain only the saturated P-wave speed from the 2006 survey due to the coarse source spacing near the critical offset. The 2009 survey was designed specifically to have high resolution around the critical offset, but to also record long offsets. The best way to achieve this was to vary the source and receiver spacing. This was a particular case where the refracting interface is very shallow and has a strong velocity contrast. It is important to remember that the virtual refraction method does not require regular spacing between sources or receivers, only that the survey geometry is known. However, for irregular spacing, the terms within the interferometric integral must be multiplied by the corresponding distance dS between sources. The other difference between the 2006 and 2009 surveys is the type of source. While the accelerated weight drop used in the 2006 survey produced a more consistent and higher-amplitude head wave, the small sledge hammer was used in the 2009 survey to obtain the fine source spacing needed to resolve the stationary-phase point in the correlation gather. Note that both sources produced similar quality virtual shot records due to the summing involved in seismic interferometry.

Another factor contributing to effective use of the virtual refraction method is the preprocessing. For the data used in this work, we found that a bandpass filter and an automatic gain control (AGC) best emphasized the refraction while minimizing the groundroll and other near-surface effects. The goal of our preprocessing was to emphasize the reflected and refracted wave from the desired interface. Because our interface was very shallow we found that more aggressive filtering of the groundroll reduced the correlation between the reflected and refracted waves from the water table. Another option to highlight the reflection and refraction would be time windowing. By windowing around the reflected wave at R1, only the correlations with the reflected wave would be present in the virtual shot record and correlation gather (Bakulin and Calvert, 2006). While windowing may help, it would be difficult because we are not able to identify the reflection in the real shot record. However, we are able to observe the virtual refraction in the virtual shot and the correlations in the correlation gather without applying manual mutes.

3.5 Conclusions

By cross-correlating the wavefields of a field survey, we are able to successfully produce the virtual refraction previously demonstrated in the numerical simulations in Chapter 2. The virtual refraction has the velocity of the deeper layer and contains information about the subsurface that cannot always be easily obtained using conventional processing techniques. Using seismic interferometry, we pick the virtual refraction in the virtual shot record, where uncorrelated noise is attenuated and the virtual refraction intercepts zero time at zero offset. We determine the critical offset manually from the stationary-phase point in the correlation gather. By examining the real and virtual shot records and the correlation gather, we determine the P-wave speeds in unsaturated and saturated sand, as well as the relative depth to the water table, using only the refracted and reflected wave modes. This technique is useful, but is open to error because of the manual interpretation. In the next chapter, we present a method to estimate H and V_1 that eliminates the need for manual interpretation.

CHAPTER 4:

SEMBLANCE ANALYSIS ON THE CORRELATION GATHER

Summary

In Chapter 3, we used an artifact in seismic interferometry related to critically refracted waves that allowed us to determine the velocity of the refracting layer. In this chapter, we present a new semblance analysis on the cross-correlation of reflection and refraction energy to estimate the depth and velocity of the slow layer, without the need for manually picking the critical offset in the correlation gather. We illustrate this concept by a numerical example and show that it more accurately describes the water table depth in field data from the Boise Hydrogeophysical Research Site.

4.1 Introduction

The band-limited Green's function between two receivers is retrieved by cross-correlating recorded wavefields from sources located on an enclosing surface around the two receivers. In the far-field approximation, the sum of the frequency-domain Green's function G and the complex conjugate G^* between two stations positioned at $\mathbf{x}_A$ and $\mathbf{x}_B$ is shown in Equation 2.3. This is commonly referred to as the seismic interferometric integral. With the survey geometry illustrated in Figure 4.1, we model the acoustic wavefield for 221 40-Hz Ricker wavelet sources at a 2.5 m interval using the spectral element method (Komatitsch and Vilotte, 1998; Komatitsch and Tromp, 2002). We record the wavefield at 101 receivers spaced 4 m apart. This is a similar numerical experiment as in Chapter 2. The difference here is the notation used as a consequence of the aforementioned semblance method.

The correlation gather is herein defined as the cross-correlations between $\mathbf{x}_A$ and $\mathbf{x}_B$ for all sources, and summing the correlation gather for each receiver $\mathbf{x}_A$, we generate a virtual shot record (Mehta *et al.*, 2008) as though there was a source at $\mathbf{x}_B$. In Chapter 2, we use this model to show that when sources are not in the far-field and do not enclose the receivers, the retrieved virtual shot record contains an artifact related to critically refracted waves. We now use the same model to show an automated approach to characterizing a two-layer subsurface model.

Following Equation 2.3, we cross-correlate every receiver record in the array with the record at $\mathbf{x}_B = \mathbf{x}_1$, the receiver colocated at $\mathbf{s}_1$. Figures 4.2(a) and 4.2(b) show the real and virtual shot records for this model, respectively. The x-axes represent the distance between the real or virtual source at $\mathbf{s}_1 = \mathbf{x}_1$ and a given receiver at $\mathbf{x}_A$. In Figure 4.2(b), we retrieve the direct-wave arrival from the cross-correlation between the direct waves, and the virtual refraction. The arrival time of the virtual refraction is $T_c = dr/V_2$, where dr is the difference in travel path that critically refracted energy travels between the two receivers (Figure 4.1). The virtual refraction

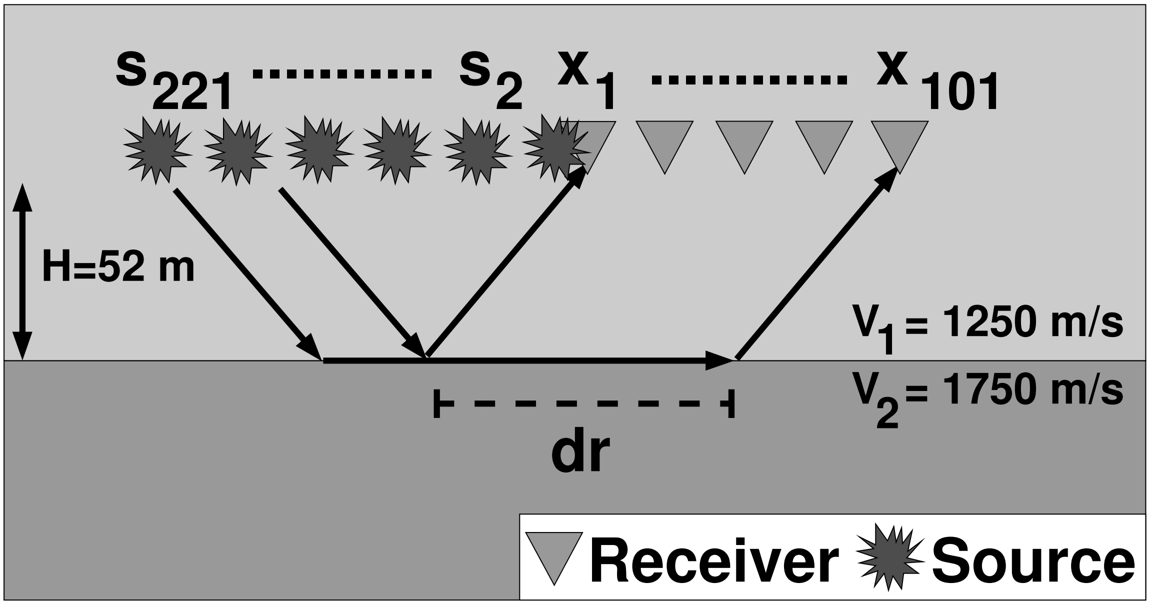

Figure 4.1: Two-layer acoustic model with $V_1 = 1250$ m/s, $V_2 = 1750$ m/s and $H = 52$ m. The source increment is 2.5 m and receiver increment is 4 m.

is produced because of an incomplete source distribution and the far-field radiation approximation inherent within Equation 2.3. The most intuitive reason for the virtual refraction is that cross-correlations of refractions from sources past the critical offset from $\mathbf{x}_1$ (Figure 4.1) sum constructively during seismic interferometry. This energy is constant across the source array (e.g., T_c in Figure 4.3), and therefore, does not sum destructively when summing the cross-correlations over all sources.

Comparing Figures 4.2(a) and 4.2(b), the virtual source recovers little of the reflected wave. This is because the stationary-phase cross-correlations (Snieder, 2004) (i.e., energy that sums constructively for the reflected event) occur near the virtual source at $\mathbf{x}_1$. In this numerical example, we apply a cosine taper to 25% of sources on each side of the source array in the correlation gather before creating the virtual shot record (i.e., $\mathbf{s}_1$ to $\mathbf{s}_{55}$ and $\mathbf{s}_{166}$ to $\mathbf{s}_{221}$). The taper suppresses truncation artifacts

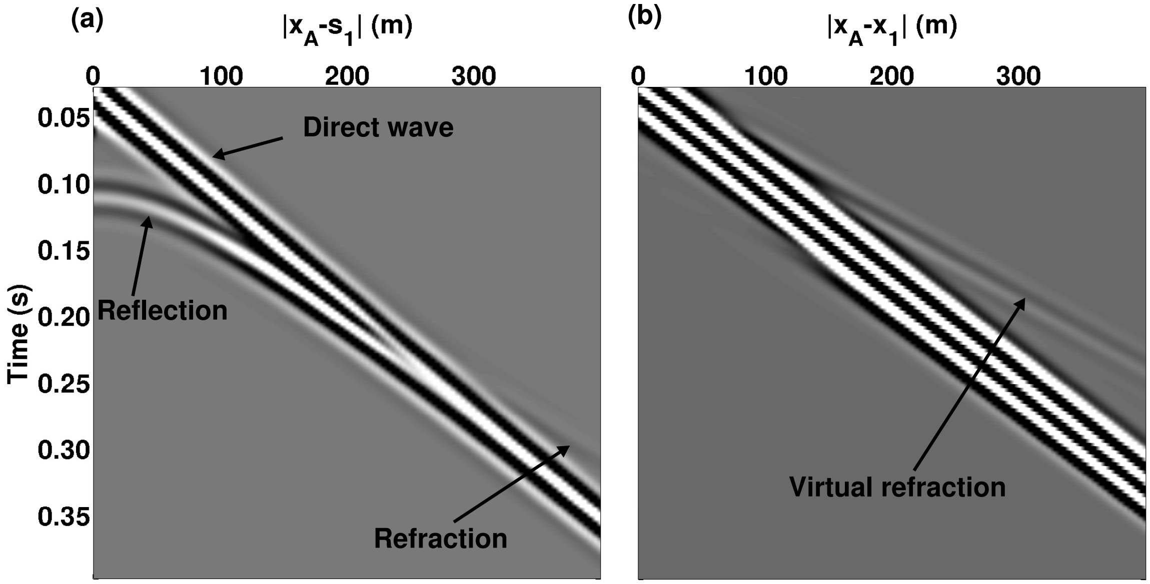

Figure 4.2: Real shot record (a) and virtual shot record (b) for real and virtual sources at $\mathbf{s}_1 = \mathbf{x}_1$. The virtual shot record contains the direct arrival and the virtual refraction artifact indicated by the arrow.

produced from the incomplete source aperture (Snieder *et al.*, 2006).

In conventional refraction analysis, we estimate V_1 and V_2 from the slope of the direct and refracted waves, respectively, and estimate the depth to the interface using Equation 3.2. The virtual refraction, on the other hand, has an intercept time $T_i = 0$ s. Therefore, in Chapter 3, we extracted H and V_1 by estimating V_2 from the moveout of the virtual refraction and picking the critical offset (X_c) in the cross-correlation gather. However, estimating X_c manually can prove difficult in noisy field data. In the next section, we present an alternative and robust method to estimate V_1 and H by maximizing the semblance of the energy in the correlation gather related to this virtual refraction. Finally, we apply this method to estimate the corresponding subsurface properties at the Boise Hydrogeophysical Research Site; a site where standard refraction methods are difficult because groundroll and the air

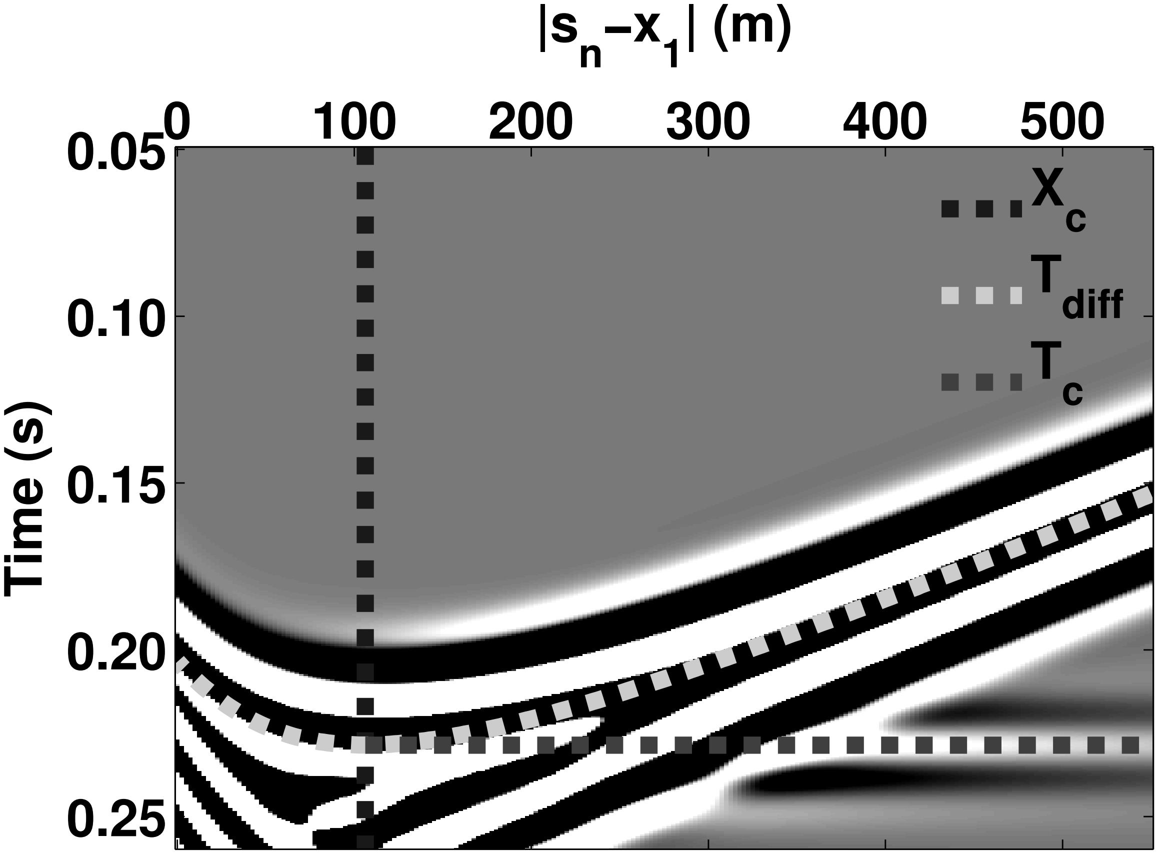

Figure 4.3: Correlation gather for $|\mathbf{x}_{101} - \mathbf{x}_1| = 400$ m. The critical offset X_c occurs at the maximum of T_{diff}. T_c is the cross-correlation between the refractions at both receivers and is equal to $\frac{|\mathbf{x}_{101}-\mathbf{x}_1|}{V_2}$ in this model.

wave mask the direct wave and the shallow water table reflection.

4.2 Velocity and Depth Estimation in the Cross-correlation Domain

We propose a semblance method of the correlation gather to estimate V_1 and H, similar to King *et al.* (2011) and Poliannikov and Willis (2011), but focused on the virtual refraction. Figure 4.3 shows the correlation gather for $|\mathbf{x}_{101} - \mathbf{x}_1| = 400$ m for all sources in Figure 4.1. The cross-correlation between the reflection at $\mathbf{x}_B$ and the refraction at $\mathbf{x}_A$ yields T_{diff}. We annotate the curve T_{diff} in Figure 4.3 as well as indicate the critical offset, X_c, and the cross-correlation between the refractions at both receivers, T_c.

For a linear source array, we showed in Chapter 2 that the maximum of T_{diff} occurs at the critical offset X_c from receiver $\mathbf{x}_B$. The travel-time difference curve T_{diff} from a source at $\mathbf{s}_n$ is

$$T_{diff}(\mathbf{x}_A, \mathbf{x}_B) = T_{refr}(\mathbf{x}_A, \mathbf{s}_n) - T_{refl}(\mathbf{x}_B, \mathbf{s}_n), \tag{4.1}$$

where the reflection arrival time is

$$T_{refl}(\mathbf{x}_B, \mathbf{s}_n) = \sqrt{\left(\frac{|\mathbf{x}_B - \mathbf{s}_n|}{V_1}\right)^2 + \left(\frac{2H}{V_1}\right)^2}, \tag{4.2}$$

and the refraction arrival time is

$$T_{refr}(\mathbf{x}_A, \mathbf{s}_n) = \frac{2H\cos\theta_c}{V_1} + \frac{|\mathbf{x}_A - \mathbf{s}_n|}{V_2} \tag{4.3}$$

(derived from Equation 8, Section 3.2 in Stein and Wysession, 2003). A full derivation of Equation 4.3 is given in Appendix A. The parameters in Equations 4.2 and 4.3 are defined in Figure 4.1, and Snell's Law relates the model velocities to the critical angle, $\sin(\theta_c) = \frac{V_1}{V_2}$. With $|\mathbf{x}_A - \mathbf{s}_n| = |\mathbf{x}_B - \mathbf{s}_n| + |\mathbf{x}_A - \mathbf{x}_B|$, Equation 4.1 becomes

$$T_{diff}(\mathbf{x}_A, \mathbf{x}_B) = T_{refr}(\mathbf{x}_B, \mathbf{s}_n) - T_{refl}(\mathbf{x}_B, \mathbf{s}_n) + \frac{|\mathbf{x}_A - \mathbf{x}_B|}{V_2}. \tag{4.4}$$

We propose to calculate the T_{diff} curve for combinations of V_1 and H for all $|\mathbf{x}_B - \mathbf{s}_n|$, taking V_2 from the slope of the virtual refraction.

We define the semblance as

$$S_{ij} = \frac{E_{i,j}^{out}}{N \times E_{i,j}^{in}}, \tag{4.5}$$

where N is the number of sources in the correlation gather and i and j represent a given V_1 and H, respectively. The numerator and denominator are the output (E^{out}) and input (E^{in}) energies (Neidell and Taner, 1971) around the arrival of T_{diff}:

$$E_{i,j}^{out} = \sum_{n=1}^{N} \left(\sum_{t=T_{diff}(i,j,n)-t_w/2}^{T_{diff}(i,j,n)+t_w/2} C(\mathbf{x}_A, \mathbf{x}_B, \mathbf{s}_n, t) \right)^2 \tag{4.6}$$

and

$$E_{i,j}^{in} = \sum_{n=1}^{N} \left(\sum_{t=T_{diff}(i,j,n)-t_w/2}^{T_{diff}(i,j,n)+t_w/2} C^2(\mathbf{x}_A, \mathbf{x}_B, \mathbf{s}_n, t) \right), \tag{4.7}$$

where C is the cross-correlated wavefield at $\mathbf{x}_A$ and $\mathbf{x}_B$ for source $\mathbf{s}_n$, and t_w is a user-defined time window. Noting that a larger time window will increase stability at the cost of resolution (Poliannikov and Willis, 2011), we use t_w=10 ms in the following examples and compute S_{ij} over a range of V_1 and H values.

4.2.1 Numerical Data Example

Figure 4.4 shows correlation gathers for different receivers at $\mathbf{x}_A$ cross-correlated with the virtual source receiver at $\mathbf{x}_1$. The correlation gathers in Figure 4.4 are not tapered. From (a) to (c), the distance $|\mathbf{x}_A - \mathbf{x}_1|$ increases. At smaller $|\mathbf{x}_A - \mathbf{x}_1|$, the cross-correlations of other wave modes overlap T_{diff}. However, as $|\mathbf{x}_A - \mathbf{x}_1|$ increases, T_{diff} separates from the other events. Note that Figure 4.3 shows a windowed portion of Figure 4.4(c) with the amplitudes gained such that T_c is visible. Figure 4.5 shows the semblance for the correlation gathers in Figure 4.4. It is apparent from Figure 4.5 that T_{diff} must be isolated in time and space in order for the semblance to accurately estimate H and V_1. For $|\mathbf{x}_A - \mathbf{x}_1| < 200$ m, the semblance estimates incorrect values. The correct velocity and depth values in this model as indicated by the star are $V_1 = 1250$ m/s and $H = 52$ m.

4.2.2 Stacking Semblance Panels

The maximum semblance offers an estimate of the velocity and depth of the top layer between X_c and $\mathbf{x}_1$. In our laterally homogeneous model, the semblance estimate is independent of $\mathbf{x}_A$. Thus, we can stack semblance panels from many $|\mathbf{x}_A - \mathbf{x}_1|$ to increase the signal-to-noise ratio (S/N). Figure 4.6(a) shows the cross-correlation gather for $|\mathbf{x}_{101} - \mathbf{x}_1| = 400$ m. We add random zero-mean Gaussian noise to the shot gathers before cross-correlation. Figure 4.6(a) shows that only cross-correlations related to the large amplitude direct wave are coherent, and the T_{diff} energy is not.

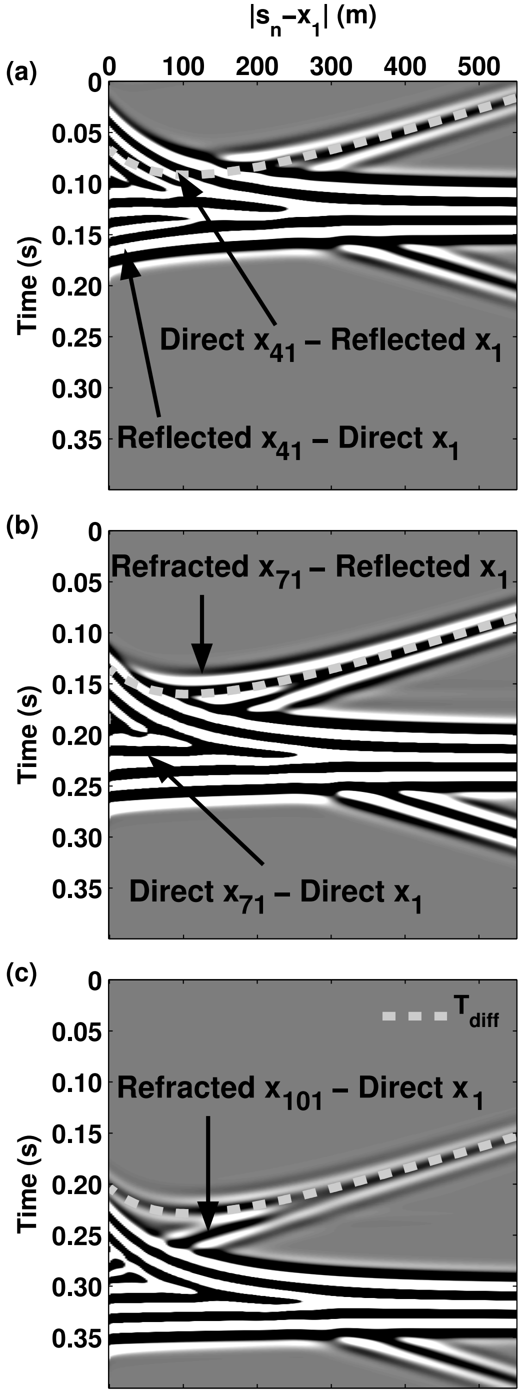

Figure 4.4: Cross-correlation gathers for $|\mathbf{x}_{41} - \mathbf{x}_1|$=160 m (a), $|\mathbf{x}_{71} - \mathbf{x}_1|$=280 m (b), and $|\mathbf{x}_{101} - \mathbf{x}_1|$=400 m (c). As $|\mathbf{x}_A - \mathbf{x}_1|$ increases, T_{diff} becomes isolated in time and space.

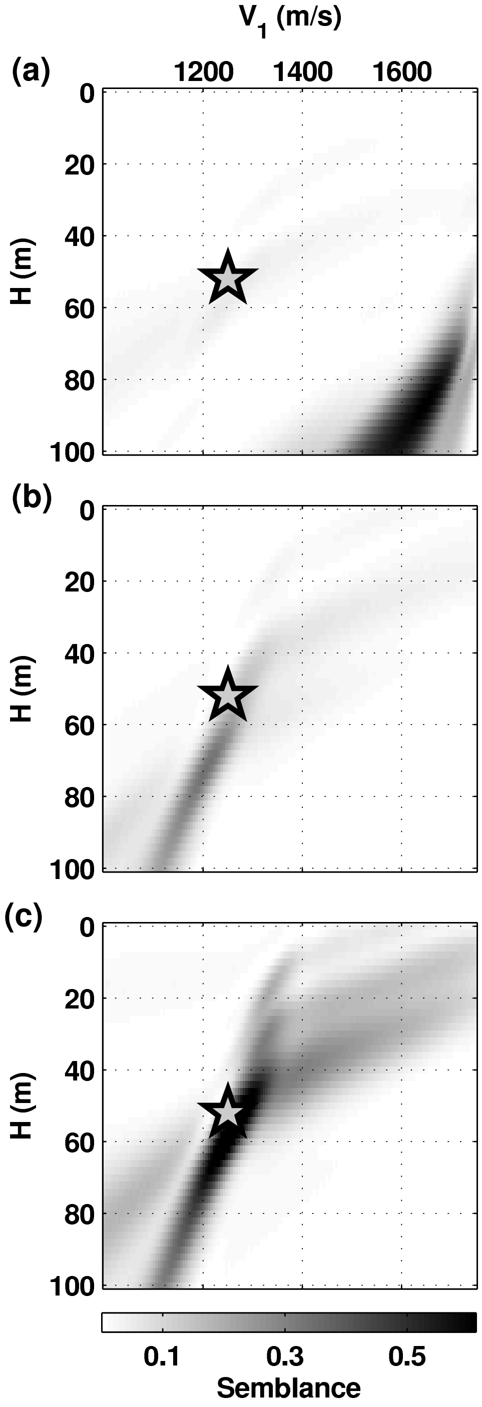

Figure 4.5: Semblance panels for $|\mathbf{x}_{41} - \mathbf{x}_1|$=160 m (a), $|\mathbf{x}_{71} - \mathbf{x}_1|$=280 m (b), and $|\mathbf{x}_{101} - \mathbf{x}_1|$=400 m (c). The star indicates the correct model parameters.

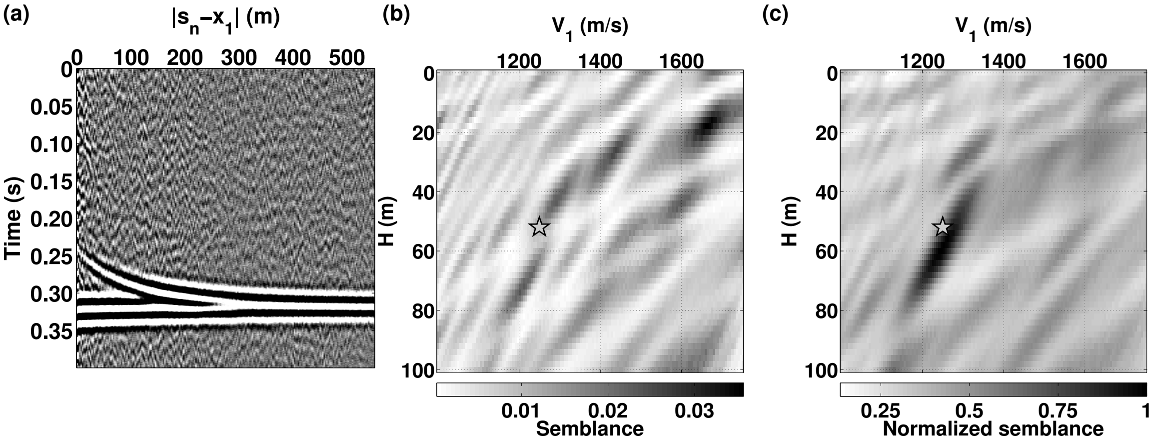

Figure 4.6: (a) Cross-correlation gather for $|\mathbf{x}_{101}-\mathbf{x}_1| = 400$ m. We add random zero-mean Gaussian noise before cross-correlation so that T_{diff} is no longer visible. (b) Semblance panel for the cross-correlation gather. (c) Semblance panel after stacking 20 semblance panels from $|\mathbf{x}_{81} - \mathbf{x}_1|$=320 m to $|\mathbf{x}_{101} - \mathbf{x}_1|$=400 m.

The semblance of this correlation gather (Figure 4.6(b)) is equally hard to interpret. However, Figure 4.6(c) is the semblance after stacking 20 individual semblance panels from $|\mathbf{x}_{81} - \mathbf{x}_1| = 320$ m to $|\mathbf{x}_{101} - \mathbf{x}_1| = 400$ m. The maximum semblance in the stacked panel occurs at $V_1 = 1250$ m/s and $H = 58$ m. The maximum semblance estimates the true value of V_1 while estimating H to within 11.5%. The stars in Figures 4.6(b) and (c) indicate the true model parameters.

4.3 Field Data Example

The Boise Hydrogeophysical Research Site (BHRS) is a research site near Boise, Idaho (USA), developed to study the properties of heterogeneous aquifers using hydrogeological and geophysical tools (Barrash *et al.*, 1999). Figure 4.7 is a model of the top 4 m at the BHRS showing vertical hammer source and vertical component geophone locations, spaced at a 1-m interval. Based on electronic tape measurements at the

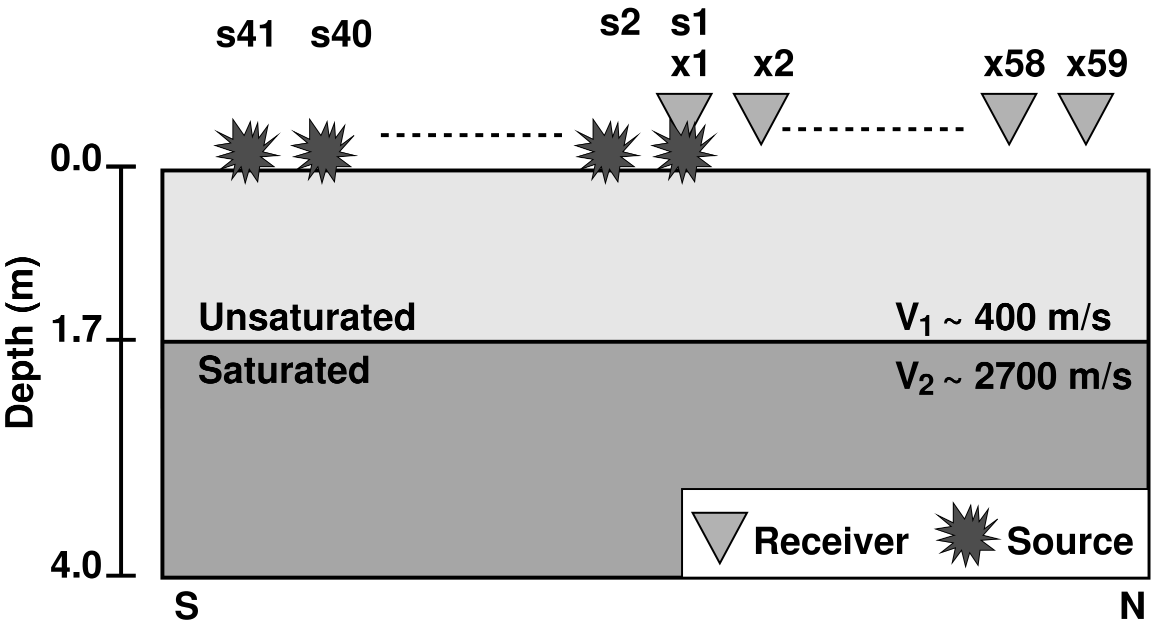

Figure 4.7: Boise Hydrogeophysical Research Site seismic model. Source and receiver spacing is 1 m.

time of seismic acquisition in well X3 (Figure 3.3), approximately 10 m from the receiver array, Johnson (2011) estimates the water table depth during data collection in 2009 to be approximately 1.7 m below the ground surface. The saturated sand below the water table has a larger P-wave velocity than the unsaturated sand above (Moret *et al.*, 2004). In Chapter 3, we extracted H and V_1 by picking the critical offset X_c in the correlation gather and estimating V_2 from the moveout of the virtual refraction. This proved to be difficult and conducive to error by the interpreter. In the following, we compare our semblance approach to the approach used in Chapter 3 for the 2009 seismic data.

Figure 4.8(a) shows the trace-normalized shot record for source $\mathbf{s}_1$ and offers insight into why our semblance approach or the approach in Chapter 3 might be better suited than conventional refraction methods for characterizing the water table. This

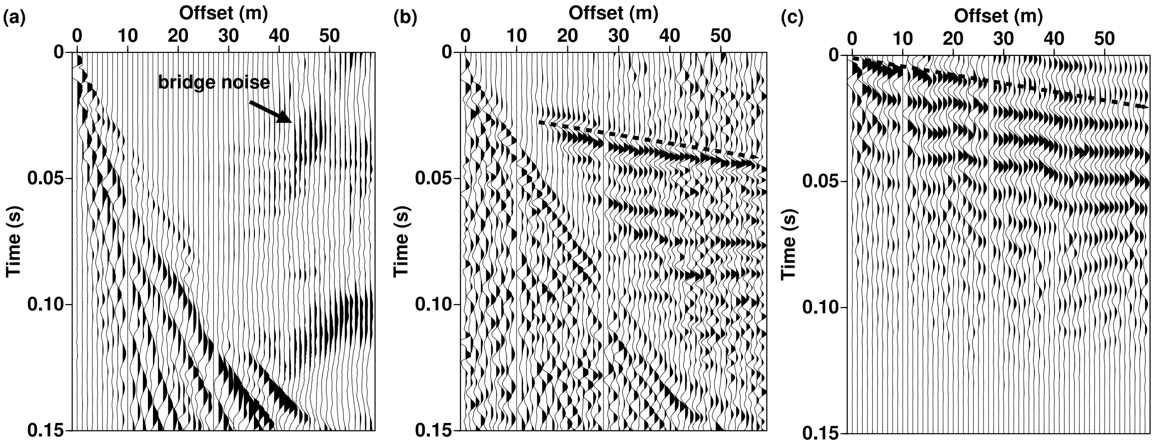

Figure 4.8: (a) Trace-normalized shot record from a sledge-hammer source at the first receiver location. (b) AGC and bandpass filtered shot record–dash indicates water table refraction. (c) Trace-normalized virtual shot record–dash indicates virtual refraction.

shot record is dominated by dispersive groundroll and coherent low-frequency noise from a bridge column located approximately 100 m North of the receiver array. To suppress the groundroll and bridge noise, we apply a zero-phase trapezoidal filter with corner frequencies 50, 100, 200, 400 Hz, and a root-mean-square Automatic Gain Control (e.g., p. 85 in Yilmaz, 2001) with a window of 0.05 s (Figure 4.8(b)). A coherent refraction from the water table is annotated, but remaining groundroll and a shallow water table at this site make it difficult to identify a direct or reflected wave. Without the direct wave, we cannot estimate V_1 or H using the conventional refraction method described in Section 4.1.

In Chapter 3, we performed seismic interferometry and used the correlation gather to manually pick X_c at the maximum of T_{diff}. We apply seismic interferometry to the shot records after applying the processing shown in Figure 4.8(b). Figure 4.8(c) is the virtual shot record created using the same tapering procedure as in the numerical data example. The virtual refraction is the dominant arrival that crosses the origin at zero offset. The virtual refraction has the same linear moveout as the real refraction in (b). To estimate V_2, we take the approach of King and Curtis (2011) and pick the maximum slowness (p) at τ=0 s after transforming the virtual shot record to the τ-p domain (e.g., p. 923 in Yilmaz, 2001). The maximum p at τ=0 gives a virtual refraction velocity of 2778 m/s. The dashed line in Figure 4.8(c) defines this moveout velocity in the shot domain. This estimate of V_2 agrees with the saturated velocity estimate of 2700 m/s from Chapter 3 and Moret *et al.* (2004).

From here our approach differs from Chapter 3 in how we estimate the top-layer depth and velocity. We perform a semblance analysis on the correlation gather; first normalizing each trace in the correlation gather. We stack 30 semblance panels over the largest offsets ranging from $|\mathbf{x}_{29} - \mathbf{x}_1|$= 28 m to $|\mathbf{x}_{59} - \mathbf{x}_1|$=58 m and estimate V_1 and H from the maximum semblance. Figure 4.9 shows the summed semblance panel with maximum semblance at 1.9 m and 395 m/s (white star). The black star denotes the estimate from Chapter 3 and the dashed line indicates the water table depth from Johnson (2011). Taking V_1=400 m/s from Moret *et al.* (2004) and H=1.7 m from direct measurements by Johnson (2011), we estimate V_1 within $\frac{|395-400|}{400} \approx 1\%$ and H within $\frac{|1.9-1.7|}{1.7} \approx 11\%$.

4.4 Discussion

Both in the numerical and field data examples, it appears that our estimates of V_1 and H are correlated. This can be seen in the Equations 4.1 through 4.4, where the term $2H/V_1$ appears repeatedly. V_1 appears independent from H once in these equations, which may be the reason for a more accurate V_1 estimate and is discussed in more detail in Appendix B. To estimate the unsaturated layer depth and velocity,

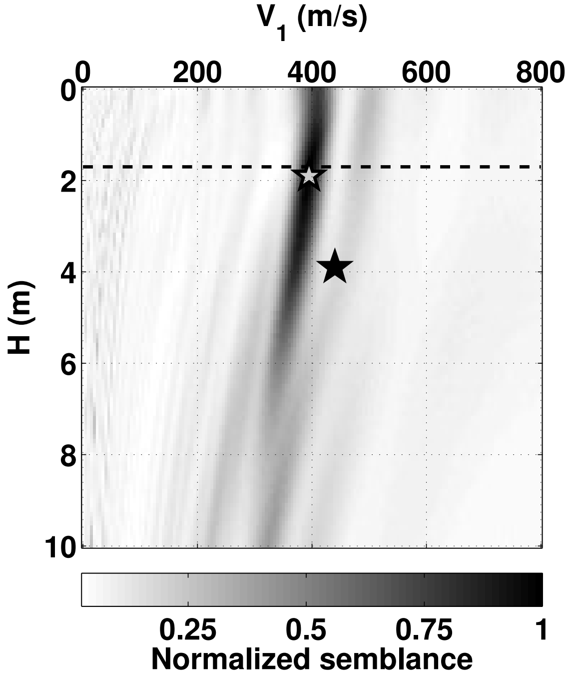

Figure 4.9: Sum of 30 semblance panels over the range of $|\mathbf{x}_{29} - \mathbf{x}_1|$= 28 m to $|\mathbf{x}_{59} - \mathbf{x}_1|$=58 m. The white star denotes the maximum semblance, which occurs at 1.9 m and 395 m/s. The black start denotes the estimate from Chapter 3 and the dashed line indicates the water table depth from Johnson (2011).

in Chapter 3 we picked the critical offset in the cross-correlation gather and the critical time in the real shot record. We estimated the critical offset X_c at 1.3 m in this area of the BHRS. This required a dense source spacing in order to sample the stationary-phase point in the correlation gather and dense receiver spacing (0.25 m) to identify the reflection. Therefore, in Chapter 3, we used a 0.1 m source spacing for the 2 m closest to the receiver array and then changed to 1 m for sources past 2 m. Using the values from the maximum semblance, we estimate

$$X_c = \frac{2V_1H}{\sqrt{V_2^2 - V_1^2}} = 0.55\ m. \tag{4.8}$$

In either case, the critical offset is on the order of the 1-m spacing we used in the semblance method, but our method does not require that we finely sample so as not to miss X_c. There is also no need to manually pick the stationary-phase point, which avoids interpreter error, and considering Figure 4.8(b), we feel it is difficult to identify the reflected wave and thus, the critical time needed in the method presented in Chapter 3.

Not only can we improve S/N of the virtual refraction, we are also able to increase the semblance S/N by stacking multiple panels. The laterally homogeneous numerical data example shows that stacking multiple semblance panels improves estimates of V_1 and H. In the case of lateral heterogeneity, stacking semblance panels is valid as long as lateral heterogeneity is on the order of the distance between the receivers used in the correlation gathers. Overall, the semblance approach has advantages to current refraction characterization methods. For example, there is no first break picking, only an estimate of the virtual refraction velocity at τ=0 s in the τ-p domain at each virtual shot location, and a semblance maximum for H and V_1. However, when lateral heterogeneity is strong, new refraction interferometry methods may be required.

To that end, there has recently been a development in first break tomography that utilizes the improved S/N of the virtual refraction. Mallinson *et al.* (2011) and Bharadwaj *et al.* (2011) have developed the super-virtual refraction method. It is based on the original receiver-receiver cross-correlation seismic interferometry, combined with an emerging technique called source-receiver interferometry that uses convolution rather than cross-correlation. The basic premise of the super-virtual refraction method is to create a virtual shot record containing the virtual refraction buy summing cross-correlations over a source array. Then convolve the virtual shot record with the original data, summing convolutions over a receiver array. This effectively redatums the high-amplitude virtual refraction back to the real refraction time. This method has the potential to increase long offset refraction amplitudes and has been demonstrated in field data (Hanafy *et al.*, 2011). This method requires a much more stringent geometry of overlapping sources and receivers, which differs from the more common off-end refraction survey geometry.

Finally, we do not explicitly show how the semblance method extends to multiple layers, but King *et al.* (2011) present a boot-strapping method whereby they estimate the interval velocity and thickness of multiple horizontal layers using a semblance method with a T_{diff} related to primary and multiple reflections. King and Curtis (2011) also use refraction artifacts in a marine setting to estimate the interval velocity of multiple layers by looking at repeating brightspots in a $\tau - p$ transformed virtual shot record. Our analysis is also not restricted to horizontal layers. Poliannikov and Willis (2011) showed a correlation gather semblance method for dipping layers using reflections from those layers; we could parametrize T_{diff} to incorporate a dip parameter, which would require a three-parameter semblance.

4.5 Conclusions

Virtual refractions in field applications of seismic interferometry are often present because acquisition requirements for exact recovery of the Green's function between receivers are not met. For a horizontal two-layer model, we estimate the velocity of the faster layer from the slope of the virtual refraction. Using a semblance analysis, we find the velocity and depth of the slower layer. Stacking multiple semblance panels at a single virtual shot location increases the signal-to-noise ratio and gives an improved estimate of these parameters. This approach offers a robust alternative to classical refraction methods and does not require the variable source and receiver spacing needed in Chapter 3.

CHAPTER 5:

STATICS ESTIMATION WITH THE VIRTUAL REFRACTION

Summary

In this chapter, we apply the virtual refraction analysis to 2D synthetic land seismic exploration data with statics caused by near-surface weathering layer thickness variations. Using the *delay-time method* (DT method), we estimate source and receiver statics using first-break arrival times. We go on to develop a *modified delay-time method* (MDT method), wherein we use the first-break arrival times of the virtual refraction to isolate and estimate receiver statics. We show that this approach simplifies the inverse problem by removing the source static term from the delay-time equation. Finally, we show that using the virtual refraction can extend lateral resolution and is better suited for estimating statics when the data are noisy.

5.1 Introduction

Velocity and thickness heterogeneity in near-surface layers is known to cause travel-time perturbations in the recorded seismic wavefield. These distortions can affect normal moveout velocity analysis (e.g., p. 183 in Yilmaz, 2001), and if left uncorrected, cause loss of lateral coherency. The end result is a poor seismic image. Travel-time perturbations of this type are often referred to as statics. An important first step in the reflection seismic imaging process is to remove these statics (e.g., p. 225 in Yilmaz, 2001).

The first step in statics removal is often elevation statics estimation and correction. If we assume the layers beneath the weathering layer are horizontal and the weathering layer velocity is known, we can estimate a time shift at each receiver relative to a reference receiver (e.g., the lowest elevation receiver) that will remove the effect of any elevation differences in the weathering layer. In areas where the weathering layer velocity is not known, methods based on first-break analysis have been developed to estimate source and receiver statics. One such method is the DT method (e.g., p. 120 in Burger *et al.*, 2006), which uses refraction arrival times. Yilmaz (2001) provides a background on the various *refraction statics methods* in Chapter 3.6.

In Chapters 2, 3, and 4, we analyzed the virtual refraction and the cross-correlation gather. We know that the virtual refraction exists in seismic interferometry if refractions exist in the input data. We also know that the virtual refraction is the first arrival in the virtual shot record and that the stationary-phase point in the cross-correlation gather defines the critical offset X_c. Therefore, in the following sections, we apply our analysis to a 2D synthetic land-seismic survey that contains source and receiver statics. We develop a modified delay-time statics estimation technique that uses the virtual refraction arrival times as input data. We use this new technique to estimate the refractor velocity (V_2) and isolate receiver statics before estimation.

5.2 Delay-Time Method

A simple statics model is shown in Figure 5.1. In the DT method, a refraction arrival time is represented by

$$T_{S_iX_j} \quad = \quad dT_{S_i} + dT_{X_j} + \frac{|S_i - X_j|}{V_2}, \tag{5.1}$$

where $|S_i - X_j|$ is the distance between a source (S_i) and a receiver (X_j), V_2 is the refractor velocity, and dT_{S_i} and dT_{X_j} are delays associated with the area around each source and receiver, respectively. In this framework, dT_{S_i} and dT_{X_j} can be thought of as the vertical travel time from the source to the refractor and from the refractor to the receiver, respectively (see Figure 5.1). Both are functions of the local weathering layer thickness and velocity. For multiple source (and/or receiver) positions as in Figure 5.1, first-break arrival times can be inverted to estimate the receiver (and/or source) statics and refractor velocity. This is done by finding dT_{S_i}, dT_{X_j}, and V_2 such that the misfit between modeled first breaks and real first breaks is minimized.

We test the DT method with an elastic wave 2D numerical experiment. The synthetic model is shown in Figure 5.2. Under the left half of the receiver array (receiver position 500 to 1000 m), the surface layer thickness is constant at 100 m. Under the right half (receiver positions 1000 to 1500 m), the surface layer thickness varies as a sine wave, leading to a layer thickness that varies between 90 to 110 m. The surface layer compressional and shear wave velocities are $V_{1,P}$=1500 m/s and $V_{1,S}$=600 m/s,

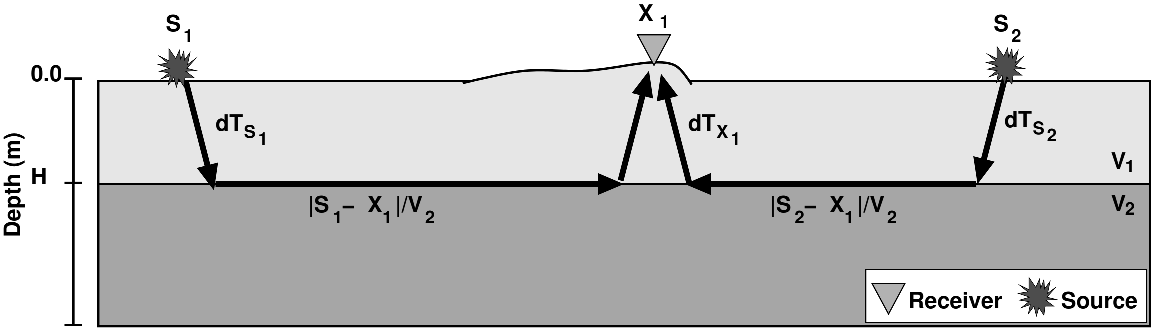

Figure 5.1: A laterally varying weathering layer model with two sources (S_1 and S_2 and receiver (X_1). Travel times are indicated along each ray path. For the travel path up from the interface receiver X_1, the path is assumed the same from each side.

respectively. The refractor velocities are $V_{2,P}$=2800 m/s and $V_{2,S}$=1000 m/s. The densities in each layer are ρ_1=1000 kg/m^3 and ρ_2=1500 kg/m^3. These parameters are constant in each layer.

We model the seismic wavefield for 0.5 s for a vertical point force at the surface using the Spectral Element Method (Komatitsch and Vilotte, 1998; Komatitsch and Tromp, 2002). The source is a 40 Hz Ricker wavelet and the blue stars represent sources placed on each end of the receiver array (green triangles). We show the wavefield recorded from sources at S_1 (500 m) and S_2 (1500 m) in Figure 5.3(a and b), respectively. Strong reflections (hyperbolic events) and a Rayleigh wave with linear moveout are visible. Weaker direct and refracted waves are also present. The effect of the surface layer thickness variation on the reflections is apparent in Figure 5.3(b), where we see the reflection oscillate as function of receiver position.

Overlain in red on the shot records are the first-break picks. We use the modified-energy ratio (MER) method (Han *et al.*, 2008) to pick first breaks. The MER method has been shown to more accurately pick noisy first breaks than other methods (e.g., short-term long-term ratios (STA/LTA) in Han *et al.*, 2010). We plot all of the first-

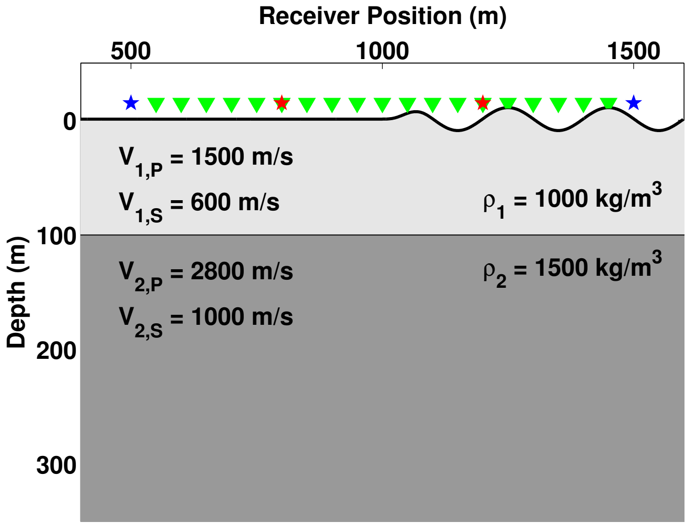

Figure 5.2: Synthetic model with varying surface layer thickness. Blue stars are real sources and red stars are virtual sources. Green triangles represent receivers located at the surface. V_1 and V_2 are the constant compressional wave velocities in each layer.

break picks in Figure 5.4(a) as a function of receiver position. Viewing the data in this way offers insights into the accuracy and resolution of the DT method inversion. The solid blue curves show the first-break picks from the two sources on each end of the receiver array. The black dashed lines indicate the crossover distance (X_d) from each of the sources. The crossover distance is the distance at which the first arrival goes from being the direct wave to being the refraction – or head wave – as is apparent by the change in slope at these points in Figure 5.4(a). Before the inversion for statics, we must remove all of the first-break picks associated with the direct waves (i.e., everything before the crossover distance).

To solve for V_2 and each source and receiver static dT_{S_i} and dT_{X_j}, we create a matrix equation relating unknown statics and velocity model parameters to the first-

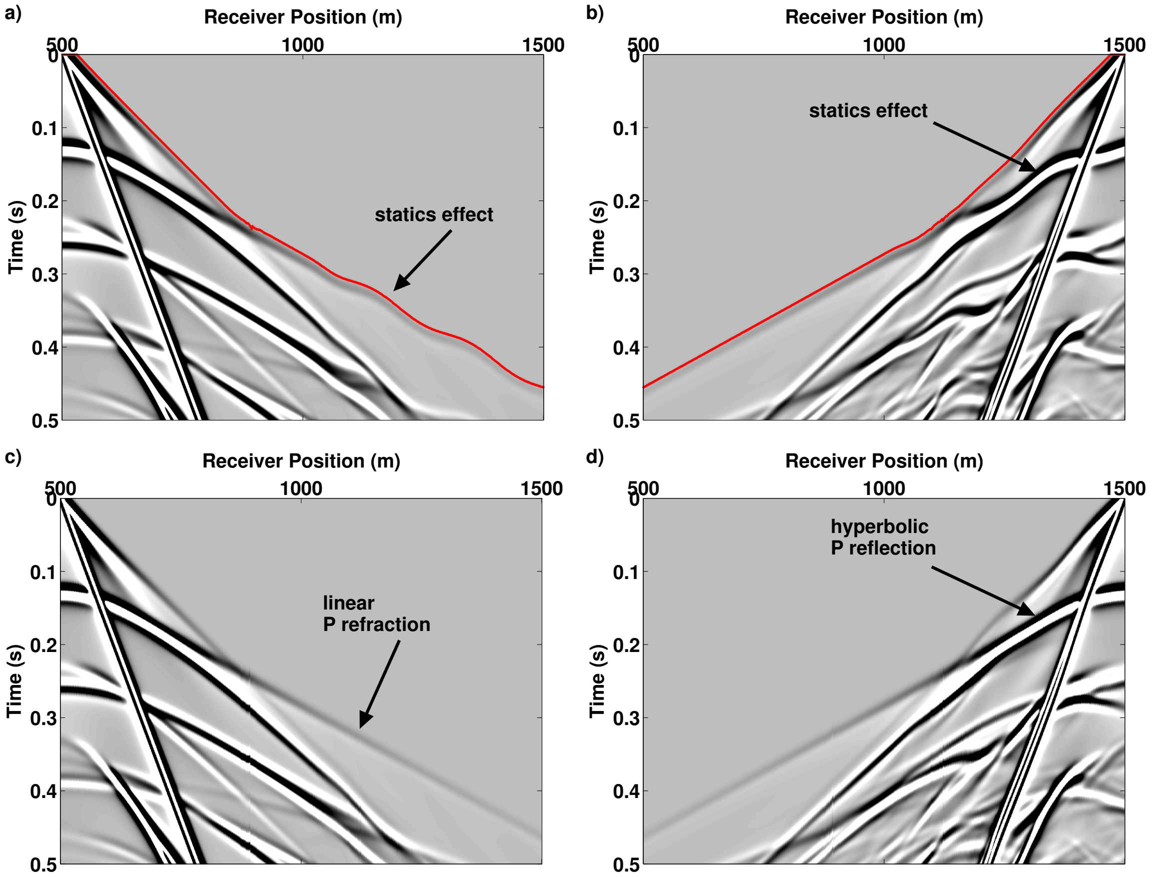

Figure 5.3: Shot records for S_1=500 m (a) and S_2=1500 m (b). The first-break picks are overlain in red. Receiver statics corrected shot records for S_1=500 m (c) and S_2=1500 m (d) using the DT method.

break picks following Equation 5.1. For source ($i = 1$), we relate the data

$$d = [T_{S_1X_1}, T_{S_1X_2}, ...T_{S_1X_j}]^T,$$

where $[]^T$ represents the vector transpose and $j = 1, \ldots, k$ is the number of receivers, to the model parameters

$$m = [dT_{s_1}, dT_{X_1}, dT_{X_2}, ..., dT_{X_k}, 1/V_2]^T$$

as $d = Am$. In this case, A is the linear operator

$$A = \begin{pmatrix} 1 & & |S_1 - X_1| \\ \vdots & (I_{kxk}) & \vdots \\ 1 & & |S_1 - X_k| \end{pmatrix}. \tag{5.2}$$

A is a horizontal concatenation of two vectors and an identity matrix. The first column of A is related to the source static and the last column is related to the $|S_i - X_j|/V_2$ term in Equation 5.1. The middle columns make up a $k \times k$ diagonal identity matrix (I). We use a truncated singular value decomposition (e.g., p. 55 in Aster *et al.*, 2005) to estimate an inverse matrix $A^\dagger$, such that we can relate the model parameters and data as $m = A^\dagger d$. We use the default MATLAB tolerance for the truncated SVD. In this case, the tolerance is computed as $(max(size(A)) * \|A\| * \epsilon)$, where $\epsilon =$ 2.22e-16 and $\|A\|$ is the norm of the matrix A. To extend the results for n sources, we vertically concatenate more data and model parameters. As a result, A is augmented on the left with columns of zeros related to each source position, so that the size of A is $(n \times k) \times (n + k + 1)$.

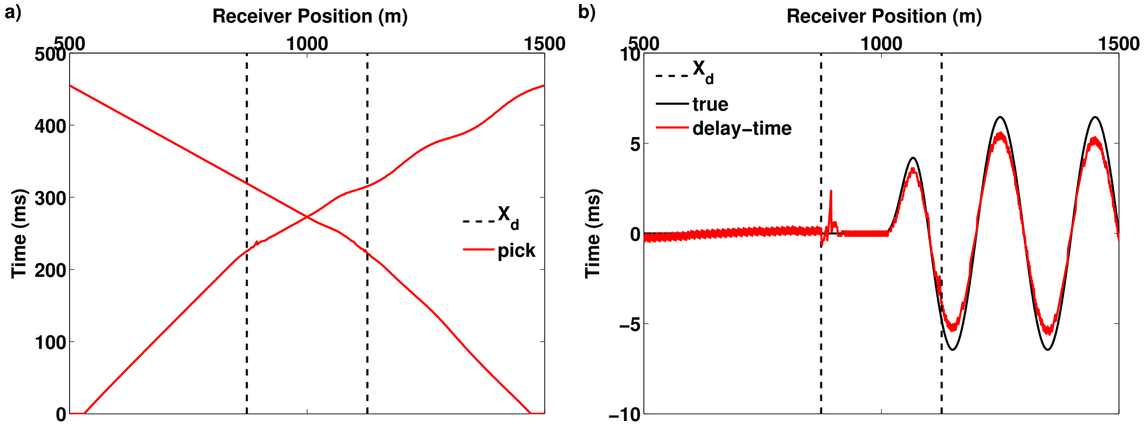

Figure 5.4: (a) Combined arrival-time plot for first-break picks. (b) Receiver statics estimate from the DT method (red) compared to the true receiver statics (black). Dashed black lines indicate the crossover distance (X_d) from each source.

Following this approach, we compute $A^{\dagger}d$ and find the source statics to be $dT_{S_1} = dT_{S_2}$ =90 ms and the refractor velocity to be V_2=2740 m/s. The receiver statics estimate are the red line in Figure 5.4(b). We also compute the true receiver statics relative to the 0 m surface elevation (black line). Estimates of the receiver statics are accurate, as long as we have good first-break picks (i.e., away from X_d where the MER picker accurately picks the refracted wave). To demonstrate the influence of the statics on raw shot records, we apply a receiver statics correction across the entire receiver array to the two shot records in Figure 5.3(a and b). The corrected shot records are shown in Figure 5.3(c and d). In Figure 5.3(c) the P-wave refraction is now linear and in Figure 5.3(d) the P-wave reflection is now hyperbolic. The later arriving converted and shear-wave reflections and refractions are not corrected because the estimated receiver statics are only for the P wavefield.

5.3 The Modified Delay-Time Method in the Presence of Noisy Data

Consider two receivers at X_A and X_B and a single source at S (Figure 5.5). Crosscorrelating the first arrivals at each receiver eliminates common terms in the two arrival-time equations. These terms are the raypaths from the source to the interface, along the interface (up to the dashed-blue line), and the path from the interface to receiver X_B. The paths that are not in common are the path along the interface dr (past the dashed-blue line), and the extra distance the refraction travels to X_A. For a horizontal refractor and any source i that generates a refraction at both receivers, the crosscorrelated arrival time equation is

$$T_{S_iX_A} - T_{S_iX_B} \quad = \quad dT_{AB} + \frac{|X_B - X_A|}{V_2}. \tag{5.3}$$

This crosscorrelation represents the virtual refraction ($|X_B - X_A|/V_2$), plus the travel time perturbation (dT_{AB}) between the two receivers. This is the combination of the red raypaths in Figure 5.5. The perturbation dT_{AB} is the receiver static at X_A relative to the reference receiver X_B. Similar to the DT method, we can invert a system of equations to estimate dT_{AB} using the virtual refraction first-break picks.

To emphasize the robustness of using the virtual refraction compared to the real refraction, we first add enough zero-mean random Gaussian noise to the real data so that the MER automated picker starts to fail at far offsets. The noisy shot records are shown in Figure 5.6(a and b). The first-break picks are the red asterisks, and it is obvious that the MER picker fails at the far offsets at this noise level. From the previous example, we know that incorrect first-break picks map directly into the

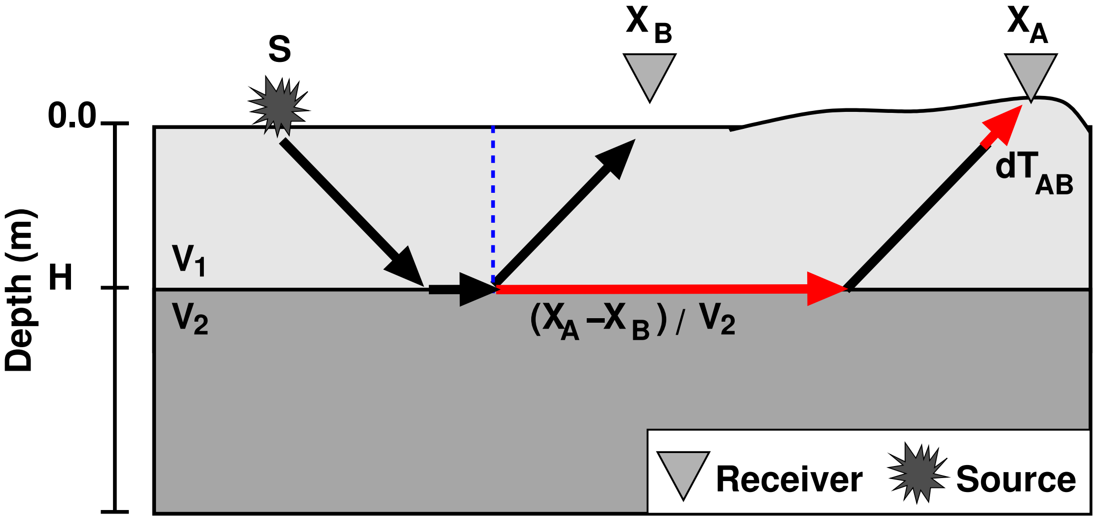

Figure 5.5: Subsurface model with a receiver static under X_A. To the left of the blue line, the model does not impact the virtual refraction arrival time.

receiver statics estimate in the DT method. Using the virtual refraction we now show that noisy data is less problematic if we use the MDT method.

We apply two preprocessing steps to the noisy data before crosscorrelation. First, we suppress the high amplitude surface wave with a $f-k$ filter; then we suppress other arrivals by muting the entire wavefield 25 ms after the direct and refracted arrivals. These steps eliminate cross terms from correlations of events other than the direct or refracted waves. We create virtual shot records by crosscorrelating the wavefields at the red star receivers (Figure 5.2) with all other receivers in the array. To improve the SNR of each virtual shot record, we sum crosscorrelations over 10 sources, evenly spaced from 500 to 545 m in the model. All sources are past the critical offset from both receivers; therefore, the virtual refraction SNR is enhanced (Figure 5.7(a)). We apply the same process for the virtual shot record in Figure 5.7(b) where we use 10 sources evenly spaced from 1455 to 1500 m. The virtual refraction first-break picks are the red asterisks in Figure 5.7(a and b) and we can see that MER picker does

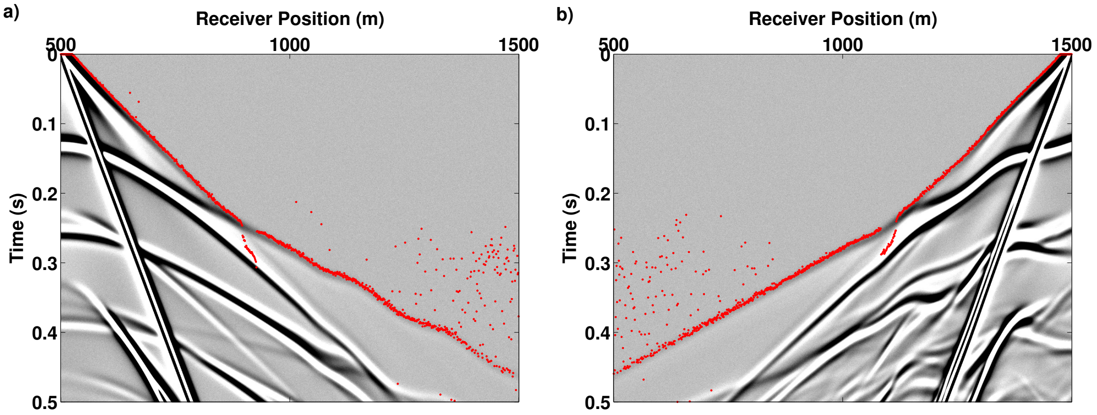

Figure 5.6: Shot records and first-break picks at S=500 and 1500 m after adding zero-mean random Gaussian noise.

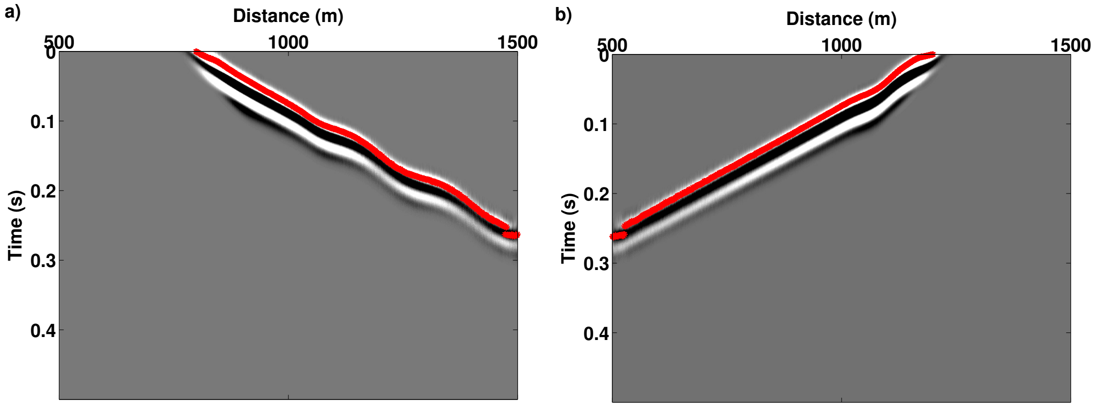

Figure 5.7: Virtual shot records for virtual sources at the red stars in Figure 5.2 (i.e., distance = 800 m (a) and 1200 m (b)).

well to pick the correct first-break. This is entirely due to the $\sqrt{N}$ improvement in the SNR in the virtual shot record, where N is the number of sources going into the summation.

We apply the same inversion procedure for the modified arrival-time equations; taking the virtual refraction first-break picks as input data. For a virtual source X_B, we relate the data

$$d = [T_{X_BX_1}, T_{X_BX_2}, ...T_{X_BX_k}]^T,$$

to the model parameters

$$m = [dT_{X_1}, dT_{X_2}, ..., dT_{X_k}, 1/V_2]^T$$

as $d = Am$. In this case, A is the linear operator

$$A = \left(\begin{array}{cc} & |X_B - X_1| \\ (I_{kxk}) & \vdots \\ & |X_B - X_k| \end{array} \right), \tag{5.4}$$

where now the offset term in the right column of A is the distance between the receiver and the virtual source. To incorporate more virtual source locations, we need only to vertically concatenate this system of equations for each virtual source.

The receiver static is now estimated relative to the virtual source position (i.e., the elevation at receiver position = 800 or 1200 m), which are at the same elevation in this example. We plot the receiver statics estimated with the MDT method in Figure 5.8(b) (red line). These receiver statics contain similar structure to the true model, and the refractor velocity estimate is V_2=2681 m/s. For comparison, we take the noisy picks from the real shot record (blue lines in Figure 5.8(a)) and apply the DT method. For these data, we estimate V_2=3562 m/s and dT_{S_1}=137 ms and dT_{S_2}=139 ms. The estimated receiver statics are plotted in blue in Figure 5.8(b). In both cases, the first-break data and receiver statics in Figure 5.8 have been smoothed using a three-point convolutional smoothing operation. Without this step, the blue lines are too noisy to compare with the red lines.

The two static estimates look similar only near the center of the model. This is

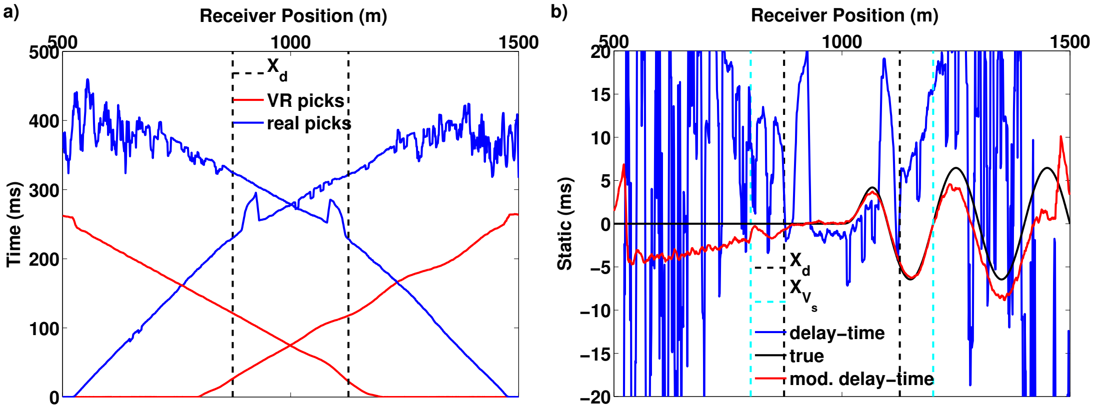

Figure 5.8: (a) Combined first-break arrival-time plot for the virtual shot record. (b) The MDT method receiver statics (red). The true static relative to zero elevation is the black line. The blue line shows the static estimated using the noisy data and DT method. The MDT method provides a superior result.

because the first-break picks for both real and virtual refractions are accurate within this region. However, the virtual refraction picks are accurate out to far offsets so the receiver statics estimated with the MDT method follow the structure with the correct magnitude over the entire model. The DT method does not. This is not due to the difference in inversion, rather this is due the inherent stacking over sources in the seismic interferometry method. Thus, higher SNR in the virtual shot records allows the MER method to more accurately pick virtual refraction first breaks than real refraction first breaks.

5.4 Lateral Resolution and Model Accuracy

We investigate the differences in lateral resolution between the two methods by looking at a diagram of the different moveouts associated with each wave type. Figure 5.9(a) shows the traveltime moveouts of the direct (solid black), reflected (solid

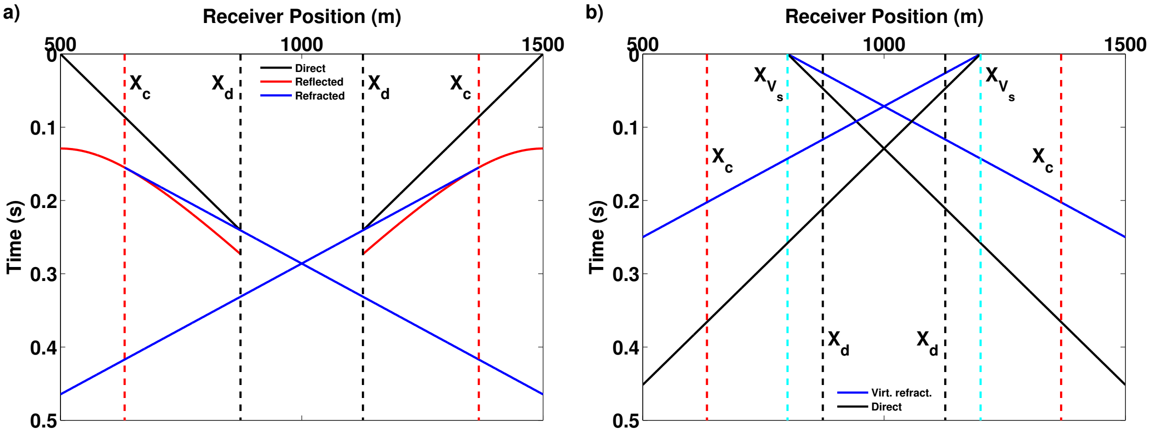

Figure 5.9: (a) Moveout of three wave types for sources at the edges of the receiver array. (b) Moveout of the virtual refraction and direct wave for virtual shots at 800 m and 1200 m. X_c and X_d are the critical offset and crossover distance, respectively. X_{V_s} is the virtual shot position.

red) and refracted waves (solid blue). The crossover distance (X_d) and the critical offset (X_c) are shown as well, dashed black and dashed cyan lines, respectively. In the DT method, we use first-break picks from the real refraction. This refers to first-break picks at distances past X_d from either of the sources. Therefore, within the bounds of the two dashed-black lines, we have data in both directions and the error is reduced compared to the error outside the black dashed lines. We can visualize this by looking the model covariance matrix estimated from the matrix A.

Following Aster *et al.* (2005), we compute the model parameter variance σ_m^2 in a least-squares sense as

$$\sigma_m^2 = \sigma_d^2 * diag((A^T A)^{-1}), \tag{5.5}$$

where A linearly relates the model parameters m and the data d as $d = Am$. In this way, we can look at the relative statics error (σ_m) for each receiver. For the real and virtual shot positions in the previous section, Figure 5.10 shows σ_m for the DT method (dashed blue) and the MDT method (solid red) assuming all first-break picks have a constant error σ_d= 1 ms. We could assign individual first-break errors, but in order to demonstrate the affect of data in both directions we keep the error constant.

In both methods the error in receiver statics is reduced within the section of the model where forward and reverse propagating refractions overlap. This is because we have two data points for one parameter. Outside of this region, we have one data point per model parameter, so data errors map directly to their corresponding model parameter. Considering Figure 5.9(b), we can see the reason behind the laterally extended error reduction in the MDT method. For any virtual shot location (X_{V_s}) between X_c and X_d the first arrival will be the virtual refraction. Therefore, the first-break pick will be the virtual refraction. This means that as long as we have the resolution in our wavelet to distinguish between reflection and refraction near X_c, we can reduce the error in the statics estimate between X_d and X_c by using the MDT method. We only need to know the distance X_c so we can correctly place the virtual shot; something that could be determined using the semblance method presented in Chapter 4. An increase in lateral resolution from using the virtual refraction has previously been investigated for time-lapse reservoir characterization by Tatanova *et al.* (2009).

5.5 Discussion

One advantage of the MDT method is its robustness in the presence of noise. In the case shown here, we use the improved SNR of the virtual refraction to get more accurate first-break picks which lead to more accurate statics estimation. This is a

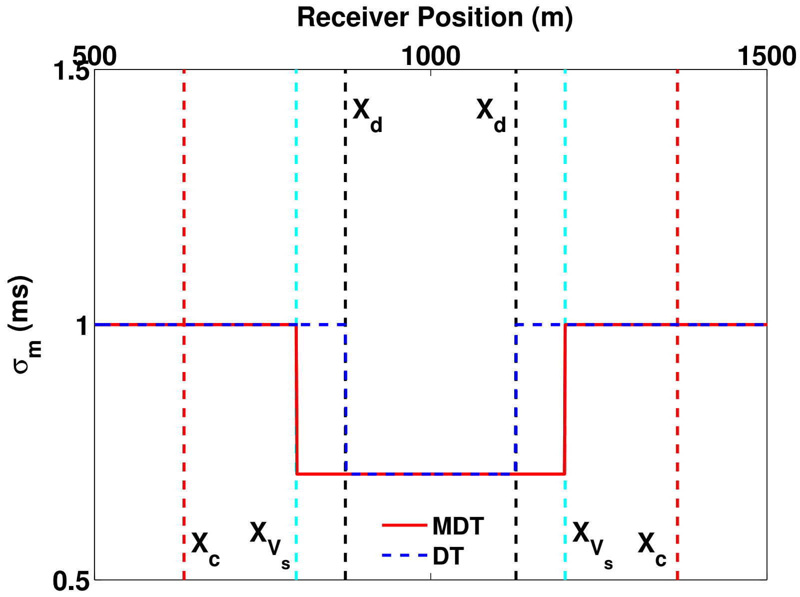

Figure 5.10: Comparison of the error estimate (σ_m) for each receiver. Black dashed lines indicate the crossover distances (X_d) and dashed cyan lines indicate the virtual shot positions. Error is reduced within the dashed lines because refractions exist in both forward and reverse directions.

useful tool for long offset surveys where refraction amplitudes can be on the same order as the background noise. A second advantage is the reduced error over a larger lateral extent than the original DT method. The diagonal of the model covariance matrix demonstrates this fact, and depending on the data quality, we can improve the lateral resolution with the MDT method.

We should keep in mind that rather than window our picks (i.e., suppressing direct wave first breaks) as in the DT method, the MDT method requires suppression of surface waves and reflections before crosscorrelation when building the virtual refraction. Not doing this step leads to other spurious arrivals in the virtual shot record. When using an automated first-break picker – as we did here – other spurious arrivals can lead to incorrect picks which effect the final receiver statics estimate.

The final thing to note is the absence of the source static in the MDT method. We have eliminated this model parameter from the inversion result; however, we can estimate source statics by rearranging the data into common receiver gathers (rather than common source gathers) and repeat the same steps outlined above. Curtis *et al.* (2009) demonstrate how to turn sources into virtual receivers using the reciprocity in the wave equation. Following this, a modified delay-time equation for source statics is

$$T_{S_A X_j} - T_{S_B X_j} = dT_{AB} + \frac{|S_B - S_A|}{V_2}, \tag{5.6}$$

where dT_{AB} is now a source static relative to source S_B. In this way, we implement a new method that isolates the two types of statics. This is useful because we now eliminate any trade-off the occurs between the source and receiver statics, as is the case in the DT method. Both methods estimate the refractor velocity with the same accuracy, which is largely affected by the quality of the picks and the geometry of the source and receiver arrays.

5.6 Conclusion

For horizontal layers, we estimate the refractor velocity and receiver statics using a modified delay-time method based on the virtual refraction. Using this approach we are able to isolate source and receiver statics and invert for each separately, thus removing any trade-off that existed within the delay-time method. Due to inherent stacking over sources in the seismic interferometry process, we are able to improve the first-break pick quality using the virtual refraction. We also show that using the virtual refraction can increase the lateral resolution compared to the delay-time method. Finally, windowing and ground-roll suppression are necessary so that the virtual refraction is the first arrival across the entire array. This newly developed method provides an alternative (and in some cases superior) approach to delay-time statics.

CHAPTER 6:

USING THE GREEN TENSOR TO ISOLATE WAVE MODES

Summary

In this chapter, we show the benefits of using the full Green tensor estimated with seismic interferometry. The fact that different waves modes have different particle motions and different incidence angles means that modes are recorded with different amplitudes on certain components in 3-component recordings. This lends itself to (possibly) isolate and/or suppress given modes of interest. We illustrate this idea using intuitive reciprocity and anti-symmetry arguments and demonstrate it with a simple laboratory experiment. In Section 6.3, we review a field-data example from van Wijk *et al.* (2011), where they use the ambient-seismic noise field to estimate and isolate Rayleigh waves when the noise-source distribution is not isotropic (i.e., not equipartitioned) and not inline with the receivers. This noise distribution causes artifacts in the standard vertical-vertical component cross-correlations not present in the cross-term component. We then consider refracted S waves in a numerical

experiment. We find that the cross-terms for body waves are sensitive to the incidence angle; however, we still find improved signal to noise in the cross-term estimate for body waves.

6.1 Introduction

Being able to estimate the impulse response between seismic stations from cross-correlating ambient noise has added a new dimension to surface-wave inversion for the Earth's lithosphere. Phase- and group-velocity dispersion curves between distributed station pairs are inverted for 3D velocity structure (e.g., Sabra *et al.*, 2005; Shapiro *et al.*, 2005; Lin *et al.*, 2008; Ekstrom *et al.*, 2009). Ideally, station pairs are surrounded by noise sources so that the elastic Green tensor can be found by summing cross-correlations of the different components (i, j) of the wavefield (Equation 87 of Wapenaar and Fokkema, 2006):

$$G_{ij}(\mathbf{x}, \mathbf{x}', t) + G_{ij}(\mathbf{x}, \mathbf{x}', -t) \propto \oint_S u_i^S(\mathbf{x}, t) \star u_j^S(\mathbf{x}', t) d\mathbf{S}, \tag{6.1}$$

where $G_{ij}(\mathbf{x}, \mathbf{x}', t)$ is the Green tensor with component i at location $\mathbf{x}$ from a source in direction j at $\mathbf{x}'$. $u_i^S(\mathbf{x}, t) \star u_j^S(\mathbf{x}', t)$ denotes cross-correlation of the components of the measured wavefield at $\mathbf{x}$ and $\mathbf{x}'$ from a source on contour S. In ambient noise surface wave tomography (Shapiro *et al.*, 2005), spatial integration is replaced with summation over k time sections of the wavefield u, aiming to capture surface-wave signal from ocean-generated noise around the stations at $(\mathbf{x}, \mathbf{x}')$:

$$G_{ij}^R(\mathbf{x}, \mathbf{x}', t) + G_{ij}^R(\mathbf{x}, \mathbf{x}', -t) \approx \sum_k \left(u_i(\mathbf{x}', t) \star u_j(\mathbf{x}, t) \right)_k . \tag{6.2}$$

In this case, G^R_{ij} represents the Rayleigh wave component of the Green function.

An uneven source distribution and contamination by wave modes other than Rayleigh waves can lead to artifacts in the estimated Green functions from cross-correlation. Wapenaar *et al.* (2011) show in a numerical example how multi-dimensional deconvolution can suppress unwanted signal. While currently the vertical component ($i = j = z$) of the Rayleigh wave is most commonly used in ambient noise tomography, we expand upon the work of van Wijk *et al.* (2010, 2011) and propose to estimate the cross-terms of the Green tensor. This approach possibly allows us to isolate and/or remove certain wave modes from interferometric wavefields. The following demonstrates how this approach can isolate Rayleigh waves.

A vertically heterogeneous earth has an anti-symmetry between the horizontal component of the Rayleigh wave from a vertical force source, and the vertical component of the Rayleigh wave from a horizontal force source (Equation 7.147 in Aki and Richards, 2002):

$$G^R_{rz}(\mathbf{x}, \mathbf{x}', t) = -G^R_{rz}(\mathbf{x}', \mathbf{x}, t) = -G^R_{zr}(\mathbf{x}, \mathbf{x}', t), \tag{6.3}$$

where subscript r stands for radial and z for vertical. The first equality in this equation shows the anti-symmetry in the Green function caused by the elliptical polarization of the Rayleigh wave particle motion. The second equality is a result of reciprocity. Figure 6.1 demonstrates this idea of anti-symmetry and reciprocity in a graphical sense. It is important to note the direction of the radial component (toward or away from vertical component) between the three diagrams. Following Equation 6.2, we estimate the multi-component ambient noise Green functions and compare $G^R_{zz}(\mathbf{x}, \mathbf{x}', t)$ to $G^R_{zr}(\mathbf{x}, \mathbf{x}', t) - G^R_{rz}(\mathbf{x}, \mathbf{x}', t)$. The Hilbert transform (e.g., page

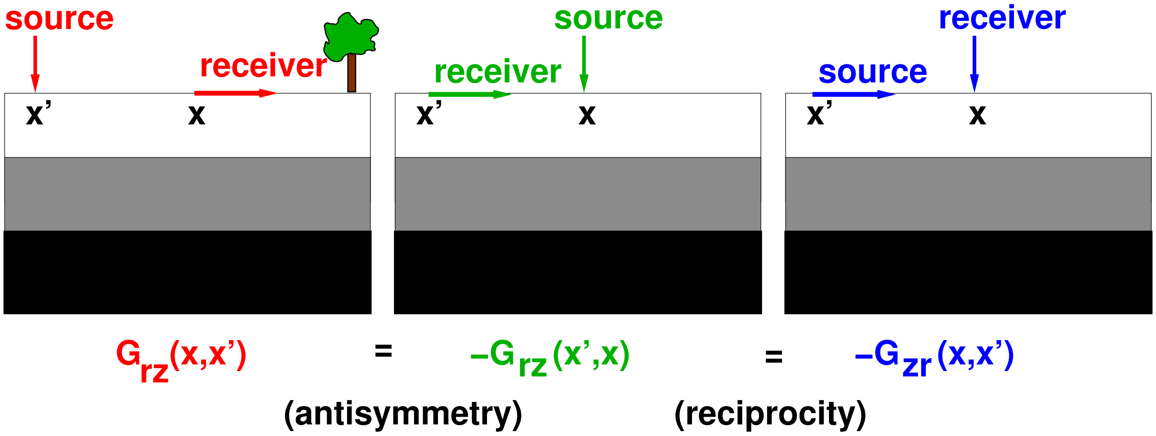

Figure 6.1: Graphical presentation of relationships in Equation 6.3. Arrows indicate the source and receiver polarizations.

20 of Claerbout, 1985) equalizes the phase between G_{zz} and the difference of the cross-terms:

$$G^R_c(\mathbf{x},\mathbf{x}',t) = \mathscr{H}\left[G^R_{zr}(\mathbf{x},\mathbf{x}',t) - G^R_{rz}(\mathbf{x},\mathbf{x}',t)\right]. \tag{6.4}$$

Cross-correlations of multi-component data from the Batholiths experiment (Calkins *et al.*, 2010) provide estimates of the cross-terms of the Green tensor. We will show that the G^R_c is more robust than G^R_{zz} in the presence of seismic signal not in-line with the seismic stations.

6.2 A Laboratory Experiment

To show a physical example of Equations 6.3 and 6.4, we designed the 2D laboratory experiment shown in Figure 6.2. The model is a homogeneous piece of aluminum. A high-powered pulsed Nd:YAG laser generates ultrasonic waves by briefly (15 ns) heating a 1-mm point on the surface. The heating causes thermoelastic expansion and generates broad-band ultrasonic waves (Scruby and Drain, 1990). In this case, the ultrasonic waves have a central frequency of 600 kHz, and the model approximates a homogeneous halfspace for Rayleigh waves (Blum *et al.*, 2010). The source is indicated by the dashed red line in Figure 6.2. The actual position of the source is not important in this example; we only require that the source be in the far field and inline with the two receiver locations (i.e., in the stationary-phase region for Rayleigh waves). We record the ultrasonic wavefield at two locations, x' and x, with a laser interferometer (Scruby and Drain, 1990). We use a 2-component laser receiver (Blum *et al.*, 2010) to record the vertical (i.e., out-of-plane) displacement field, as well as the radial (i.e., in-line or in-plane) component. The two recordings at each location are displayed in Figure 6.3.

To turn x' into a virtual source, we cross-correlate combinations of the vertical and radial components (Figure 6.4(a)) and the vertical-vertical recordings (Figure 6.4(b)). As expected from the intuitive explanation in Section 6.1, the combinations of radial and vertical components have a phase difference of π (i.e., anti-symmetric). Following from the previous section, we take the difference of the cross-terms (Figure 6.4(b)) and then the Hilbert transform (Figure 6.4(c)). The Hilbert transform of the difference in the cross-terms is compared to the more common, vertical-vertical cross-correlation. The phase matches and the amplitude of the cross-term is larger than the vertical-vertical cross-correlation. The amplitude difference is a function of the ellipticity of the Rayleigh wave, and in this model we can quantify the ellipticity by looking at the ratio of G_C to G_{ZZ}. Assuming attenuation and ellipticity in this homogeneous aluminum block are constant, then the amplitude relationship between the vertical and cross-term components is $G_{ZZ} = 2RG_C$, R is the ellipticity or ratio of the hori-

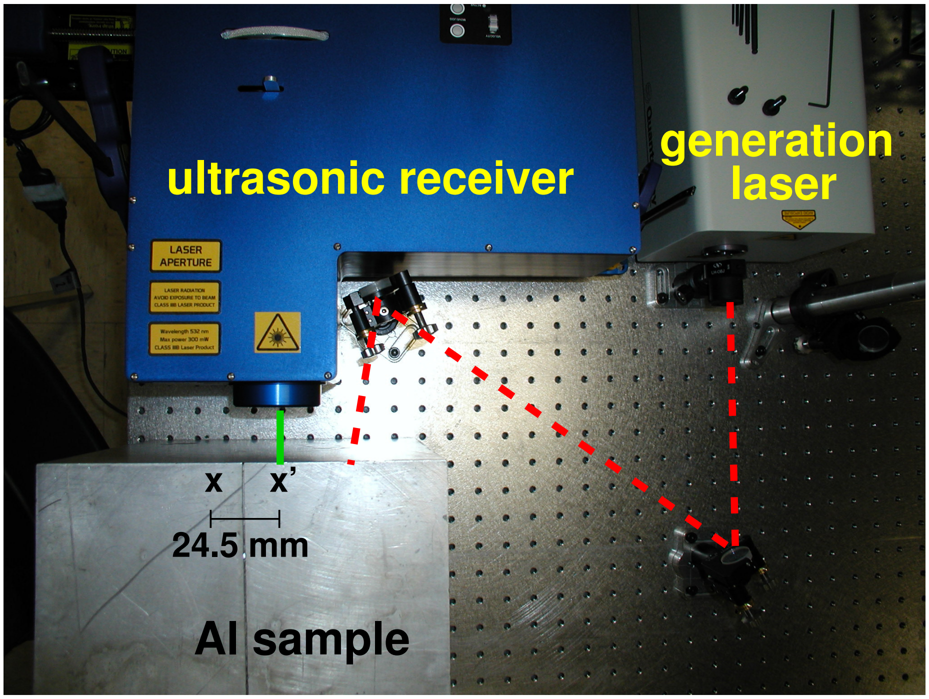

Figure 6.2: Laser ultrasonic laboratory experimental setup. A source laser generates an ultrasonic wavefield that is recorded at x' and x by a laser interferometer. The model is a homogeneous piece of aluminum. This model represents a homogeneous halfspace at these wavelengths.

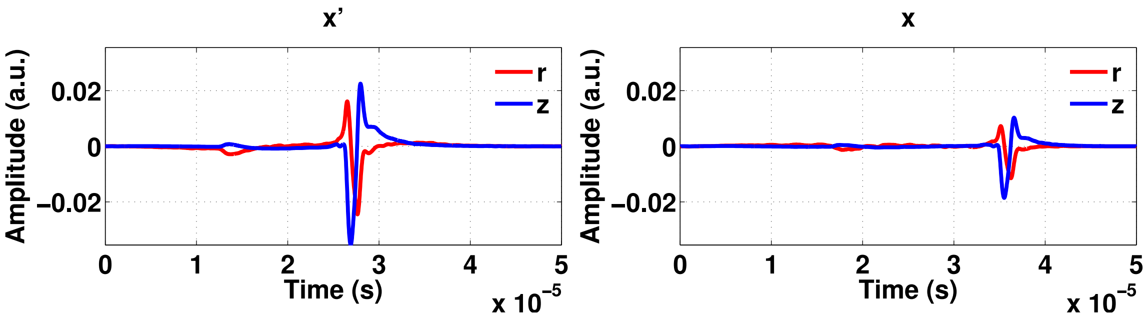

Figure 6.3: Displacement in the vertical (z) and radial (r) directions recorded by a laser interferometer at locations x' and x shown in Figure 6.2.

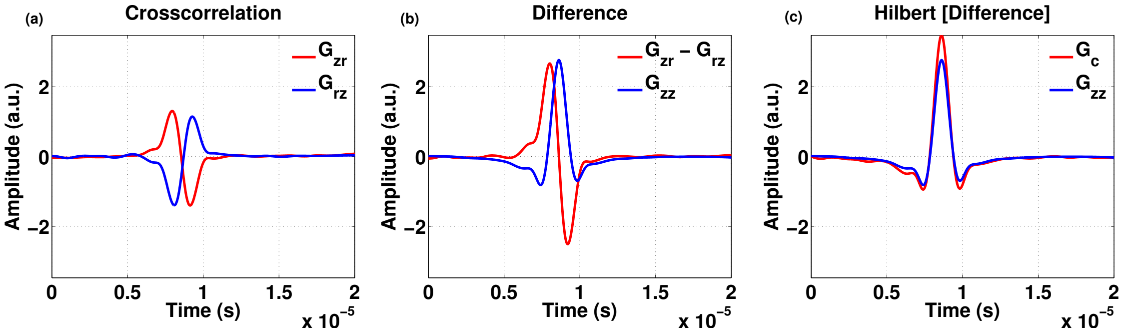

Figure 6.4: (a) Cross-correlation between vertical and radial components recorded at x' and x. (b) Comparison between cross-correlation of vertical-vertical with the difference between the signals in (a). (c) Hilbert transform of the difference in (a) compared to the vertical-vertical cross-correlation.

zontal to vertical particle motion for Rayleigh waves. From the data in Figure 6.4(c), we estimate R=0.63, which matches well with an independent estimate of R=0.64 in this same block by Blum *et al.* (2010). In the next section, we show a field data example, where the majority of sources lie out-of-line with the receiver array. We use the cross-term estimates to suppress artifacts and improve the S/N in the estimate Green function.

6.3 Rayleigh Wave Isolation with the Cross-Terms

Continuous measurements of the ambient-seismic noise field from the Batholiths experiment serve to illustrate the robustness in the Rayleigh wave Green function estimated with the cross-terms. During this experiment, 14 months of 3-component broadband seismic data were recorded along two perpendicular transects, with roughly $\sim$ 10 km interstation spacing along each transect (Calkins *et al.*, 2010). Sensors consisted of either a Guralp CMG3T or a Streckheisen STS-2 seismometer linked to a Quanterra 330 data acquisition system recording at 40 samples per second (Calkins *et al.*, 2010). The northern transect (Figure 6.5) traversed Douglass Channel from Hartley Bay to Kitimat and then followed the Skeena River northeast from Terrace to New Hazelton (Calkins *et al.*, 2010).

The azimuth from station BN01 to BN23 is 29 degrees from North in the clockwise direction (Figure 6.5). We rotate the horizontal components of the wavefield recordings to a generally radial (r; parallel to 29 deg from N) and transverse (t; perpendicular to 29 deg from N) component, band-pass filter (0.1 - 1 Hz), and sign-bit the data. We cross-correlate combinations of the vertical and radial components of the wavefield from station BN01 with those of all 20 active stations according to Equation 6.2. The Green tensor estimate is the sum of non-overlapping, ten-minute cross-correlations from August 1, 2006 00:00:00 (HH:MM:SS) to August 4, 2006 00:00:00. We correct the amplitudes for geometrical spreading.

We show the Green tensor elements related to the vertical and radial components in Figure 6.6. We observe strong similarity in the Rayleigh-wave arrivals in all com-

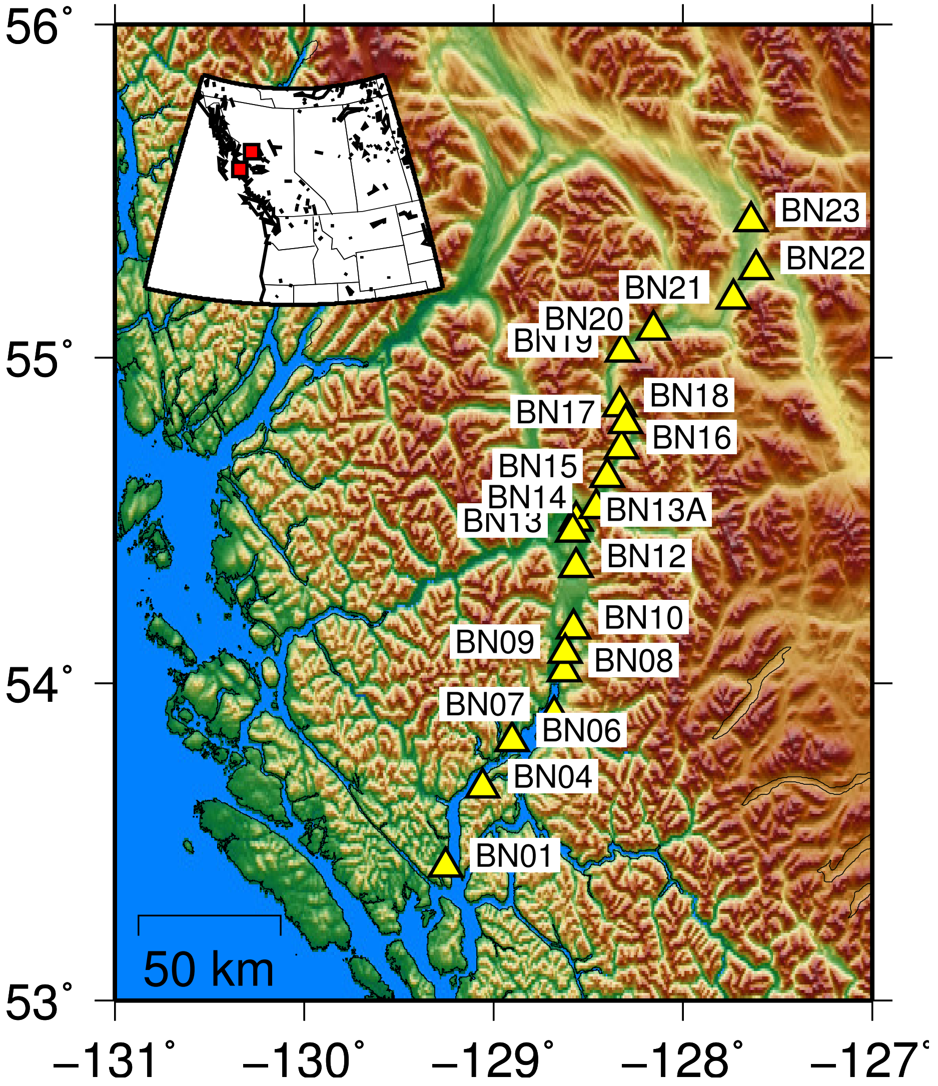

Figure 6.5: Location of the active stations in August of 2006 of the North line of the Batholiths experiment. Red squares on the regional inset are BN01 and BN23.

ponents. However, G_{zz} contains coherent signal around $t = 0$ s for all stations, not present in the cross-terms or G_c. This energy is the result of near-simultaneous arrivals (i.e., not in-line with the receivers) on the vertical component at the stations $\mathbf{x}$ and $\mathbf{x}'$. The lack of this coherent noise in G_c means that u_r is less sensitive to it, which suggests the noise source is either out-of-line surface-wave energy with the seismic stations, or body-wave energy.

To test for the presence of out-of-line surface- or body-wave energy inferred from the cross-correlation results in Figure 6.6, we conduct a frequency-wave number (f-k) analysis (e.g., Rost and Thomas, 2002) of the vertical component records. We added the Batholiths southern station line (Figure 6.7), which has a nearly E-W orientation, to increase resolution compared to beam forming with a linear array. L-shaped arrays, as used here, smear energy in the direction of the array legs (see examples in Rost and Thomas, 2002).

Our analysis is performed in the same frequency band as the cross-correlations (0.1 - 1 Hz), taking the average of the absolute amplitudes in the beam window to calculate each value in the slowness grid. We apply the f-k analysis to consecutive one-hour segments spanning the same time window used in the cross-correlations. All hourly slowness grids are stacked using the L1 norm and the result normalized to the maximum amplitude in the grid. The L-shaped array likely explains the elongated shapes of noise sources in Figure 6.7. Nevertheless, the southern (in-line) source is a true secondary source to the dominant western (out-of-line) source, since the peak amplitude areas have large separation in slowness space and their amplitudes vary independently with time when viewed in the individual one hour f-k grids. Both source directions have slownesses typical for Rayleigh waves, with the dominant en-

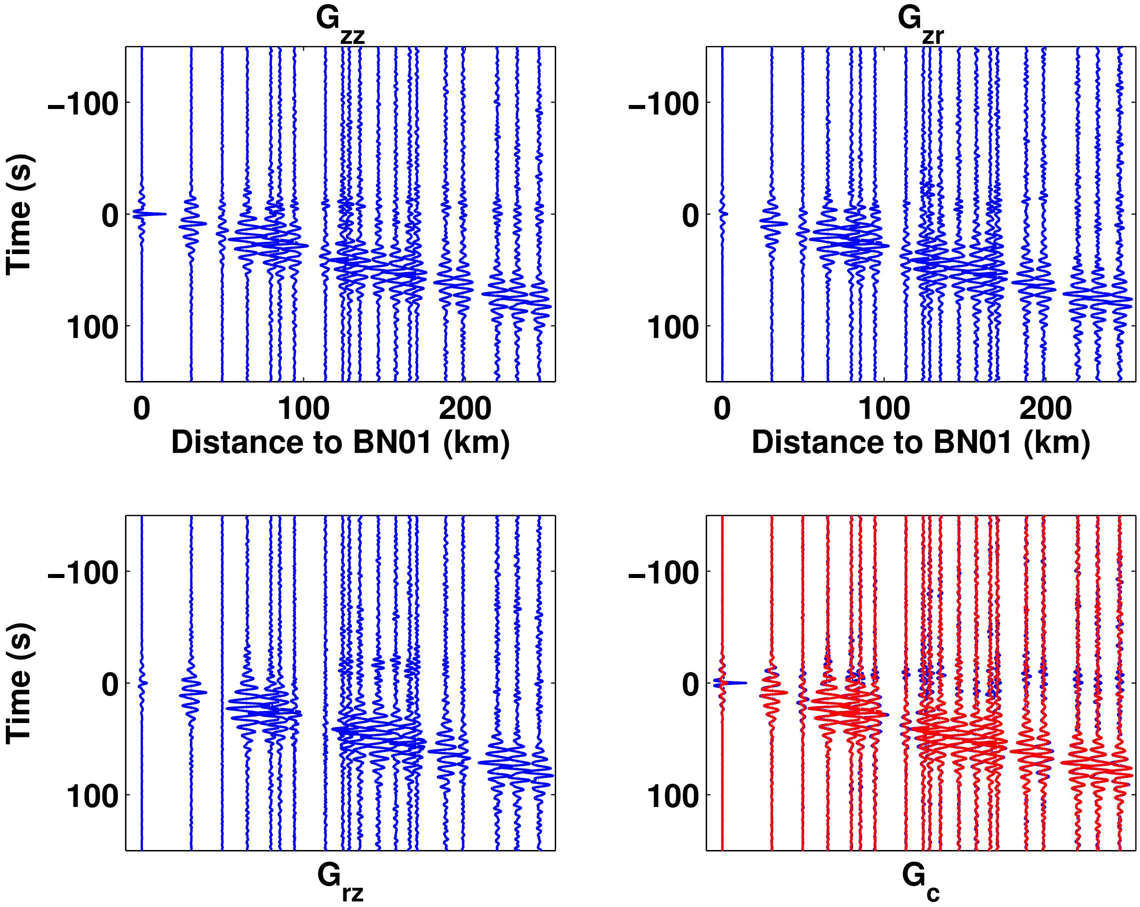

Figure 6.6: Estimated Green tensor from cross-correlation of three days of ambient noise. For the smaller station spacings in G_{zz}, an artifact at $t \approx 0$ s interferes with the Rayleigh wave. In the lower right plot, G_c is red and overlays G_{zz} (blue) in order to compare the presence or lack of coherent energy at $t \approx 0$ s.

ergy from the West propagating obliquely to the North station line used for the cross-correlations. This out-of-line source energy is responsible for the feature near $t = 0$ s in the vertical component cross-correlations. The f-k analysis confirms that the dominant noise direction is out-of-line. Fortunately, the cross-terms and G_c are less sensitive to this energy because it is not recorded on the radial component. Therefore, G_C will contain fewer artifacts due to an uneven source distribution. To understand the impact of these artifacts, we now look at individual station correlations.

For stations separated less than 175 km from BN01, the signal from out-of-line ocean noise interferes with the Rayleigh-wave arrival in G_{zz}. This can be observed in Figure 6.6, and is highlighted by showing three of the waveforms in Figure 6.8 (upper) and corresponding envelopes in Figure 6.8 (lower). In the left plots there is no clear time separation between the Rayleigh wave energy and the noise around $t \approx 0$ s. Only for large station separation – such as in the center and right panels – can a separation between Rayleigh-wave signal from noise be seen. This interference for the shorter station separations can lead to biased velocity and/or amplitude information in the estimate of the Rayleigh wave, which in turn can be erroneously attributed to attenuation and anisotropy (also discussed in Harmon *et al.*, 2010).

To quantify the improvement of using the cross-terms, we use the five largest station spacings, where the Rayleigh wave arrival is distinctly later than the early-time noise, and calculate the signal-to-noise ratio:

$$\mathrm{SNR}_{dB} = 10 \log \left(\frac{A_{signal}}{A_{noise}} \right)^2 , \qquad (6.5)$$

where A_{signal} and A_{noise} are the average amplitudes in the time window of the Rayleigh wave ($35 < t < 100$ s) and of the noise ($t < 35$ s), respectively. For G_c, $\mathrm{SNR}_{dB} =$

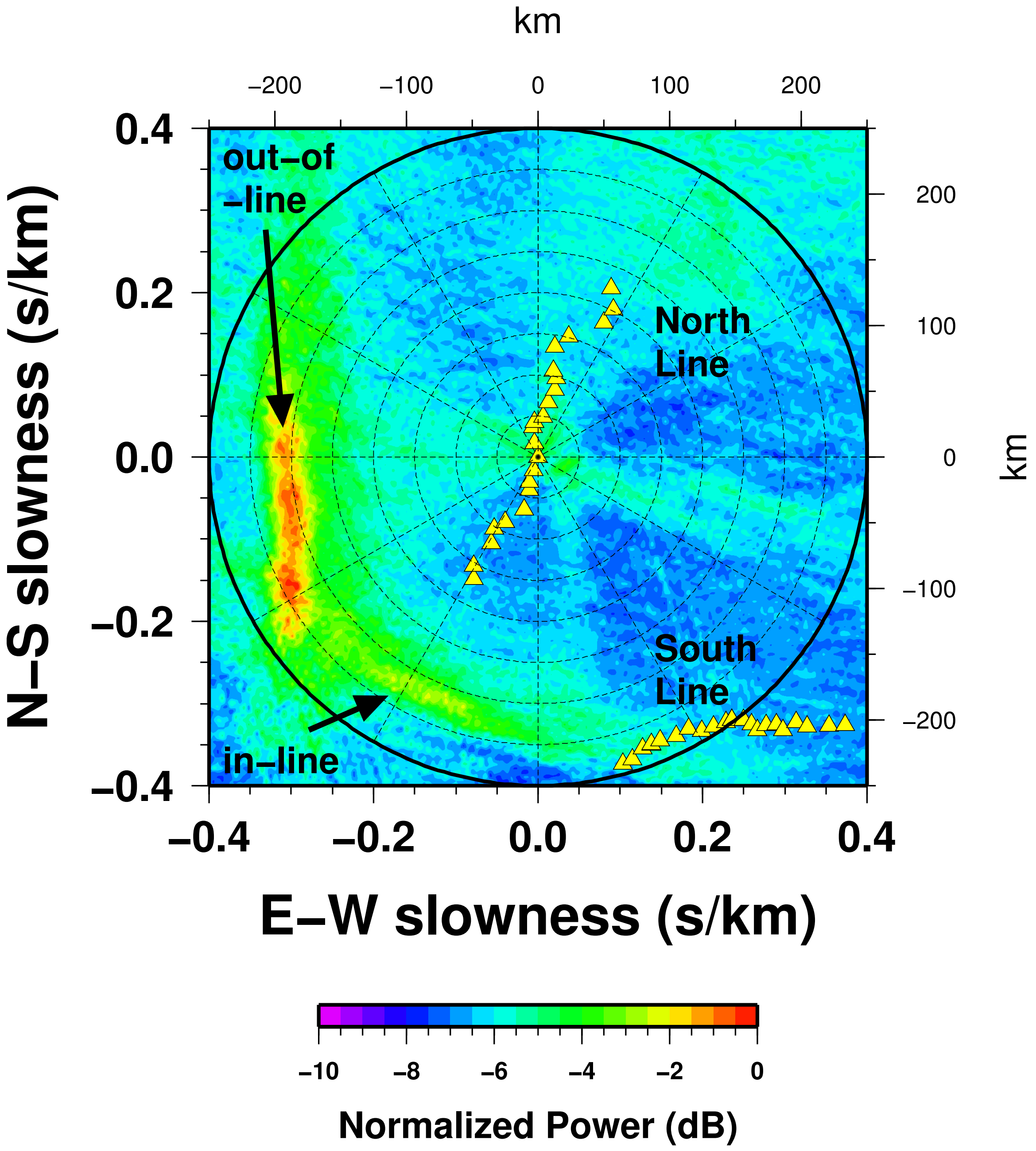

Figure 6.7: Summation of hourly f-k grids for the same three-day time window used in the cross-correlations. Yellow triangles show station locations (distance scale on top and right). Dominant energy is from the West, with a secondary source of energy in the Southwest.

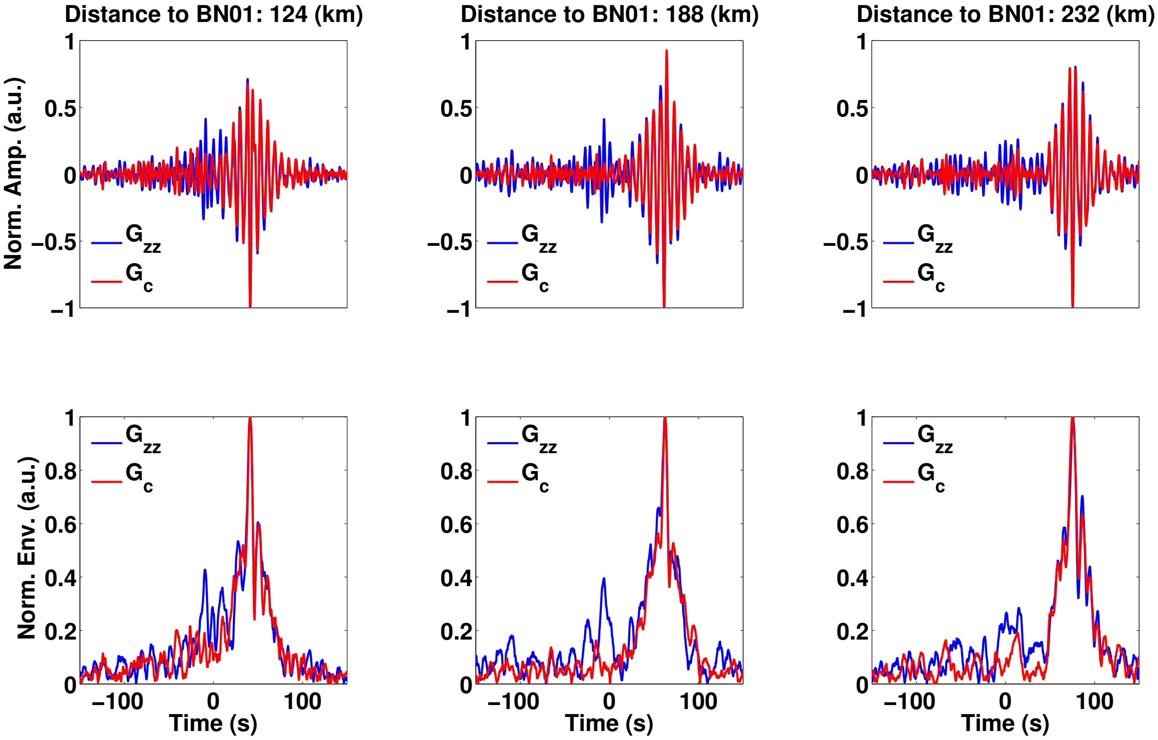

Figure 6.8: Top panel shows a comparison of the Green function estimates for three stations. Bottom panels shows the waveform envelopes for each Green function above. For the smaller two station spacings, noise at $t \approx 0$ s interferes with the Rayleigh-wave arrival in G_{zz} (blue), but this artifact is not present in G_c (red). For wave fields with a large station spacings, such as in the right panel, noise and signal are separated in time.

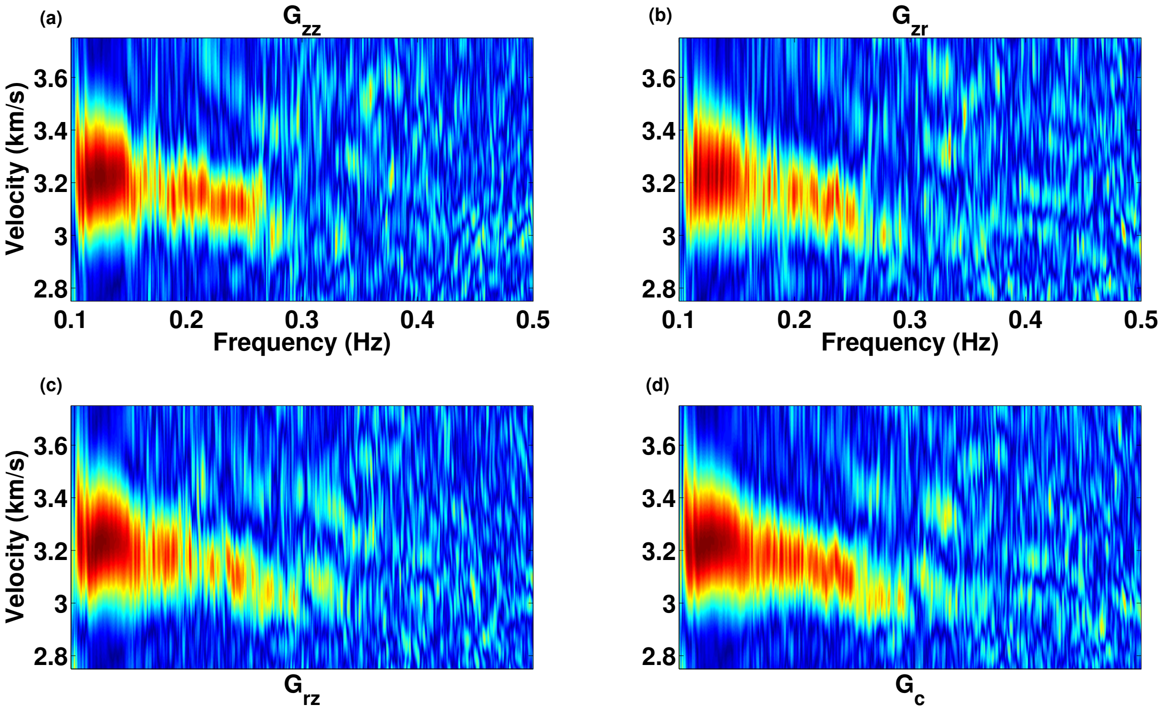

Figure 6.9: Phase velocity dispersion curves for the estimated cross-term components of the Rayleigh wave Green tensor. G_c shows significant improvement in coherency, particularly near 0.3 Hz.

14 dB, compared to a much lower 5 dB for G_{zz}.

To further illustrate the quality of G_c, we compute the phase-velocity dispersion curve – commonly used to invert for velocity structure – for each virtual shot record in Figure 6.6. We compute the phase-velocity dispersion curves using the Full-Offset Dispersion Imaging technique (Park, 2011), which includes spectral whitening in the phase-velocity transformation. A direct comparison between the cross-terms and the vertical component show significant differences, particularly from 0.25-0.29 Hz. In addition, we could probably pick the dispersion curve from 0.29-0.5 Hz, for G_c, but not for G_{zz}. From 0.5-1 Hz we do not observe signal in any dispersion curve, which is consistent with what is known about the frequency content of ocean microseisms.

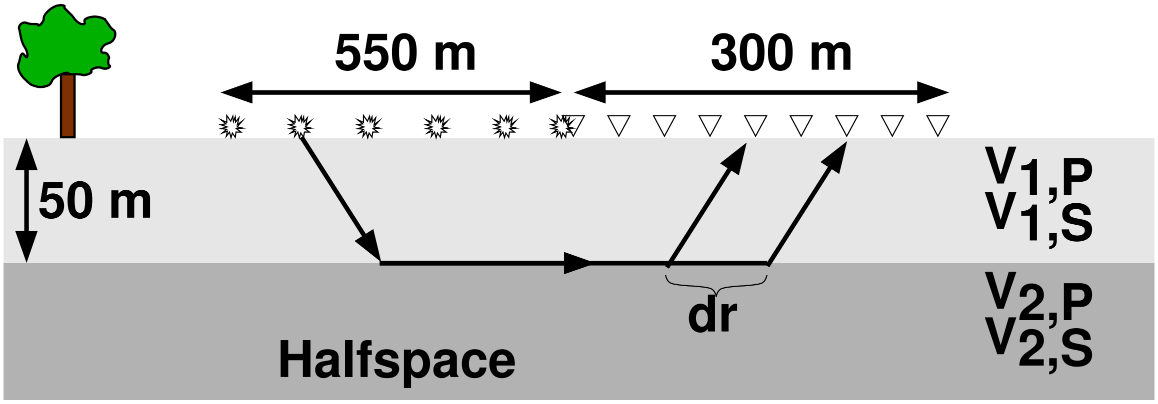

Figure 6.10: Elastic numerical model used in multi-component seismic interferometry. The velocities are $V_{1,P}$=1250 m/s, $V_{1,S}$=400 m/s, $V_{2,P}$=1750 m/s, $V_{2,S}$=900 m/s.

6.4 A Numerical Body Wave Experiment

We applied cross-term correlation to a numerical data set based on the same two-layer geometry shown in Chapter 2. However, this model is elastic with sources and receivers located at the surface (see Figure 6.10). The shear-wave velocities are 400 m/s and 900 m/s for the slow and fast layers, respectively, which gives a critical angle $\theta_{c,s} \sim 26^o$ for S waves. The P-wave velocity for the slow and fast layers remains the same, 1250 m/s and 1750 m/s, respectively. The vertical component shot record is shown in Figure 6.11(a). We see a strong Rayleigh wave as well as P and S refractions and reflections. Panels (b) and (c) show the vertical and radial components, respectively, with random Gaussian noise added (noise mean = 20% max amplitude in (a)). The source is a vertical point force with a 40 Hz Ricker wavelet.

As in the previous section, we cross-correlate the wavefields from each source using the four combinations – ZZ, RZ, ZR, RR. We taper the edges of the cross-correlation gathers and stack over sources to generate virtual shot records. Figure 6.12 shows four virtual shot records: G_{ZZ} (a), G_{RR} (b), G_{ZR+RZ} (c), and G_{ZR-RZ} (d). In (a),

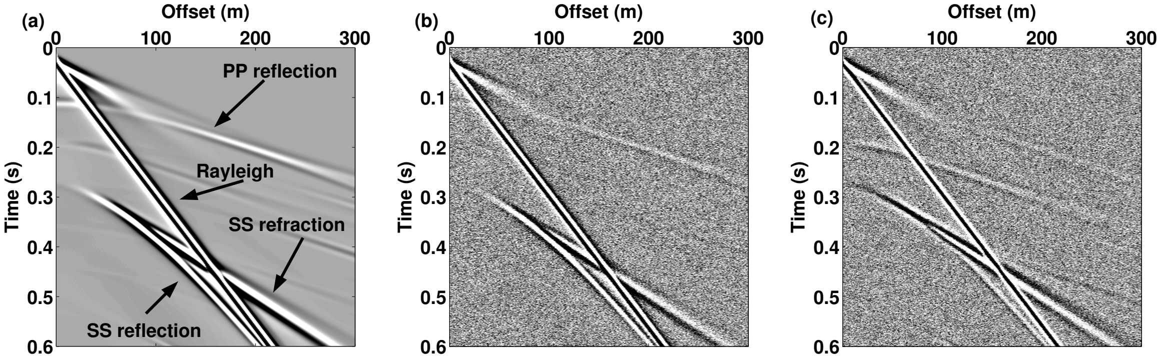

Figure 6.11: (a) Vertical component zero-offset shot record. (b) and (c) vertical and radial component shot records, respectively, with added random Gaussian noise.

(b), and (d) we see mostly Rayleigh wave and S wave energy. This makes sense if we look back to Figure 6.11, where most of the energy is Rayleigh wave and reflected and refracted S wave. In (c), there is no substantial energy, rather it looks like we cross-correlated the Rayleigh waves with arrivals at constant times causing the striped features. We see a similar pattern in the other panels as well, but the real events have much larger amplitudes.

6.5 Discussion

To investigate what happens to the virtual SS refraction amplitude and phase when we use cross-term correlations, we compare traces from the virtual shot records (Figure 6.13). We plot 3 waveforms in this figure: G_{ZZ}, G_{RR}, and G_C (i.e., G_{ZR-RZ}). These traces show a window of time at the receiver 65 m away from the virtual source. At this offset, the Rayleigh wave is outside the time window and we observe only the virtual SS refraction. As expected from the real data, the amplitude on G_{RR} is larger than G_{ZZ} for the virtual SS refraction. This is due to the velocity model and resulting incidence angle; more energy from the real SS refraction is recorded on R than Z.

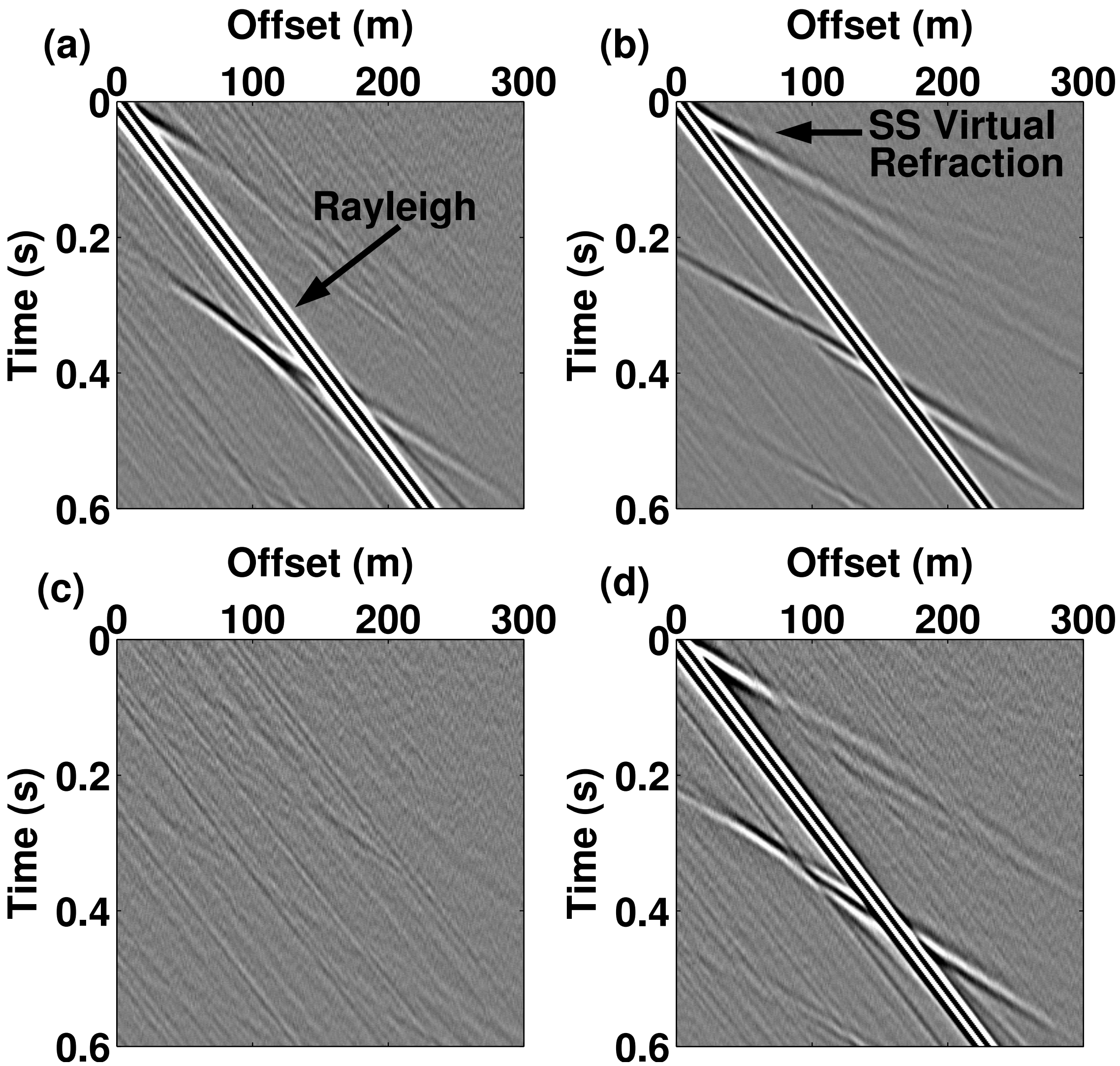

Figure 6.12: G_{ZZ} (a), G_{RR} (b), G_{ZR+RZ} (c), and G_{ZR-RZ} (d) virtual shot records. The first and last 10% of the source array is cosine tapered to zero before summing correlation gathers to generate the virtual shot record.

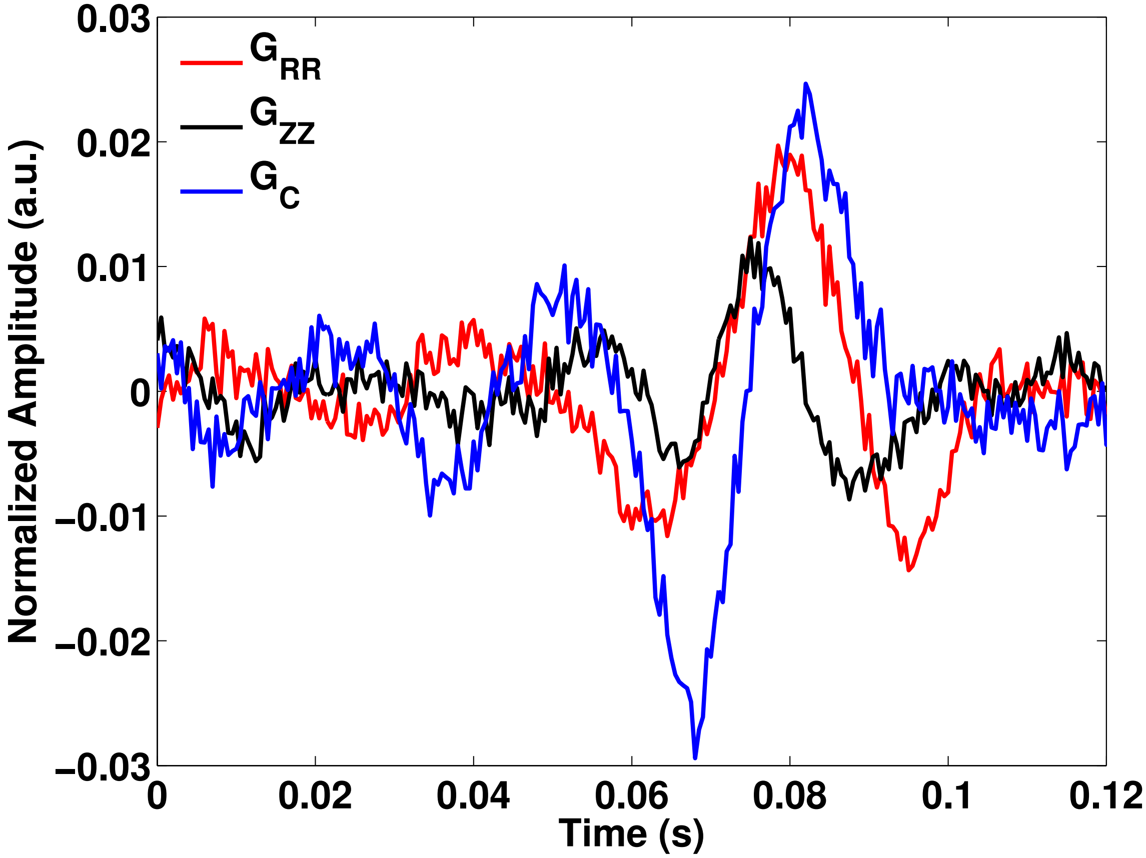

Figure 6.13: Comparison of amplitudes for different combinations of cross-correlations at 65 m offset. The arrival is the virtual S wave.

We also see that the combination of cross-terms, G_C, is higher amplitude than G_{RR}. Because some real SS refraction energy is recorded on the vertical component, cross-correlating with the radial component creates the virtual refraction on either G_{ZR} and G_{RZ}. Similar to the Rayleigh wave example, subtracting the two increases the signal-to-noise. The amount by which the amplitude increases depends on the number of sources going into the interferometric summation and the incidence angle, with the maximum G_C amplitude increase occurring when the real S wave is well represented on both components.

Finally, we see that the recovered wavelets in G_C, G_{RR}, and G_{ZZ} do no match exactly for the virtual refraction, as was the case for Rayleigh waves. This is due to differences in the wave mode polarization. Rayleigh waves commonly have elliptical particle motions, while body waves have rectilinear motion. The relationship between G_{zz} and G_C, as defined in Section 6.1, obviously does not hold true for body waves, where particle motion changes on each component (X, Y, Z) based on the incidence angle, which depends on the near-surface velocity. The amplitude and phase for body wave cross-terms are not so simple as the 1D experiment where the amplitude difference was related to the Rayleigh wave ellipticity.

Despite this, we hypothesize about instances where this kind of multi-component body-wave virtual shot record may be useful. In the case of areas with permafrost, high velocity near-surfaces violate assumptions about increasing velocity gradients and incoming body-wave reflections do not have near-vertical incidence. In these instances, common refraction statics methods, based on surface-consistency assumptions, fail. Henly (2011) shows a new technique using seismic interferometry, whereby he corrects statics problems using an incidence-angle based approach. Up to now, they have only used vertical component data. We hypothesize that using multi-component data and the Green tensor cross-terms would further improve the ability to remove statics effects, especially in noisy environments. Lastly, we demonstrate in Appendix C that the combinations of cross-terms contain unique and independent model information.

6.6 Conclusions

Ambient-noise correlations of multi-component wavefields from the Batholiths seismic experiment provide estimates of the Rayleigh-wave Green tensor. Taking advantage of the anti-symmetry of this tensor for laterally homogeneous media, the difference between the cross-terms provides a superior estimate of the Rayleigh wave compared to the estimate from the vertical components. Beam forming shows that the improvement lies in the robustness of the cross-terms in the presence of out-of-line Rayleigh-wave sources. We are also able to increase the S/N by subtracting the cross-terms. This ultimately leads us to estimate superior dispersion information. Using a numerical elastic example, we also find that subtracting the cross-term correlations improves the S/N for body waves. We demonstrate this using the virtual SS refraction. However, the relationship between the phase of the cross-terms is not as straight forward as it is for Rayleigh waves.

CHAPTER 7:

CONCLUDING REMARKS

Overview

Seismic interferometry works well for surface wave recovery because the source and receiver geometry is such that illuminating stationary-phase points is favorable. However, in practical body wave applications of seismic interferometry, spurious waves are ever present because strict requirements on the source energy distribution for the exact recovery of the Green function between receivers cannot be met in practice. Characterizing these spurious waves, or artifacts, is a necessary and logical step when interpreting interferometric data or applying standard reflection processing methods. Not doing so can lead to misinterpretations and incorrect models of the subsurface. As with any new processing method, discovering limitations is as educational as discovering possibilities.

In Chapter 2, we presented an spurious arrival we call the virtual refraction. We used a two-layered acoustic model to characterize and develop an understanding of the origin of this artifact. While the virtual refraction is not part of the true Green function, its moveout defines the wave speed V_2 in the fast layer, and because dr goes to zero as we approach the virtual shot location, the intercept time of the virtual refraction is by definition $t = 0$ s. Therefore, unlike in conventional refraction analysis, important subsurface information about the slow-layer velocity V_1 and interface depth H cannot be determined from the virtual refraction alone. However, over the duration of this dissertation multiple authors have shown that the ability to measure time lapse changes in V_2 from the virtual refraction is a useful reservoir monitoring tool and we are certain it will continue to find more use in the future. We also feel it is important to reiterate that the virtual refraction intercepts the time axis at the origin and is the direct result of stacking multiple sources. These two characteristics provide robustness in the presence of noise and make identification in the virtual shot record straightforward. In the case of multiple refractions, estimating the refractor velocity is easily achieved in the *tau-p* domain. Other researchers are currently taking advantage of the virtual refraction's robustness to noise, for example, the newly developed super-virtual refraction method directly exploits the inherent stacking in seismic interferometry (Mallinson *et al.*, 2011; Bharadwaj *et al.*, 2011).

We overcame the lack of a refraction intercept time by investigating events in the correlation gather. We identified the critical offset from the stationary-phase point in the correlation gather between two receivers. We showed in Chapter 3 that with the critical time picked on the real shot record, the real and virtual refractions provide enough information to estimate wave speeds in unsaturated and saturated sands and the depth to the water table. However, even though we determined that it is possible to pick the critical offset manually, we found it difficult in noisy environments. Therefore, in Chapter 4, we implemented a correlation domain semblance analysis. With this, we were able to estimate the velocity and depth of the slower layer in a robust and automated way, removing variability based on user interpretation. Stacking multiple semblance panels at a single virtual shot location increased the signal-to-noise ratio and gave improved estimates of these parameters. However, stacking assumes lateral homogeneity.

The virtual refraction is a practical tool for source and receiver statics. Statics are small time shifts in individual traces due to local variations in the weathering layer. These static time shifts must be estimated and removed before standard reflection processing occurs. In Chapter 5, we applied the virtual refraction analysis to synthetic 2D land seismic exploration data with statics caused by near-surface weathering layer thickness variations. Using the *delay-time method*, we estimated source and receiver statics from first-break arrival times. We went on to develop a *modified delay-time method*, wherein we used the first-break arrival times of the virtual refraction to isolate and estimate receiver statics. We showed that this approach simplifies the inverse problem by removing the source static term. In this chapter, we exploited the improved SNR of the virtual refraction due to stacking over sources and showed that using the virtual refraction increases the lateral resolution of the receiver statics estimate.

Finally, we investigated the use of multi-component data in seismic interferometry. The theoretical foundation for multi-component seismic interferometry was laid during the original theoretical developments (Wapenaar, 2004). However, the Green tensor estimate from seismic interferometry is rarely used. In Chapter 6, we developed intuitive and theoretical arguments for using the cross-terms of the Green tensor to estimate Rayleigh waves with seismic interferometry. Correlations of multi-component wavefields from the Batholith seismic experiment provided estimates of the Rayleigh-wave Green tensor. Taking advantage of the anti-symmetry of this tensor for laterally homogeneous media, the difference between the cross-terms provided a superior estimate of the Rayleigh wave compared to the estimate from the vertical components. Beam forming showed that the improvement lies in the robustness of the cross-terms in the presence of out-of-line Rayleigh-wave sources. We were also able to increase the Rayleigh wave SNR by subtracting the cross-terms. This ultimately led us to estimate superior dispersion curves.

Toward investigating multi-component cross-correlation for body waves, we used an elastic numerical example and determined that subtracting the cross-term correlations improved the SNR. We demonstrated this using the virtual SS refraction. However, the relationship between the phase of the body wave cross-terms is not as straight forward as it is for Rayleigh waves and warrants further investigation. We determined that the phase relationship between the vertical-vertical and vertical-radial cross-correlations for body waves is not the same as Rayleigh waves. This is due to the difference in particle motions. Finally, the ability of the cross-term estimates to improve body wave SNR lies in the incidence angle of the body wave of interest.

Discussion

The ideas and applications developed in this dissertation have led to numerous conference presentations and abstracts. The significant new ideas have been published or are in the process of being published in peer-review journals. As an illustration of the impact this work has had on the larger community, a list of articles citing Mikesell *et al.* (2009) (i.e., Chapter 2) are given in Appendix D. The following are my own thoughts on the relevance, significance, and future of the work presented in this dissertation as pertaining to seismic interferometry and seismic imaging.

From the academic viewpoint, seismic interferometry is still in its infancy. The theoretical foundations were laid down less than 10 years ago, and since then researchers have been investigating new ways to use this technology and determining the best method to estimate accurate interferometric wavefields. Ambient noise tomography with surface waves – in essence interferometry using passive sources with a tomography applied after – has forever changed the field of passive seismology. The increased quantity and quality of data used to image the top tens of kilometers will continue to provide new images, with greater accuracy and resolution. As previously mentioned, surface waves are the easy part of the Green function to recover. As a community, we are well aware of the requirements placed on the source energy distribution in seismic interferometry. For surface waves, all sources lie on the surface, and the energy distribution required to estimate an accurate Green function is readily available. For reflected body waves, this is not the case, especially when sources and receivers are limited to the Earth surface.

Accurate body wave recovery is where I still see the largest challenges facing our community. Many groups have shown that in environments where reflection multiples proliferate (e.g., marine acquisition) or when sensors are placed downhole with surface sources, we can successfully recover body waves. However, when this is not the case, we find ourselves struggling to find a benefit in the interferometric wavefield. For this reason, I think that new perspectives on imaging are required. We have shown in this dissertation, as well as others working in this field, that the interferometric wavefield contains useful information about the subsurface–even the artifacts. Historically, imaging practitioners have opted to suppress artifacts. I think this is a point where we should take a step back and rethink what we define as *noise*. I think the next big breakthroughs will come not from accurately estimating reflected body waves, but modifying imaging techniques that utilize *all* of the information contained the interferometric wavefield–physical and non-physical energy. The results in Chapter 5 demonstrate this point. We are now able to isolate certain parts of the wavefield (e.g., the receiver statics) because the interferometric processing removes the other part.

Finally, I think there is a bright future for the method of *source-receiver interferometry* that has began to show up in the literature. This technique applies interferometry twice, once using a boundary of receivers, and then using a boundary of sources. The order in which to two are applied depends on the target Green function, but clever reformulations such as this are going to lead to more accurate estimates of body waves. The new *super virtual refraction method* utilizes this concept and makes good use of the virtual refraction presented in this dissertation. This technique demonstrates one instance where researchers were aware of the limitations in seismic interferometry and developed a method that incorporates spurious energy to accurately estimate the true Green function.

REFERENCES

Aki, K., and Richards, P. G. 2002. *Quantitative seismology: theory and practice.* second edn. Unversity Science Books.

Aster, Richard C., Borchers, Brian, and Thurber, Clifford H. 2005. *Parameter estimation and inverse problems.* International Geophysics Series, vol. 90. Elsevier.

Bakulin, A., and Calvert, R. 2004. Virtual source: new method for imaging and 4D below complex overburden. *SEG Technical Program Expanded Abstracts*, **23**(1), 2477–2480.

Bakulin, A., and Calvert, R. 2006. The virtual source method: Theory and case study. *Geophysics*, **71**(4), SI139–SI150.

Barrash, W., Clemo, T., and Knoll, M. D. 1999. Boise Hydrogeophysical Research Site (BHRS): Objectives, design, initial geostatisical results. *Proceedings of SAGEEP99, the Symposium on the Application of Geophysics to Engineering and Environmental Problems*, 389–398.

Barrash, Warren, and Clemo, Tom. 2002. Hierarchical geostatistics and multifacies systems: Boise Hydrogeophysical Research Site, Boise, Idaho. *Water Resources Research*, **38**(Oct.), 14–1.

Barrash, Warren, and Reboulet, Edward C. 2004. Significance of porosity for stratigraphy and textural composition in subsurface, coarse fluvial deposits: Boise Hydrogeophysical Research Site. *Geological Society of America Bulletin*, **116**(9-10), 1059–1073.

Bharadwaj, Pawan, Schuster, Gerard, Mallinson, Ian, and Dai, Wei. 2011. Theory of supervirtual refraction interferometry. *Geophysical Journal International*.

Blum, Thomas E., van Wijk, Kasper, Pouet, Bruno, and Wartelle, Alexis. 2010. Multicomponent wavefield characterization with a novel scanning laser interferometer. *Rev. Sci. Instrum.*, **81**, 073101.

Burger, H. Robert, Sheehan, Anne F., and Jones, Craig H. 2006. *Introduction to Applied Geophysics: Exploring the Shallow Subsurface*. W. W. Norton & Company.

Calkins, Josh A., Zandt, George, Girardi, James, Dueker, Ken, Gehrels, George E., and Ducea, Mihai N. 2010. Characterization of the crust of the Coast Mountains Batholith, British Columbia, from P to S converted seismic waves and petrologic modeling. *Earth and Planetary Science Letters*, **289**(1-2), 145 – 155.

Claerbout, J. F. 1985. *Fundamentals of Geophysical Data Processing*. Palo Alto, CA: Blackwell Scientific.

Clement, W.P., Knoll, M.D., Liberty, L.M., Donaldson, P.R., Michaels, P., Barrash, W., and Pelton, J.R. 1999. Geophysical surveys across the Boise Hydrogeophysical Research Site to determine geophysical parameters of a shallow, alluvial aquifer. *Proceedings of SAGEEP99, The Symposium on the Application of Geophysics to Engineering and Environmental Problems*, March, 399–408.

Curtis, Andrew, Gerstoft, Peter, Sato, Haruo, Snieder, Roel, and Wapenaar, Kees. 2006. Seismic interferometry—turning noise into signal. *The Leading Edge*, **25**(9), 1082–1092.

Curtis, Andrew, Nicolson, Heather, Halliday, David, Trampert, Jeannot, and Baptie, Brian. 2009. Virtual seismometers in the subsurface of the Earth from seismic interferometry. *Nature Geosci*, **2**(10), 700–704.

Ekstrom, Goran, Abers, Geoffrey A., and Webb, Spahr C. 2009. Determination of surface-wave phase velocities across USArray from noise and Aki's spectral formulation. *Geophysical Reseach Letters*, **36**, L18301. doi:10.1029/2009GL039131.

Han, Lejia, Wong, Joe, Bancroft, John C., and Stewart, Robert R. 2008. *Automatic time picking and velocity determination on full waveform sonic well logs*. Tech. rept. 20. CREWES, University fo Calgary.

Han, Lejia, Wong, Joe, and Bancroft, John C. 2010. Time picking on noisy microseismograms. *GeoCanada Meeting*.

Hanafy, Sherif M., AlHagan, Ola, and Al-Tawash, Feras. 2011. Super-virtual refraction interferometry: Field data example over a colluvial wedge. *SEG Technical Program Expanded Abstracts*, 3814–3818.

Harmon, Nicholas, Rychert, Catherine, and Gerstoft, Peter. 2010. Distribution of noise sources for seismic interferometry. *Geoph. J. Int.*, **183**, 1470–1484.

Henly, David. 2011. Interferometric application of static corrections. *Geophysics*, **accepted**.

Johnson, Brady. 2011. *Characterization of evapotranspiration in the riparian zone of the Lower Boise River, with implications for groundwater flow.* M.Phil. thesis, Boise State University.

King, Simon, and Curtis, Andrew. 2011. Velocity analysis using reflections and refractions in seismic interferometry. *Geophysics, accepted.*

King, Simon, Curtis, Andrew, and Poole, Travis L. 2011. Interferometric velocity analysis using physical and nonphysical energy. *Geophysics*, **76**(1), SA35–SA49.

Komatitsch, D., and Tromp, J. 2002. Spectral-element simulations of global seismic wave propagation - I. Validation. *Geophysical Journal International*, **149**, 390–412.

Komatitsch, D., and Vilotte, J.-P. 1998. The spectral element method: An efficient tool to simulate the seismic response of 2D and 3D geological structures. *Bulletin of the Seismological Society of America*, **88**(2), 368–392.

Lin, F., Moschetti, M. P., and Ritzwoller, M. H. 2008. Surface wave tomography of the western United States from ambient seismic noise: Rayleigh and Love wave phase velocity maps. *Geophys. J. Int.*, **173**, 281 298. doi:10.1111/j1365-1246X.2008.3720.x.

Lowrie, W. 2007. *Fundamentals of Geophysics.* second edn. Cambridge University Press.

Mallinson, Ian, Bharadwaj, Pawan, Schuster, Gerard, and Jakubowicz, Helmut. 2011. Enhanced refractor imaging by super-virtual interferometry. *The Leading Edge*, **30**, 546.

Mehta, K., Snieder, R., Calvert, R., and Sheiman, J. 2008. Acquisition geometry requirements for generating virtual-source data. *The Leading Edge*, **27**(5), 620–629.

Mehta, Kurang, Bakulin, Andrey, Sheiman, Jonathan, Calvert, Rodney, and Snieder, Roel. 2007. Improving the virtual source method by wavefield separation. *Geophysics*, **72**(4), V79–86.

Mikesell, Dylan, van Wijk, Kasper, Calvert, Alexander, and Haney, Matt. 2009. The virtual refraction: Useful spurious energy in seismic interferometry. *Geophysics*, **74**(3), A13–A17.

Mikesell, T. D., and van Wijk, K. 2011. Seismic refraction interferometry with a semblance analysis on the crosscorrelation gather. *Geophysics, in press.*

Moret, Geoff J.M., Clement, William P., Knoll, Michael D., and Barrash, Warren. 2004. VSP traveltime inversion: Near-surface issues. *Geophysics*, **69**(2), 345–351.

Neidell, N. S., and Taner, M. Turhan. 1971. Semblance and other coherency measures for multichannel data. *Geophysics*, **36**(3), 482–497.

Nichols, Josh, Mikesell, Thomas Dylan, and van Wijk, Kasper. 2010. Application of the virtual refraction to near-surface characterization at the Boise Hydrogeophysical Research Site. *Geophysical Prospecting*, **58**(6), 1011–1022.

Palmer, D. 1986. *Refraction seismics: The lateral resolution of structure and seismic velocity.* Vol. 13. Geophysical Press.

Park, Choon B. 2011. Imaging Dispersion of MASW Data—Full vs. Selective Offset Scheme. *Journal of Environmental and Engineering Geophysics*, **16**(1), 13–23.

Poliannikov, Oleg V., and Willis, Mark E. 2011. Interferometric correlogram-space analysis. *Geophysics*, **76**(1), SA9–SA17.

Rost, S, and Thomas, C. 2002. Array seismology: Methods and applications. *Reviews of Geophysics*, **40**(3).

Sabra, Karim G., Gerstoft, Peter, Roux, Philippe, Kuperman, W. A., and Fehler, Michael C. 2005. Surface wave tomography from microseisms in Southern California. *Geophysical Research Letters*, **32**(14), L14311–L14311.

Scruby, C. B., and Drain, L. E. 1990. *Laser ultrasonics.* Adam Hilger.

Shapiro, N. M., Campillo, M., Stehly, L., and Ritzwoller, M. H. 2005. High-resolution surface-wave tomography from ambient seismic noise. *Science*, **307**, 1615–1618.

Snieder, R. 2004. Extracting the Green's function from the correlation of coda waves: A derivation based on stationary phase. *Physical Review E*, **69**(4), 046610.

Snieder, R., Wapenaar, K., and Larner, K. 2006. Spurious multiples in seismic interferometry of primaries. *Geophysics*, **71**(4), SI111–SI124.

Snieder, R., van Wijk, K., Haney, M., and Calvert, R. 2008. Cancellation of spurious arrivals in Green's function extraction and the generalized optical theorem. *Phys. Rev. E*, **78**, 036606.

Stein, Seth, and Wysession, Michael. 2003. *An Introduction to Seismology, Earthquakes and Earth Structure.* Wiley-Blackwell.

Tatanova, Maria, Mehta, Kurang, and Kashtan, Boris. 2009. Applications of virtual refraction in time-lapse monitoring. *SEG Technical Program Expanded Abstracts*, 2617–2621.

Tatanova, Maria, Mehta, Kurang, and Kashtan, Boris. 2011. Virtual refraction tomography: Application to realistic 3D model. *SEG Technical Program Expanded Abstracts*, 4239–4243.

van Wijk, K., Mikesell, T. D., Schulte-Pelkum, V., and Stachnik, J. 2011. Estimating the Rayleigh-wave impulse response between seismic stations with the cross terms of the Green tensor. *Geophys. Res. Lett.*, **38**, L16301.

van Wijk, Kasper, Mikesell, Dylan, Blum, Thomas, Haney, Matt, and Calvert, Alex. 2010. Surface wave isolation with the interferometric Green tensor. *SEG Technical Program Expanded Abstracts*, **29**(1), 3996–4000.

Wapenaar, K., and Fokkema, J. 2006. Green's function representations for seismic interferometry. *Geophysics*, **71**(4), SI33–SI46.

Wapenaar, K., Ruigrok, E., van der Neut, J., and Draganov, D. 2011. Improved surface-wave retrieval from ambient seismic noise by multi-dimensional deconvolution. *Geophysical Research Letters*, **38**, L01313.

Wapenaar, Kees. 2004. Retrieving the Elastodynamic Green's Function of an Arbitrary Inhomogeneous Medium by Cross Correlation. *Phys. Rev. Lett.*, **93**(25), 254301.

Yilmaz, Ö. 2001. *Seismic Data Analysis.* Society of Exploration Geophysicists.

APPENDIX A:

THE REFRACTION TRAVEL TIME EQUATION

Summary

While publishing the work in Chapter 4, we found that readers did not immediately arrive at the T_{refr} equation we presented. The following derivation shows how we arrive at Equation 4.3.

A.1 The T_{refr} Derivation for a Two-Layered Model

We begin with a two-layer model. The layers are laterally homogeneous and we define the model parameters shown in Figure A.1. Snell's Law states that

$$V2 = \frac{V1}{\sin(\theta_c)}, \tag{A.1}$$

where θ_c is the critical angle. The travel-time equation for a refracted wave is

$$T_{refr}(A, B) = \frac{X1}{V1} + \frac{X2}{V2} + \frac{X3}{V1}. \tag{A.2}$$

For horizontal layers and a laterally homogeneous model, $X1 = X3$, so we can combine terms to get

$$T_{refr}(A, B) = \frac{X1 + X3}{V1} + \frac{X2}{V2} = \frac{2X1}{V1} + \frac{X2}{V2}. \tag{A.3}$$

We can represent $X1$ in terms of the model parameters $X1 = \frac{H}{\cos(\theta_c)}$. Thus,

$$T_{refr}(A, B) = \frac{2H}{V1 \cos(\theta_c)} + \frac{X2}{V2}. \tag{A.4}$$

We can also write $X2$ in terms of model parameters $X2 = |A - B| - 2H \tan(\theta_c)$. The travel-time equation is then

$$T_{refr}(A, B) = \frac{2H}{V1 \cos(\theta_c)} - \frac{2H \tan(\theta_c)}{V2} + \frac{|A - B|}{V2}. \tag{A.5}$$

Now we replace $V2$ in the middle term using Snell's Law

$$T_{refr}(A, B) = \frac{2H}{V1 \cos(\theta_c)} - \frac{2H \sin^2(\theta_c)}{V1 \cos(\theta_c)} + \frac{|A - B|}{V2}. \tag{A.6}$$

We combine terms with a common denominator so that

$$T_{refr}(A, B) = \frac{2H(1 - \sin^2(\theta_c))}{V1 \cos(\theta_c)} + \frac{|A - B|}{V2}. \tag{A.7}$$

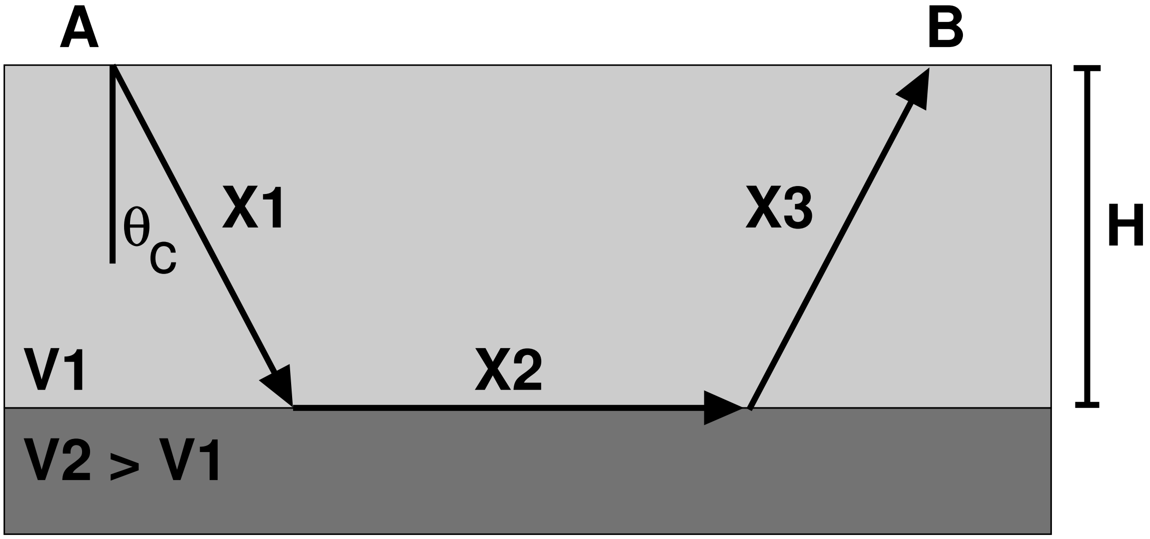

Figure A.1: Two-layer model and parameters used in derivation.

The final step uses the identity $1 - \sin^2(\theta_c) = \cos^2(\theta_c)$ to get

$$T_{refr}(A, B) = \frac{2H\cos(\theta_c)}{V1} + \frac{|A - B|}{V2}. \tag{A.8}$$

This is Equation 4.3. The only assumption we have made is that the model layers are laterally homogeneous.

APPENDIX B:

SEMBLANCE ANALYSIS AND RESOLUTION

Summary

This appendix investigates the trade-off between the two parameters we estimated using the cross-correlation gather semblance method. We look at changes in the range of thickness and slow velocity as a function of semblance amplitude and find that no matter the semblance amplitude, a constant relationship exists between the two estimates. We determine that the velocity estimate is on average five times more accurate than the thickness estimate using the semblance method.

B.1 Travel-Time Difference Equation

We return to the travel-time difference curve T_{diff} from a source at $\mathbf{s}_n$ and receivers at $\mathbf{x}_A$ and $\mathbf{x}_B$:

$$T_{diff}(\mathbf{x}_A, \mathbf{x}_B) = T_{refr}(\mathbf{x}_A, \mathbf{s}_n) - T_{refl}(\mathbf{x}_B, \mathbf{s}_n), \tag{B.1}$$

where the reflection arrival time is

$$T_{refl}(\mathbf{x}_B, \mathbf{s}_n) = \sqrt{\left(\frac{|\mathbf{x}_B - \mathbf{s}_n|}{V_1}\right)^2 + \left(\frac{2H}{V_1}\right)^2}, \tag{B.2}$$

and the refraction arrival time is

$$T_{refr}(\mathbf{x}_A, \mathbf{s}_n) = \frac{2H\cos\theta_c}{V_1} + \frac{|\mathbf{x}_A - \mathbf{s}_n|}{V_2}. \tag{B.3}$$

The parameters in Equations B.2 and B.3 are defined in Figure 4.1, and Snell's Law relates the model velocities to the critical angle, $\sin(\theta_c) = \frac{V_1}{V_2}$. With $|\mathbf{x}_A - \mathbf{s}_n| = |\mathbf{x}_B - \mathbf{s}_n| + |\mathbf{x}_A - \mathbf{x}_B|$, Equation B.1 becomes

$$T_{diff}(\mathbf{x}_A, \mathbf{x}_B) = T_{refr}(\mathbf{x}_B, \mathbf{s}_n) - T_{refl}(\mathbf{x}_B, \mathbf{s}_n) + \frac{|\mathbf{x}_A - \mathbf{x}_B|}{V_2}. \tag{B.4}$$

In Section 4.2, we defined the semblance value using Equation B.4. Next we investigate the semblance result using the same acoustic two-layer model as in Section 4.2.1.

B.2 Acoustic Numerical Example

We showed in Section 4.2.1 that with t_w=10 ms we could accurately estimate V_1 and H with V_1 being more accurate than H. We now look at how the sensitivity of H and V_1 behave at different semblance levels. To begin, we normalize the semblance plot in Figure 4.5(c). The normalized semblance panels are shown in 2D and 3D in Figure B.1(a and b), respectively. The 2D plot shows that there is correlation between the two parameters (i.e., as H decreases, V_1 increases). The 3D plot shows that even though this correlation exists, the semblance falls off steeply as we move

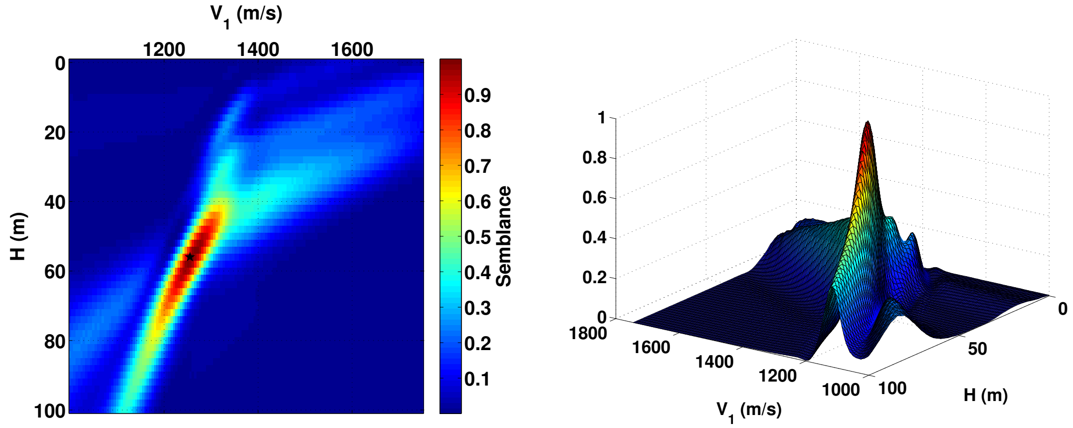

(a) (b)

Figure B.1: (a) 2D map of the semblance as a function of slow layer thickness and velocity. (b) 3D map of the semblance function. This display illustrates the steep sides around the peak.

through the H-V_1 space.

In order to investigate this correlation – or trade-off – between H and V_1, we look at the range in both parameters at different limits of the semblance. The plots in Figure B.2 show binary representations of the 2D semblance plot in Figure B.1(a). The first plot represents all values above a semblance value of 0.4 as red. We then look at the minimum and maximum H and V_1 values. For a semblance of 0.4 H has a range $32 < H < 100$ and V_1 has a range $1115 < V_1 < 1405$. Using these values, we compute the parameter deviation normalized by the maximum semblance value (H=56 m and V_1=1255 m/s). In this way, we estimate that at a semblance value of 0.4, H varies ± 60.7% and V_1 varies ± 11.6%. We show the parameter variation for each of the plots in Figure B.2 in Table B.1. In the far right column we compute the ratio of the H deviation (σ_H) over the V_1 deviation (σ_V). We can see that even though the H values increase much more than V_1 as we decrease the semblance threshold, the

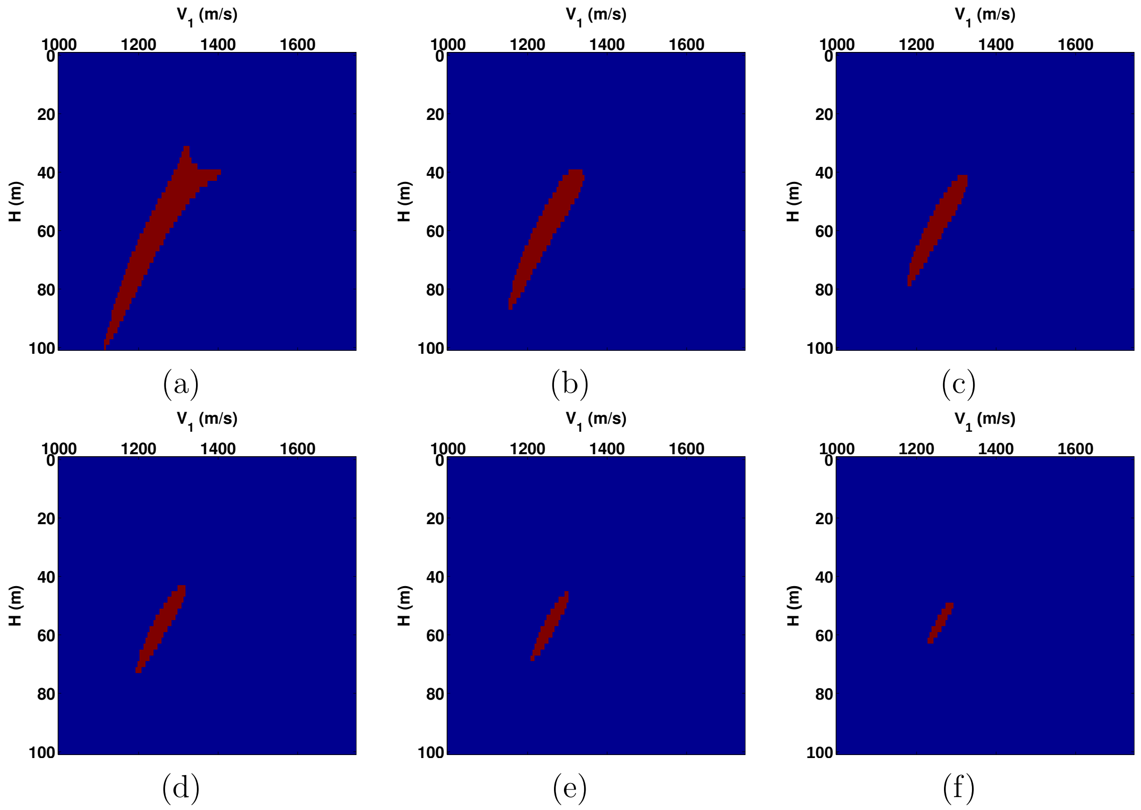

(a) (b) (c) (d) (e) (f)

Figure B.2: Clipped semblance panels for minimum semblance values of 0.4 (a), 0.5 (b), 0.6 (c), 0.7 (d), 0.8 (e), 0.9 (f). The shape remains constant from b-f.

Threshold	σ_H (%)	σ_V (%)	σ_H/σ_V
0.4	60.7	11.6	5.3
0.5	41.1	7.4	5.6
0.6	32.1	5.8	5.6
0.7	25.0	4.8	5.2
0.8	19.6	3.6	5.5
0.9	10.7	2.4	4.5

Table B.1: Table showing the deviation from the maximum semblance, normalized by the maximum semblance value.

ratio remains the same. With this in mind, we conclude that the relative accuracy of V_1 is will be 5 times better than the accuracy of H.

If we look at the complete travel-time difference equation

$$T_{diff}(\mathbf{x}_A, \mathbf{x}_B) = \frac{2H\cos\theta_c}{V_1} + \frac{|\mathbf{x}_A - \mathbf{s}_n|}{V_2} - \sqrt{\left(\frac{|\mathbf{x}_B - \mathbf{s}_n|}{V_1}\right)^2 + \left(\frac{2H}{V_1}\right)^2}, \qquad \text{(B.5)}$$

we see the term $(|\mathbf{x}_B - \mathbf{s}_n|/V_1)^2$. In this term, V_1 appears by itself. In the other terms, H and V_1 appear as a ratio $2H/V_1$. The term with V_1 by itself explains the smaller σ_v compared to σ_H at different semblance values, and the constant $2H/V_1$ ratio, to some degree, explains the constant value for σ_H/σ_V.

B.3 Discussion

It is worthwhile to briefly discuss a difference between semblance applied to raw data and semblance applied to cross-correlated data. The difference in wavelet leads to a conclusion that semblance on correlated data should be more accurate. In raw seismic data, the first-break arrival contains the key travel-time information to estimate velocity. Unfortunately, the first-break arrival has a very small amplitude compared to the rest of the wavelet. Therefore, semblance inaccurately estimates the velocity field. Contrastingly, the cross-correlated data will be zero phase, assuming the refraction and reflection wavelets are similar. This means that the maximum of the wavelet arrives at the real first-break time with high amplitude and semblance should estimate a more accurate velocity.

APPENDIX C:

MULTI-COMPONENT CORRELATION GATHERS

Summary

While working on the multi-component data it occurred to us that it may be possible to estimate the seismic properties of the Earth using multi-component correlation gathers. The following gives the background needed for such an endeavor. Up to now, we have been unsuccessful to identify stationary-phase points in the correlation gathers associated with the each of the arrivals discussed below. As you move to more complex elastic model, the cross-correlation gathers becomes increasingly difficult to unravel due to cross-correlations between the multiple wave modes present. It might also be that the modes described below do not occur or are very weak compared to the other more dominant modes such as PPP refractions.

C.1 The Critical Offset

In Chapter 2, we showed that the stationary-phase point between the reflected and refracted waves in the correlation gather gives the critical offset X_c. We now extend the idea to S- and converted wave modes. The following three equations describe the critical offsets for three possible refraction events:

$$X_{c,ppp} = \frac{2HV_{1,p}}{\sqrt{V_{2,p}^2 - V_{1,p}^2}}, \tag{C.1}$$

$$X_{c,sss} = \frac{2HV_{1,s}}{\sqrt{V_{2,s}^2 - V_{1,s}^2}}, \tag{C.2}$$

$$X_{c,sps} = \frac{2HV_{1,s}}{\sqrt{V_{2,p}^2 - V_{1,s}^2}}, \tag{C.3}$$

where $X_{c,ppp}$ represents a wave traveling down to the interface as a P-wave, refracting and traveling along the interface as a P-wave, and returning to the surface as a P-wave as shown in Figure C.1. The subscript S stands for a wave traveling along one portion of the path in an S_V mode. We showed in Chapter 2 that with the equation for $X_{c,ppp}$ and the critical time picked from real data, we can calculate H and $V_{1,p}$. With the three equations above, we can solve for the three unknown parameters without any information from real data:

$$
\begin{aligned}
H &= \frac{X_{c,sss}X_{c,sps}}{2}\sqrt{\frac{V_{2,p}^2 - V_{2,s}^2}{X_{c,sss}^2 V_{2,s}^2 - X_{c,sps}^2 V_{2,p}^2}}, && \text{(C.4)}\\
V_{1,s} &= \sqrt{\frac{X_{c,sss}^2 V_{2,s}^2 - X_{c,sps}^2 V_{2,p}^2}{X_{c,sss}^2 - X_{c,sps}^2}} && \text{(C.5)}\\
V_{1,p} &= V_{2,p}X_{c,ppp} \times \\
&\quad \sqrt{\frac{X_{c,sss}^2 V_{2,s}^2 - X_{c,sps}^2 V_{2,p}^2}{X_{c,sss}^2 X_{c,sps}^2 (V_{2,p}^2 - V_{2,s}^2) + X_{c,ppp}^2 (X_{c,sss}^2 V_{2,s}^2 - X_{c,sps}^2 V_{2,p}^2)}}. && \text{(C.6)}
\end{aligned}
$$

In this way, we determine the parameters H, $V_{1,p}$, and $V_{1,s}$ in the top layer using only the virtual refractions. The challenge is to identify the three stationary-phase points in the cross-correlation domain and estimate the lower layer velocities from the virtual refractions. We need to estimate $V_{2,s}$ from the virtual S-refraction to solve for the unknowns in the upper layer using the semblance method. It is worth noting that under certain conditions, it may be possible to determine the stationary-phase points on different combinations of multi-component data depending on the incidence of the incoming refractions. Our most recent results indicate that we need multi-component data because often not all three stationary-phase points appear in the vertical component correlation gather.

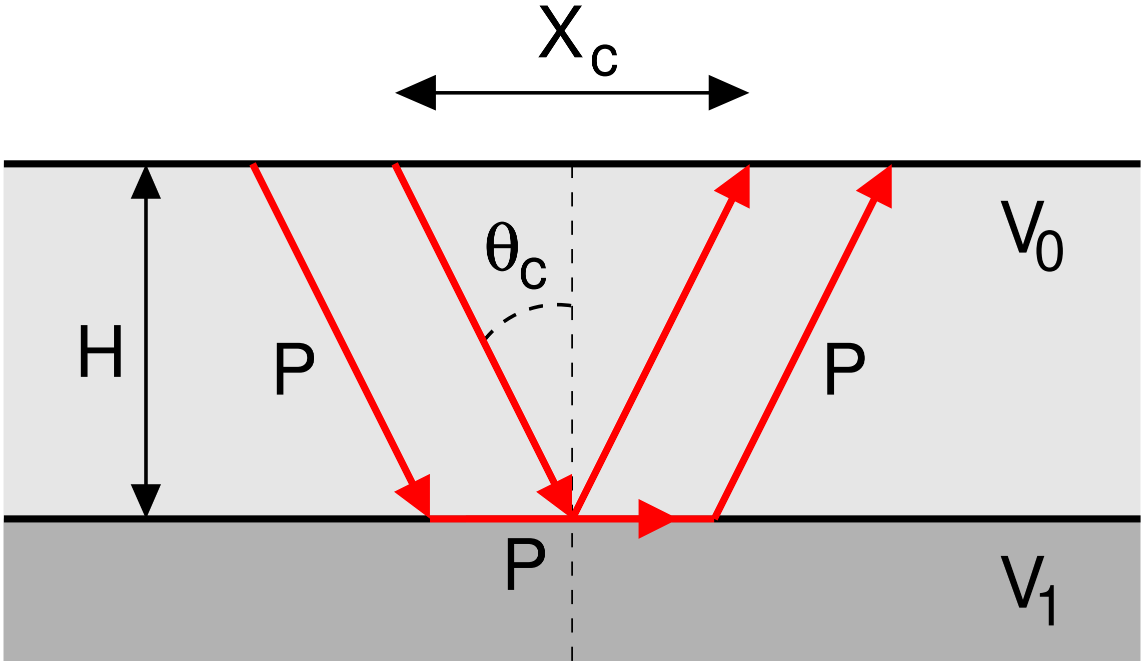

Figure C.1: Raypath for a critically reflected wave and for a refracted PPP wave.

APPENDIX D:

LIST OF CITING ARTICLES

- Al-Shuhail, Abdullatif A. 2011. Estimation of direct-arrival velocity using the linear moveout velocity analysis method with applications from eastern Saudi Arabia. *Journal of Geophysics and Engineering*, **8**(4), 524.

- Brooks, Laura A., & Gerstoft, Peter. 2009. Green's function approximation from cross-correlation of active sources in the ocean. *Journal of the Acoustical Society of America*, **126**(1), 46–55.

- King, Simon, Curtis, Andrew, & Poole, Travis L. 2011. Interferometric velocity analysis using physical and nonphysical energy. *Geophysics*, **76**(1), SA35–SA49.

- Mangriotis, Maria-Daphne, Rector, James W., III, & Herkenhoff, E. Frederick. 2011. Effects of the near-field on shallow seismic studies. *Geophysics*, **76**(1), B9–B18.

- Melo, Gabriela, Malcolm, Alison, Mikessel, Dylan, & van Wijk, Kasper. 2010. Using SVD for improved interferometric Green's function recovery. *SEG Technical Program Expanded Abstracts*, **29**(1), 3986–3990.

- Mikesell, Dylan, van Wijk, Kasper, Colvert, Alexander, & Haney, Matt. 2009. Refraction interferometry for numerical surface seismic experiments. *SEG Technical Program Expanded Abstracts*, **28**(1), 1350–1354.

- Nichols, Josh, Mikesell, Dylan, & Van Wijk, Kasper. 2010. Application of the virtual refraction to near-surface characterization at the Boise Hydrogeophysical Research Site. *Geophysical Prospecting*, **58**(6), 1011–1022.

- Ruigrok, Elmer, Mikesell, Dylan, & Van Wijk, Kasper. 2012. Scanning for velocity anomalies in the crust and mantle with diffractions from the core-mantle boundary. *Geophysical Research Letters*, in press.

- Ryberg, T. 2011. Body wave observations from cross-correlations of ambient seismic noise: A case study from the Karoo, RSA. *Geophysical Research Letters*, **38**, 5 PP.

- Snieder, Roel, Snchez-Sesma, Francisco J., & Wapenaar, Kees. 2009. Field Fluctuations, Imaging with Backscattered Waves, a Generalized Energy Theorem, and the Optical Theorem. *SIAM Journal on Imaging Sciences*, **2**(2), 763–776.

- Tatanova, Maria, Mehta, Kurang, & Kashtan, Boris. 2009. Applications of virtual refraction in time-lapse monitoring. *SEG Technical Program Expanded Abstracts*, **28**(1), 2617–2621.

- Tatanova, Maria, Mehta, Kurang, & Kashtan, Boris. 2011. Virtual refraction tomography: Application to realistic 3D model. *SEG Technical Program Expanded Abstracts*, **30**(1), 4239–4243.

- van Wijk, Kasper, Mikesell, Dylan, Blum, Thomas, Haney, Matt, & Calvert, Alex. 2010. Surface wave isolation with the interferometric Green tensor. *SEG Technical Program Expanded Abstracts*, **29**(1), 3996–4000.

- Wang, Bao-Li, Zhu, Guang-Ming, & Gao, Jing-Huai. 2010. Joint interferometric imaging of walkaway VSP data. *Applied Geophysics*, **7**, 41–48. 10.1007/s11770-010-0004-3.

- Wapenaar, Kees, Draganov, Deyan, Snieder, Roel, Campman, Xander, & Verdel, Arie. 2010. Tutorial on seismic interferometry: Part 1 — Basic principles and applications. *Geophysics*, **75**(5), 75A195–75A209.